Production and size characterization of graphene

Lucas Beetsma

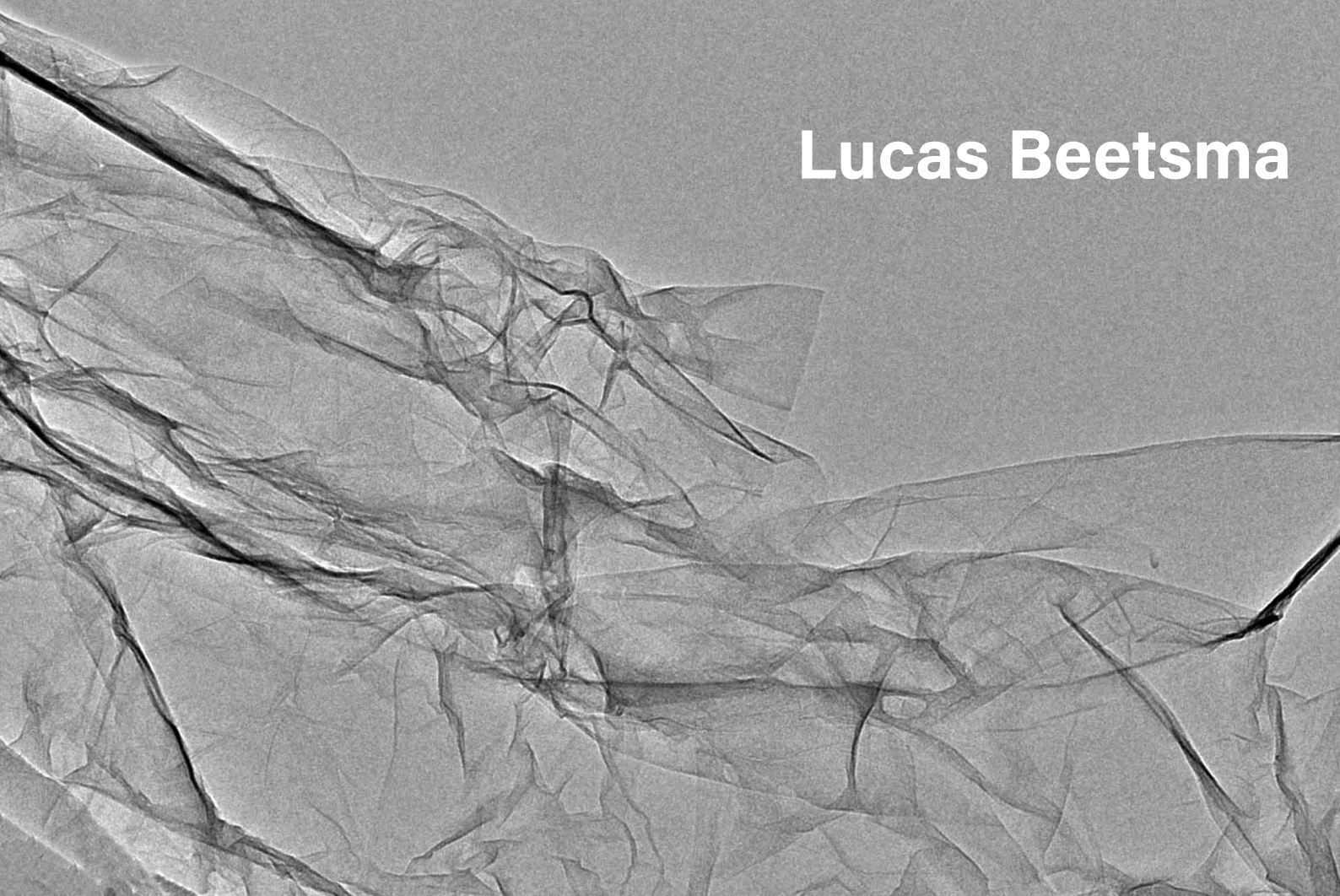

Production and size characterization of graphene

by

J. L. Beetsma

to obtain the degree of Master of Science
at the Delft University of Technology,
to be defended publicly on Monday, May 30, 2022 at 10:30 hours.

Student number:	4465202
Project duration:	Juni 1, 2021 - May 30, 2022
Thesis committee:	Lorenzo Botto, TU Delft, supervisor
	René Delfos, TU Delft
	Burak Eral, TU Delft
	Suriya Senthil Kumar, TU Delft, daily supervisor

TU Delft

Acknowledgement

For the duration of exactly one year, I dipped my toe in the world of academia and contributed to a very exciting topic. I want to thank Lorenzo Botto for giving me the freedom to be creative and to come up with something new. I felt very involved in the research group, where I enjoyed the coffee breaks that were used for brainstorming sessions. Each person in the group is working on exciting projects, on a very high level. I was impressed with the quality of the feedback everybody had for each other, even when the topics were very complicated and tough to grasp. I think Lorenzo his approach to science, which is very direct and critical, created a great environment to do research in. He was an excellent mentor and I have learnt numerous things from him. Further, I want to thank Suriya for being a great daily supervisor. We were able to have good sparring sessions and I am really impressed with his passion for fluid dynamics. Above all, he is a really nice guy and was always ready to help me. I am sure he will pursue a great career in science. I also want to thank Heng, he helped me out a lot, especially in the early stages of my research. Lastly, from Lorenzo's group, I want to thank Hugo for always being very supportive and interested in my research. I also want to thank Floor, my girlfriend, for being somewhat of a daily supervisor to me as well and helping me prepare my presentations. She has become an expert on graphene too, whether she wanted to or not. Also, she designed the front page, so credits to Floor. I want to thank my roommates for being good friends and helping me feel at home in Rotterdam. The many discussions on the roof terrace were very motivating and I believe we all do better because of each other. Last but not least, I want to thank my parents and sisters. They support me through *dik en dun*.

J. L. Beetsma

Rotterdam, May 2022

Abstract

Graphene, a 2D nanomaterial made of carbon, has gained interest in the scientific community since its discovery in 2004. Among other properties, graphene has excellent tensile strength, electrical and thermal conductivity and can be used as catalyst. Graphene has no shortage of applications, but large scale production methods are yet to be developed. LPE is a promising method, in which the layers that make up graphite are separated to produce graphene in a liquid medium. However, the flakes that are produced are polydispersed in size and thickness, which leads to the need for size selection. Current studies have achieved size selection with centrifugation. However, centrifugation has thus far been a trial-and-error procedure, without understanding the underlying physics and statistics. This research focuses on creating a rational basis by combining experiments with simulations based on fluid dynamics and statistics.

By combining results from simulations and experiments we are able to arrive at the size distributions of initial stock dispersion of graphene that was made from LPE. The simulations entail plate particle settling in a tube, where randomly generated polydisperse particles are randomly distributed in a tube. Stokes settling velocity is assumed for each particle. In parallel to this, we perform sedimentation experiments of stock dispersion at fixed relative centrifugal force (RCF) for different times. From the experiments we know the mass transfer from the supernatant to the sediment and the average thickness of the plates in the supernatant. Both these experimental results allow us to narrow the initial particle size distributions we assumed in the simulations. Thus we have developed a technique based on simple experiments and simulations that gives great insight into particle size distribution without having to perform tedious characterization such as AFM or TEM. Once the particle size distribution is known for a specific LPE protocol, it will allow the likes of both industry and academia to standardize graphene quality.

Contents

1. Introduction

1.1 Motivation

The energy transition requires environmentally friendly technologies and materials. Currently, the need for rare materials causes dependency on disputed countries and the exploitation of vulnerable countries, causing corruption and suffering of people. Researchers have been exploring alternatives, such as two dimensional (2D) materials. 2D materials are single- or few-atom thick sheets with lengths of in the order of a hundred or thousand times its thickness. Among these materials are molybdenum disulfide (MoS_2), tungsten disulfide (WS_2), borium nitride (BN) and graphene. Besides these materials exhibiting unique properties, they are environmentally friendly and could be sustainably produced, unlike rare materials. The 3D variants of these materials are well known to science, but their stability in two-dimensional form has only been discovered very recently. Graphene is the monolayer or few layer counterpart of graphite and exists of carbon atoms configured in a hexagonal, honeycomb lattice. In the famous scotch tape experiment, in 2004, graphite was micromechanically cleaved into a single stable layer of graphene [1]. The excellent properties of graphene, such as its tensile strength and electrical and thermal conductivity, were already predicted by scientists, but its stability was not known until 2004. Since then, interest has exploded [2] and the applications of 2D materials are being explored. Graphene has been shown to enhance the performance of lithium-ion batteries [3]. This property is promising for the future of energy storage, the increase of which is inevitable with the electrification of our society. Other applications are the use of graphene in composites [4], as catalysts [5] and the possibility to ink-jet print graphene to create flexible electrical circuits [6]. However, for graphene and the other 2D materials, there exists no large scale production method. One promising technique is liquid phase exfoliation (LPE) [7], but this technique yields flakes of vastly different sizes and an efficient size selection method is needed. This research aims to contribute in the size selection of polydispersed 2D materials after LPE.

1.2 Production of 2D materials

Researchers are developing a variety of methods to produce graphene and other 2D materials. Production methods can be classified into two categories: Bottom-up and top-down [8].

As the name suggests, bottom-up refers to all methods that build 2D materials atom-by-atom. The dominating bottom-up method is chemical vapor deposition [9]. In the case of graphene, a carbon source in the form of methane or ethylene flows through a controlled chamber in which carbon atoms are deposited on a substrate and hydrogen is formed as a side product. Besides the organic gas, additional hydrogen and an inert gas

are flowed into the system. The first corrodes amorphous carbon atoms [10] and the latter acts as a carrier gas. The formation of graphene is very sensitive to the ratio between hydrogen and methane and the choice of carrier gas. Other variables are the chamber material and the substrate. Metals such as copper or nickel in the form of a thin film or foam are common substrates.

The top-down refers to all methods in which 2D sheets are made from bulk material. This method has large potential to be implemented on large scale, but control of shape and size of the sheets is worse compared to bottom-up. In the case of graphene, the mother material is graphite. Graphite consists of stacked layers of a repeated hexagonal carbon structure, as seen in Figure 1. These chicken wire layers are graphene sheets. The distance between layers is 0.335 nm and the C-C distance in the plane is 0.1417 nm [11]. The crystal size and quality of graphite are of great importance for the sheet size and the rate of defects in graphene. The graphene layers are held together by van der Waals forces (vdW). The vdW forces are weaker than the forces that hold the C-C bonds in the plane and can be broken by slippage, peeling or buckling of layers.

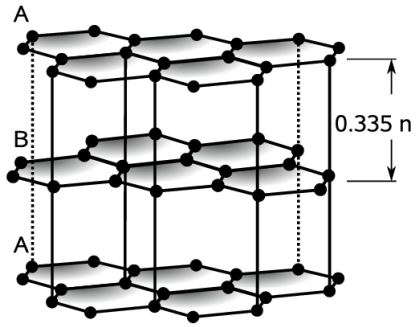

Figure 1: Crystal structure of graphite. Reproduced from Schmidt et al., 2007 [12]

Most of the top-down methods are performed in a liquid medium. For this reason, these techniques are called liquid phase exfoliation (LPE). Various LPE methods are being developed in laboratories. Some of these methods are: (1) Shear flow exfoliation, in which high shears are created in laminar or turbulent flows. These shears are chosen such that they are strong enough to break the vdW bonds between the layers, but too weak to break the C-C bonds in plane. (2) Ball milling is cheap alternative technique where inert balls are used to grind and reduce particle size. This technique is often performed in a liquid medium, but this is not necessary. (3) Sonication or ultrasonication uses a bath or horn sonicator to create high-frequency vibrations that exfoliate bulk material into 2D platelets. The resultant particles after LPE are polydispersed. The number of layers N and the lateral size L both tend to be log-normally distributed [13] [14] [15] and the shape of the flakes is irregular. The achievable number of layers and aspect ratio between lateral size and thickness are strongly dependent on the exfoliation method. Furthermore, the correlation rate between N and L also differs by method.

1.3 Issues with the size fractionation of 2D materials

As a result of the polydisperse nature, size fractionation after LPE is required. Different applications of 2D materials require specific flake sizes: Composites and ink-jet printing require relatively large graphene flakes [16] [17] and the use of MoS_2 as catalyst requires small flakes [18]. The most common method for size selection is centrifugation. Large particles sediment faster than small particles, and on this principle, separation of smaller particles from larger particles is possible. Researchers found that the average particle size in the supernatant decreases with centrifugation time: $T \propto \langle V^{-2/3} \rangle$, in which T is time and $\langle V \rangle$ is the average volume of the flakes found [19]. However, there is little understanding of the sedimentation of polydispersed particles and centrifugation has mainly been a trial-and-error procedure, lacking the connection to the fluid mechanics and statistics to the predict the content of the product. Part of the problem is the difficulty in characterizing and measuring graphene particles. Since the lateral size is typically hundreds of nanometers and the thickness is in the nanometer range, advanced microscopy and spectroscopy techniques are required to measure particles. The state of the art technology of gaining information about the distribution comes down to measuring and counting individual particles. This method is tedious and, above all, could be sensitive to getting biased data if the range of particle sizes is very large. Finally, the literature that covers centrifugation falls short in extensively describing the LPE and centrifugation protocols, making the reproduction of these experiments difficult.

1.4 Research objectives

This research aims to lay a basis for the rational purification of 2D materials by centrifugation, with the focus on graphene nanoparticles. Reaching this goal requires an estimation of the initial particle size distribution. On the basis of physics and statistics, we aim to create a method to estimate the distribution of the dispersion before and after centrifugation. This technique will use a combination of experiments and simulations. The overarching research goal is divided into the following research tasks:

1. **Liquid phase exfoliation of graphite:** The first task is to attempt to produce graphene from graphite by ultrasonication in the lab of the Process and Energy department of the TU Delft. Essential for the centrifugation, and following characterization of graphene, is the availability of a stable dispersion with constant characteristics. Therefore, we need to develop a reproducible protocol.

2. **Centrifugation experiments:** The second task is to fractionate graphene particles by centrifugation. The stock graphene dispersion will be centrifuged by a benchtop centrifuge with a swing-out rotor for 0.5 to 14 hours. Per session, $4\times\sim 30$ mL of graphene will be centrifuged. The floating fluid on top, the supernatant, will contain smaller particles and is extracted by pipetting. Experience is needed

in handling and pippeting the graphene dispersion to minimize the error by human actions. Instructions will be recorded to ensure repeatability and pass on experience.

3. **Graphene characterization:** To characterize the extracted graphene dispersions, UV-Vis spectroscopy will be performed. In this technique, light from the ultraviolet to the visible range penetrates a liquid sample to find the extinction spectrum. For 2D materials, such as graphene, the extinction spectrum provides quick information about concentration and average thickness of particles, without the need for extensive data analysis. The samples that are obtained from LPE are too concentrated to be analyzed straight away. For this reason, dilution is needed, which requires precise bookkeeping of the ratio of mixing. Another challenge lies in cleaning the cuvettes that hold the sample, which is a process that is prone to contamination.

4. **Settling velocity models:** Besides data from experiments, the physical and statistical side of centrifugation of polydispersed particles will be explored. In order to simulate large number of graphene flakes, the third task is to create models to estimate the settling velocity of single particles. Graphene flakes are well approximated by thin disks in Stokes' flow. However, surfactant and slippage may affect the settling velocity of the graphene flakes. An elaborate study will be performed on the implementation of these phenomena in the thin-disk model, and their effects will be investigated.

5. **Simulating centrifugation experiments of polydispersed particles:** In order to gain insight in the statistics of the settling of polydispersed particles, a Matlab script will be written that simulates centrifugation experiments. The script will be based on generating large amount of polydispersed particles and applying a settling velocity model to find what particles reach the sediment and what particles remain in the supernatant. In addition, these simulations will be able to track the mass transfer of graphene particles from the supernatant to the sediment as a function of the initial size distribution of particles. The macro effect of the surfactant and the slip on the sedimentation of polydispersed particles will also be explored.

6. **Finding the initial size ditribution of particles:** This research ultimately aims to produce graphene via LPE and characterize it without the need of extensive AFM or TEM analysis. The way this size estimation is achieved is by combining experimental data and simulations. On the experimental side, we are able to find the mass transfer from the supernatant to the sediment as a function of the centrifugation time, with UV-Vis spectroscopy. And as mentioned in the previous task, finding the mass transfer is also possible with simulations. However, we do not know what the distribution of particles is of the LPE product, so we simulate many thousands of initial particle size distributions and compare the mass transfer

from the simulations with the mass transfer from the experimental data. Only the simulated distributions that are compatible with the experimental data are filtered out and will give us a range of the initial distributions. If successful, this method can make size characterization much more accessible than current microscopy techniques. Additionally, with a fair estimate of the size distribution, we can predict yield and purity after centrifugation with simulations.

2. Literature review

2.1 Liquid phase exfoliation of graphene

Some of the LPE techniques are already mentioned in the introduction. These techniques and more variants will be discussed further in this section. The feasibility and quality of the product will be compared, and from here we can decide which method should be used in this research.

1. **Shear flow exfoliation:** In the literature simply named shear exfoliation, is a method that is based on creating high shear flows in the liquid medium and graphite flake mixture that causes high shear stresses, allowing for exfoliation. LPE only occurs with local shears that exceed $\dot{\gamma} > 10^4$. These shears can be generated in a variety of different manners. Varrla et al., proved that shear exfoliation can be performed with a device as simple as a kitchen blender [20]. Other research includes high shear mixers creating Couette flow [21] or Taylor-Couette vortices [22]. Furthermore, graphene has been produced by a microfluidizer [23], a device that creates high shears by flowing liquid through 75 μm channels at 2000 bar. These shear rates are in the order of 10^6 s^{-1}, with velocities up to 400 ms^{-1}.

2. **Ball milling:** Inert balls with or without a liquid medium are used to grind and reduce particle size. It has been successful in the production of graphene [24]. The balls induce a shear force upon the graphite that destroys the vdW bonds. However, the impact of the balls bumping into walls or one another causes high normal stresses that tend to break graphene in-plane, reducing lateral size.

3. **Ultrasonication:** Graphite flakes in a liquid medium are exposed to ultrasonic produced by a tip- or bath sonicator. These waves cause high shear stresses or cavitation bubbles that break the vdW bonds and change the structure of the 3D bulk material into 2D sheets [25]. Both devices have proven to be very effective in exfoliating graphite, however, their scalability is not proven, since the exfoliation happens very locally. Nevertheless, graphene production at small scale is superior with sonication, producing very high yields.

Among other methods, these LPE techniques do not change the molecular composition of the material, as is the case with reduced graphene oxide (RGO) and functionalized graphene.

2.2 Exfoliation medium

In the process of exfoliation, the liquid medium determines stability and influences the size of the particles of the dispersion [26]. Surface tension describes the degree of aggregation

[27] and should be chosen so that interfacial tension is minimized [28]. The desired surface tension for graphene can be approximated with the Hansen parameters [29] and results in a surface tension of $\gamma \approx 40$ mJ·m^{-2}. Suitable, high boiling point solvents that are commonly used are: *N*-methyl-2-pyrrolidone (NMP), *N*,*N*-dimethylformamide (DMF) and *ortho*-dichlorobenzene (*o*-DCB) [28]. However, all three are to some extent toxic [30] [31], which means that their handling will require additional safety precautions.

Alternatively, a mixture of a low-boiling solvent and water, such as ethanol / water [32] [6] or, less commonly, isopropanol/water [32] can be used. By adjusting the ratio of the solvents, the desired γ can be obtained, which is approximately 1:4 for water:ethanol [6]. However, some drawbacks of using such mixtures are the lower concentration of graphene after exfoliation and the stability sensitivity due to temperature and evaporation [6]. Aggregation remains a problem, even with the perfect ratio of solvents and the degree of dilution has to be much higher.

Lastly, surfactant-based aqueous solutions are widely used to create stable dispersions for polydispersed graphene [33] [19]. Graphitic materials are naturally hydrophobic, but molecules with a hydrophobic and hydrophilic face like sodium cholate (SC) encapsulate the graphene flakes and minimize the free surface energy. Recent studies have shown that LPE in sodium cholate (SC) results in high aspect ratios [34] and the dispersion stability is superior to that of the previously mentioned medium [33]. However, when used for ink-jet printing it decreases the connectivity between flakes and thus its conductive properties [6]. However, water plus sodium cholate is the chosen medium since health precautions do not have to be taken, contrary to high boiling solvents such as NMP [35] and due to its performance, as Professor C. Backes told.

2.3 Graphene-surfactant interaction - Cake-model

As the surfactant covers the graphene particles, the buoyant density changes. The hydrophobic side of the cholate ions bonds to the graphene and the hydrophilic side bonds to water molecules, forming a hydration layer, which increases the effective thickness of the particles. Previous studies have investigated the effect of the surfactant on the buoyant density of nanoparticles [36] [37]. Green et al., 2019 [38] made a simple model for the density of graphene encapsulated by sodium cholate and water:

$$\rho_{\mathrm{gra,SC}}(N) = \frac{\rho_{\mathrm{gra,2D}} N + 2m_{\mathrm{SC}}\sigma + 2\rho_{\mathrm{H_2O}} t_{\mathrm{H_2O}}}{(N+1)t_{\mathrm{gra}} + 2t_{\mathrm{SC}} + 2t_{\mathrm{H_2O}}} \tag{1}$$

This expression will be referred to as the cake-model, as it consists of uniform layers of SC and water. The denominator is the sum of the mass of graphene, sodium cholate and water per unit area of graphene sheet. The numerator is the total thickness of the cake. The constants have the following values:

Constant	Symbol	Value	Unit
Graphene area density	$\rho_{\mathrm{gra,2D}}$	7.66×10^{-8}	$\mathrm{g{\cdot}cm^{-2}}$
Mass SC molecule	m_{SC}	7.15×10^{-22}	g
SC packing	σ	1.35	$\mathrm{nm^{-2}}$
Water density	$\rho_{\mathrm{H_2O}}$	1000	$\mathrm{kg{\cdot}m^{-3}}$
Water layer thickness	$t_{\mathrm{H_2O}}$	3.3	nm
Graphene interlayer distance	t_{gra}	0.335	nm
SC layer thickness	t_{SC}	0.355	nm

An SC packing of $\sigma = 1.35\ \mathrm{nm^{-1}}$ corresponds to 94% coverage. Note that the thickness of a ML graphene flake with SC- and hydration layer and is 20 times larger than just the graphene thickness. Additionally, the thickness contribution of the graphene is not the interlayer graphene distance times its number of layers, Nt_{gra}, but it is $(N+1)t_{\mathrm{gra}}$, suggesting that cholate attach a distance t_{gra} from the graphene face.

2.4 Graphene-surfactant interaction - Lin's model

From various molecular simulations [39] [40], we find surfactant molecules do not adhere evenly to the graphene surface, as is assumed by the cake-model, but tend to adhere to themselves as well via their hydrophobic and hydrophilic sides. This phenomenon causes aggregation of surfactant and leaves carbon sites exposed to water. In a mixture of water and SC, there exists a concentration at which the surfactant molecules thermodynamically prefer to form aggregates rather than remain dispersed as free monomers. These aggregates are called micelles and this threshold is the critical micelle concentration (cmc). When micelles exist in the prescence of graphene, they may hinder the sedimentation rate and form large clumps of nanoflakes and micelles, which can have a negative effect on the processing of the product. In Figure 2, micellization is shown for sodium dodecylbenzene sulfonate (SDBS) from molecular simulations by Sun et al., 2014 [41]. As can be clearly observed from this figure, multiple micelles have attached to trilayer (TL) graphene, which is of size similar to that of the nanoparticles. The size of micelles is described by the aggregation number n, which is the number of molecules that form a micelle. For SDBS this number is $n \approx 55$ [42], which explains the large surfactant assemblies as seen in Figure 2. However, for sodium cholate $n = 2-6$, as cholate its facial structure does not allow for formation of large clusters [40]. In fact, less than 1% of the cholate molecules are in larger aggregates $n > 4$ at a very high concentration of 200 mM, which is roughly 20 $\times$ cmc. At low concentrations ($C = 10$ mM), 98% of the cholate ions are freely dispersed monomers, <2% are micelles consisting of $n = 2$ and <0.04% form micelles with $n = 3$. Low micellization is of benefit for this research, as formation of graphene-SC clusters is not likely.

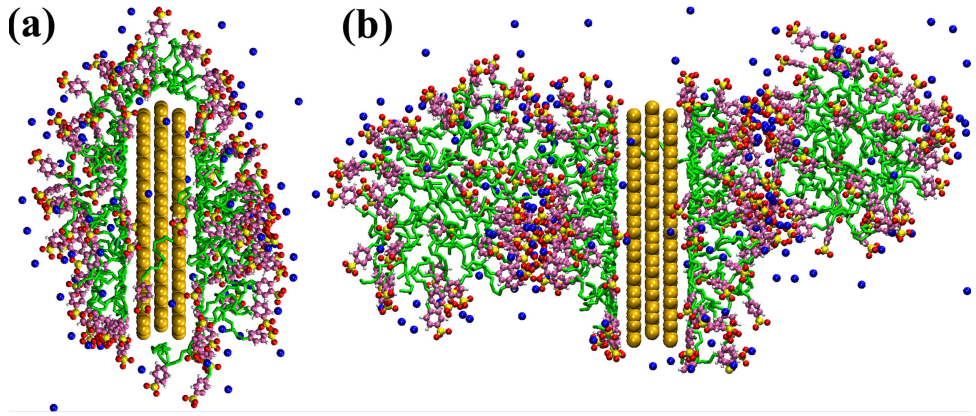

Figure 2: Side views of representative simulation snapshots for SDBS surfactants absorbed on tri-layer graphene sheets at the surface coverage density of (a) 2.8 molecules·nm^{-2} and (b) 5.7 molecules·nm^{-2}, respectively. Water molecules are not shown for clarity. Reproduced from Sun et al., 2014 [41].

Surface coverage as a function of SC concentration has also been predicted with molecular simulations [40] and can be seen in Figure 3. The coverage is shown for the number of molecules on both sides of the flake. This is roughly 1.8 molecules·nm^{-2} at maximum and thus 0.9 molecules·nm^{-2} for one side, which corresponds to a coverage of 63%, similar to the 60% coverage at 46 mM found by Lin et al., 2011 [39], both significantly less than the 94% coverage by Green et al., 2009 [38]. In addition, we assume that the coverage is independent of the layer number at higher concentrations, which has also been supported by Lin et al., 2011 [39].

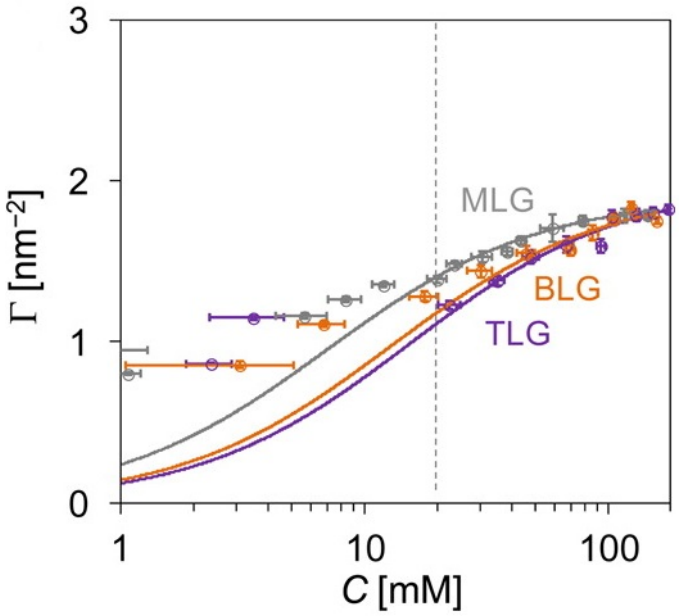

Figure 3: Molecular simulations of surface coverage σ of SC on MLG, BLG and TLG as a function of concentration C. The dotted line represents the cmc. Reproduced from Shih et al., 2015 [40].

As the coverage is roughly two thirds of the graphene area, openings between the cholate ions trap water molecules. This phenomenon is also seen in Figure 4, where the densities of the relevant molecules/ions are shown as a function of the distance from the center of ML graphene. There are two peaks in the density of water molecules, at ±0.35 nm and a weaker peak at ±1 nm. These peaks are the first and second hydration layers i.e. water molecules that are bound to the cholate ions. There is also a slight fluctuation in the water density around ±1.3 nm, suggesting that water molecules are affected by the surfactant layer up to this distance. We take the average density from $z = -1.5$ to $z = 1.5$:

$$\rho_{\text{gra-SC}} = \frac{1}{z_2 - z_1} \int_{z_1}^{z_2} (\rho_{\text{gra}} + \rho_{\text{cholate}} + \rho_{\text{sodium}} + \rho_{\text{water}}) \mathrm{d}z \tag{2}$$

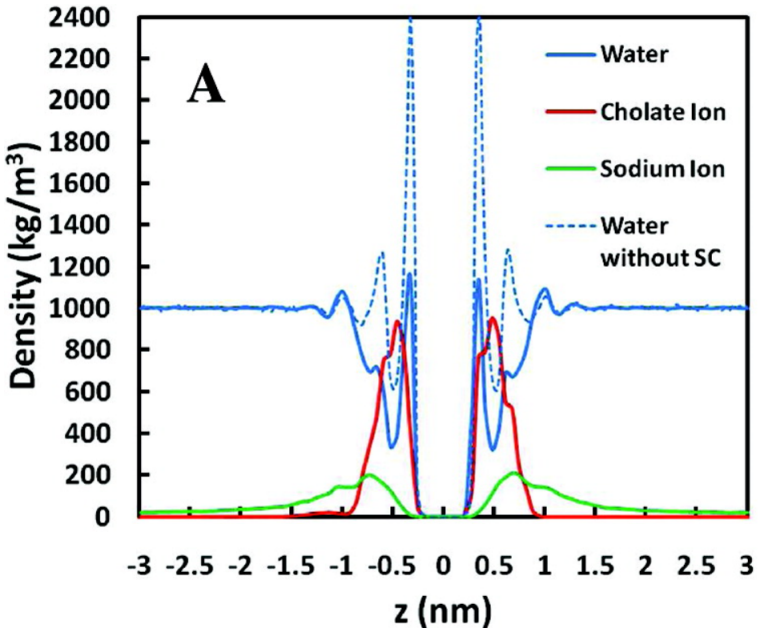

Figure 4: Cross section density profile of monolayer graphene in water and sodium cholate. Graphene flake is aligned perpendicular to the z-axis. Reproduced from Lin et al., 2011 [39].

The integral results in a total density of 1.18 kg·L^{-3}, which is in line with the cake-model from Green et al., 2009 [38], as the cake model results in 1.16 kg·L^{-3} for a monolayer flake. However, the cake-model assumes a total thickness of 7.65 nm for an ML graphene flake, which is much larger than that of the simulations by Lin et al., 2011 [39], being approximately 3 nm. Theoretically, it is possible that the force on the outer water molecules is not sufficiently strong to bind them to the surfactant when a graphene flake sediments, meaning that the thickness is smaller than 3 nm.

2.5 Centrifugation of polydispersed particles

The LPE-produced flakes tend to be polydispersed in lateral size L and thickness N [19], with both variables following log-normal distributions. The characteristic values of the lateral size and thickness of a LPE-produced ML graphene sheet are 50 nm and 0.335 nm, respectively [13], typically much smaller than sheets produced by CVD. Fractionation of 2D nanomaterials by centrifugation is very common [43].

2.5.1 Sedimentation rate based centrifugation

Sedimentation rate based centrifugation refers to size selection based on the settling velocity of particles and can be distinguished into two methods based on the preparation of the sample: Band sedimentation [15] [44], where a stock dispersion of nanosheets is layered on top of clear fluid before centrifugation, and homogeneous sedimentation [45] [13], where the nanosheets are evenly dispersed in the vial before centrifugation. Vials prepared for band and homogeneous centrifugation are illustrated in Figure 5. The band or homogeneously dispersed samples are centrifuged to find larger particles in the sediment and smaller particles in the supernatant, on average. For band sedimentation, particles are dispersed from $x = 0$ to $x = 0.1H$, H being the height of the vial. The top liquid, in which the particles are dispersed, is required to have a density lower than that of the clear fluid to create a temporarily stable dispersion. However, the liquids should be miscible, because an interface between two immiscible fluids traps the particles. A combination of water and heavy water (D_2O) can be used [15]. Band centrifugation can theoretically result in higher purity [46]: Particles with settling velocity smaller than the distance from the top layer to bottom divided by the centrifugation time are per definition unable to reach the sediment and will remain in the supernatant. A sharp cut between particles faster and slower than the settling velocity can be achieved. This sharp cut cannot be obtained with homogeneous centrifugation, as slower particles are always able to reach the sediment when they are positioned closer to the bottom of the vial. A settling velocity frequency distribution of band centrifugation is illustrated in Figure 6. Clearly, there are two discontinuities visible in the dispersion of the sediment (middle) and supernatant (right): After t seconds, particles with a settling velocity $q > \frac{H}{t} = q_{\max}$ must have reached the sediment. The second marked point $q_{\min}$ is defined by the particles that start at $x = 0.1H$ with a settling velocity of $q_{\min} = \frac{0.9H}{t}$, i.e. the particles with the lowest settling velocity able to reach the sediment. The ratio of the band height band to the height of the clear fluids dictates the steepness in the cut: The thinner the band, the steeper the cut and the higher the purity that can be reached. However, a thin band will result in a diluted SN.

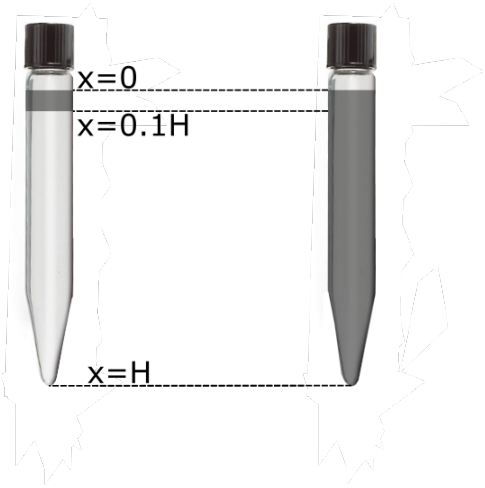

Figure 5: Band sedimentation (left), in which the graphene is dispersed from x=0 to $x = 0.1H$ and homogeneous dispersion (right) with particles dispersed from x=0 to x=H.

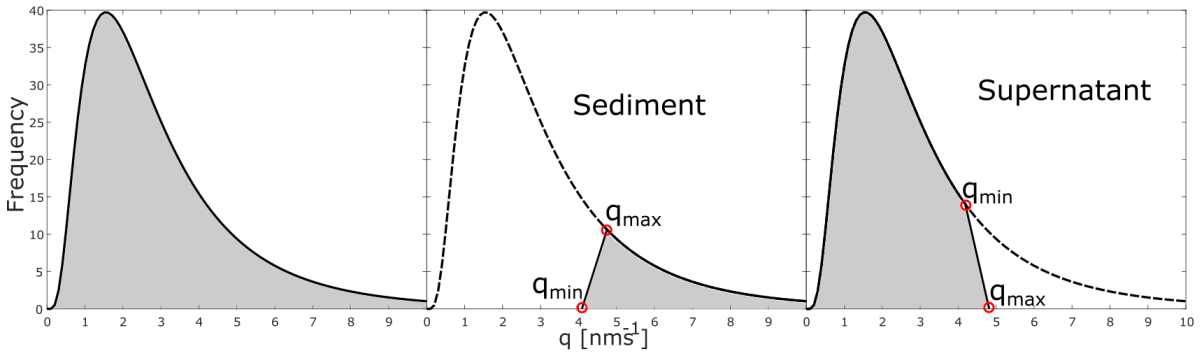

Figure 6: SVD of the initial dispersion (left), the sediment after BC (middle) and supernatant after BC (right).

2.5.2 Boycott effect

There exist two types of centrifugation rotors: The more common fixed angle rotor and the swing-out rotor. As the name suggests, the fixed angle rotor remains at a constant angle, which means that the centrifugal force is not aligned with the vial. For the swing-out rotor, the vials are free to rotate and naturally align with the centrifugal force. Fixed angle rotors are generally more robust and are commonly used for ultracentrifugation as a result of their capability to reach higher RCF. When the centrifugal force is at an angle with the vial, the Boycott effect occurs [47]: Particles that move along the wall of the vial cause vortices in the medium with speeds up to a hundred times the settling velocity [48] which increase the sedimentation rate by $O(H/b)$ [49], where H and b are the height and width of the vial. This effect could be desirable, but for band sedimentation, a swing-out rotor centrifuge is recommended to ensure one-dimensional movement.

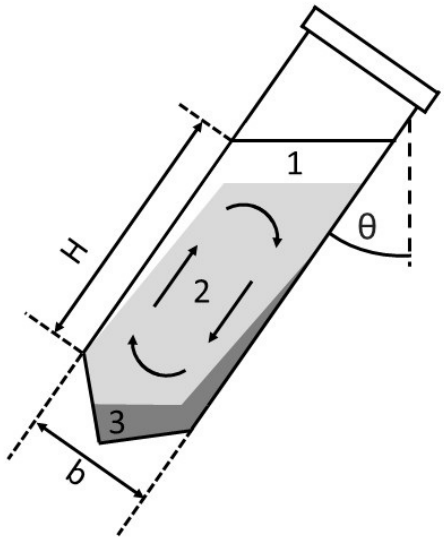

Figure 7: Schematic representation of the Boycott effect, where gravity is directed downwards. Region 1 is clear fluid. Particles are dispersed in region 2 and undergo movement due to a vortex that is illustrated with arrows. Region 3 is the sediment.

2.5.3 Liquid cascade centrifugation

One step of centrifugation will separate smaller and thinner particles in the supernatant from the larger and thicker ones in the sediment. Instead, liquid cascade centrifugation (LCC) is a technique used to fractionate particles that have a settling velocity within a certain interval [13]. Initiating with a highly heterogeneous dispersion, multiple steps are performed. The supernatant is repeatedly redispersed and centrifuged at increasing relative centrifugal force (RCF) $g_e \times$ time. With every step, the sediment is collected to find decreasing average particle size [13]. LCC has been proven to be a very effective method for size selection [50] and is illustrated in Figure 8. In practice, LCC has only been performed with multiple steps of homogeneous centrifugation. This means that with every successive step, smaller, desired particles are lost. It is theoretically possible to perform two steps of centrifugation, in which the first step is band sedimentation and the second homogeneous. In this way, much higher purity can be reached compared to two steps of homogeneous centrifugation, as in the first step the largest particles can be discarded without losing the desired particles.

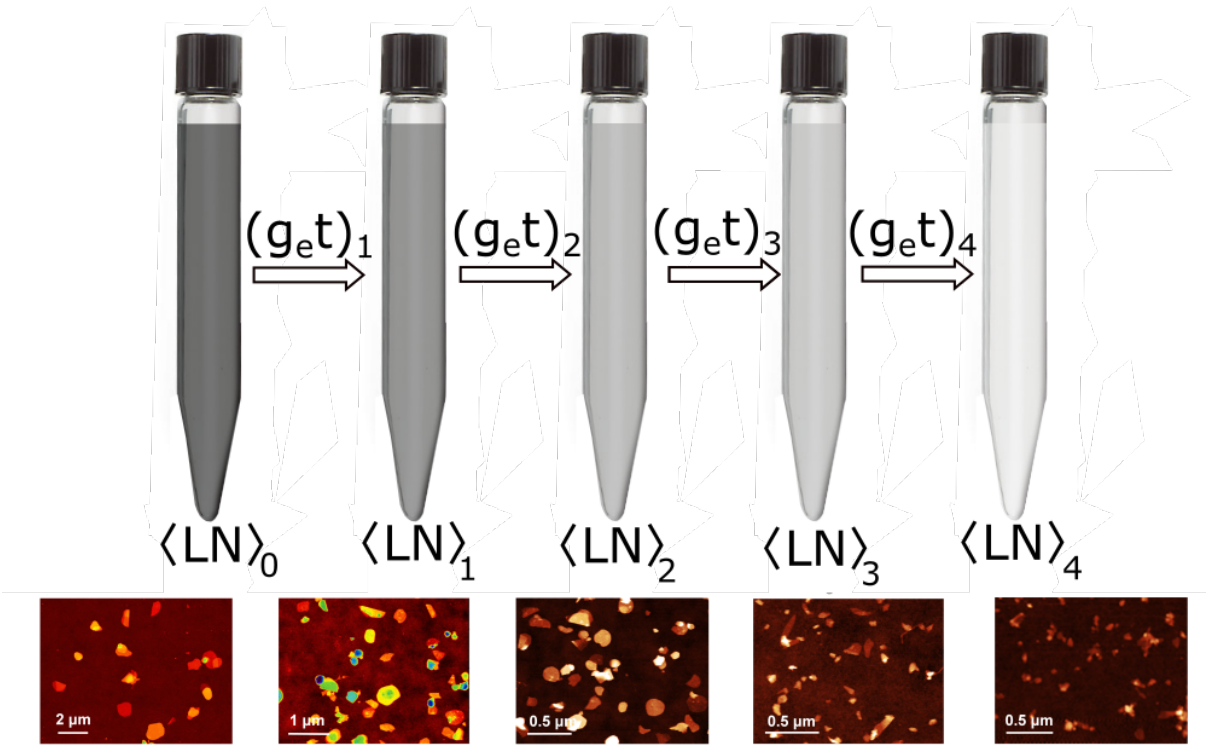

Figure 8: Illustration of LCC starting with stock dispersion with $\langle LN \rangle_0$. Every centrifugation step the RCF×time increases, $(g_e t)_{n+1} > (g_e t)_n$ and the average lateral size times layer number decreases, $\langle LN \rangle_{n+1} < \langle LN \rangle_n$. Below: Atomic force microscopy (AFM) images of decreasing particle size for illustrative purposes. Reproduced from Backes et al., 2016 [13].

2.5.4 Density gradient ultracentrifugation

With sedimentation rate based centrifugation, particles are selected based on their size. However, particles can also be separated on their density with density gradient ultracentrifugation (DGU) in which the density of the medium increases along the vial. Aqueous solutions with surfactants such as sodium cholate (SC) are commonly used to create stable dispersions for graphene [38] [33]. Surfactant wraps around the graphene flakes, this causes the density of the graphene plus surfactant to be lower than the density of pure graphene. This effect is more pronounced for thinner flakes. When equilibrium state is reached in DGU, particles are positioned along the medium where the centrifugal force is balanced by the buoyancy, thus allowing for isolation by layer number instead of weight. This technique has been shown very effective with a 80% ML yield [38].

2.6 Measurement techniques

Numerous methods have been developed to characterize graphene dispersions. As there are two dimensions of interest, the lateral size and the thickness, a dispersion can be approximately described by the averages of both dimensions and their variances. These four variables, along with the concentration, provide information about the yield and

purity of LPE and centrifugation. However, in the literature, there is a lack of reliable and quick methods to obtain this information, other than measuring large quantities of individual particles by microscopes. Efforts have been made to find average dimensions via spectroscopy techniques. These methods have the potential to provide quick information about dimensions. In this section, existing technologies for characterizing graphene are discussed.

2.6.1 Transmission electron microscopy

A common technique for measuring the lateral size of graphene particles is transmission electron microscopy (TEM) [51]. With TEM, a beam of electrons is transmitted through a sample to create an image. This is only possible with very thin samples (<100 nm), which makes graphene the perfect candidate as FL graphene is typically not thicker than tens of nanometers. With TEM, a top view of a population of graphene particles is made after which image analysis is needed. From the analysis, the lateral size and shape of the particles can be found. Around 150 counts are sufficient for a robust distribution of L [8]. Commonly found in the literature, the largest dimension of the graphene flake that is measured is the length, which will be denoted as L_m and the largest dimension perpendicular to L_m is W_m, the width, where subscript m denotes that it is gained from microscopy. To compare the flakes found from microscopy techniques to the thin disk model, we state $L{=}\sqrt{L_\mathrm{m}W_\mathrm{m}}$ to be the lateral size.

2.6.2 Atomic force microscopy

Atomic force microscopy (AFM) [52] is a type of scanning microscopy that has a resolution in the order of tenths of nanometers. The principle is the following: A spring-like cantilever with a sharp tip touches the surface of the sample. The tip is deflected up- or downwards in the z-direction as it scans the surface of the sample in the x- and y-plane. A laser is pointed at the head of the cantilever and is reflected towards a light detector. When the z-position of the tip changes, the cantilever bends and alters the angle of the laser. This is measured by the light detectors which results in a full three dimensional mapping of the sample. This makes AFM a more powerful technique than TEM, as it provides information on both N and L with a single measurement. However, taking a single image takes considerably longer with AFM. Similar to TEM, image analysis is needed. For both microscopy techniques, creating the sample is the most difficult aspect. In the case of AFM, the dispersion needs to be drop-cast onto a pre-heated Si/SiO_2 wafer of 50°C to 70°C to create bubbles that help spread the flakes more evenly [8]. It is important that the dispersion is sufficiently diluted when working with a surfactant. The surfactant should then be washed away with water and isopropanol as remainder may alter the apparent height. A more elaborate protocol can be found in [19] and [53].

2.6.3 UV-Vis spectroscopy

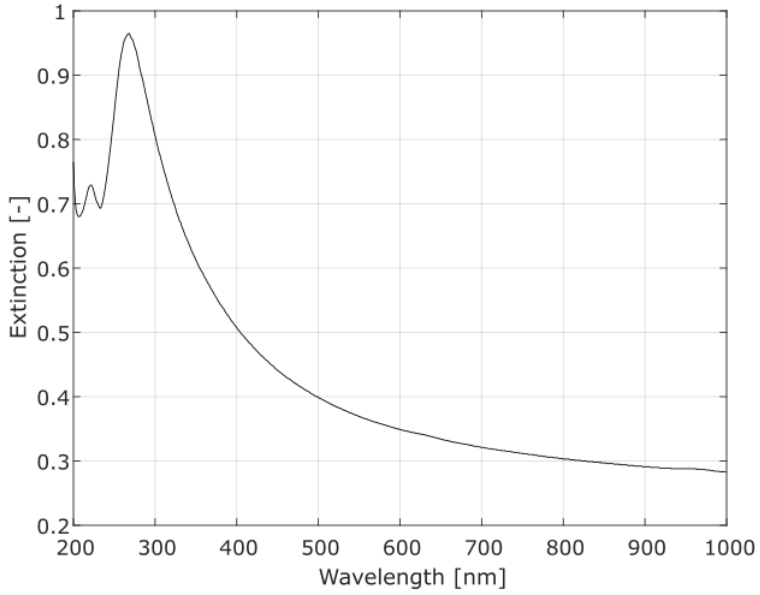

Figure 9: UV-Vis spectrum of dispersed graphene from the research group of J. Stafford et al. of the University of Birmingham. Peak at 268 nm.

Spectroscopy techniques have the potential to provide quick information about the content of the dispersion without extensive data analysis. With UV-Vis spectroscopy, light from the UV-range up to the visible range penetrates a liquid sample. The extinction of light varies over the range of the wavelength spectrum and is measured. This is due to electronic transitions, i.e. the excitation of electrons from the ground state into the excited state. This results in a "fingerprint" that is characteristic per material that is determined by the electron bonds. In Figure 9 the UV-Vis spectrum is shown for graphene dispersed in an aqueous solution with surfactant. The concentration can be determined with the Lambert-Beer relation:

$$E = \varepsilon c l \tag{3}$$

This equation relates the concentration c to the extinction E, the extinction coefficient ε and length of the sample l. The extinction is related to the transmittance as $T = 10^{-E}$ and is the sum of the absorption and the scattering: $E(\lambda) = A(\lambda) + S(\lambda)$. Similarly the extinction, absorption and scattering coefficient are related as $\varepsilon(\lambda) = \alpha(\lambda) + \sigma(\lambda)$. For graphene, ε has been found by filtration and weighing:

Research,	ε [L·g·$^{-1}$m^{-1}]	λ [nm]	**Method, medium**
Stafford et al, 2020 [53]	2322	750	Shear exfoliation, water/IPA
Hernandez et al, 2008 [7]	2460	660	Bath sonication, various solvents
Lotya et al, 2010 [33]	6600	660	Bath sonication, water/SC
Khan et al, 2010 [54]	3620	660	Bath sonication, NMP
Lotya et al, 2009 [55]	1390	660	Bath sonication, water/SDBS

2.6.4 Layer number determination from UV-Vis spectroscopy

The carbon atoms in graphite are bound to four other carbon atoms, forming single bonds or σ-bonds. In contrast, carbon atoms in graphene are bound to three other atoms, forming two single bonds and one double bond: Three σ-bonds and one π-bond. Electrons in the π-bond can be excited to the π*-state. Photons with energy in the UV-range are able to cause this excitation. In the UV-Vis spectrum, this phenomenon can be observed as there is a π-π* peak in the UV-range as seen in Figure 9. Graphitic mass is capable of absorbing longer wavelengths independently of dimensions or layer number [56]. A large amount of π-bonds relative to the total amount of graphitic mass results in a more pronounced π-π* peak, i.e. the fewer layers the average graphene particle in the dispersion, the larger the ratio of the peak to the extinction in visible light.

In practice, the graphene samples upon which the UV-Vis spectrometer is used are polydispersed and the resulting spectrum will be the result of the average of numerous particles. Backes et al. [13] established metrics for quick determination of the average layer number of the sample by comparing AFM data to UV-Vis data. Various relations were found:

$$\langle N \rangle = 0.42\lambda_{\text{peak}}\,(\text{nm}) - 108 \tag{4}$$

$$\langle N \rangle = 13.7\frac{\alpha_{550}}{\alpha_{\max}} - 1.2 \tag{5}$$

$$\langle N \rangle = 25\,\frac{\varepsilon_{550}}{\varepsilon_{\max}} - 4.2 \tag{6}$$

$$\langle N \rangle = 35.7\frac{\varepsilon_{550}}{\varepsilon_{325}} - 14.8 \tag{7}$$

However, yet-to-be published data were provided by prof. Backes, which is more robust. The replotted data with a power law fit can be seen in Figure 10. This is extremely useful data, as the way of production is is identical to that of this research.

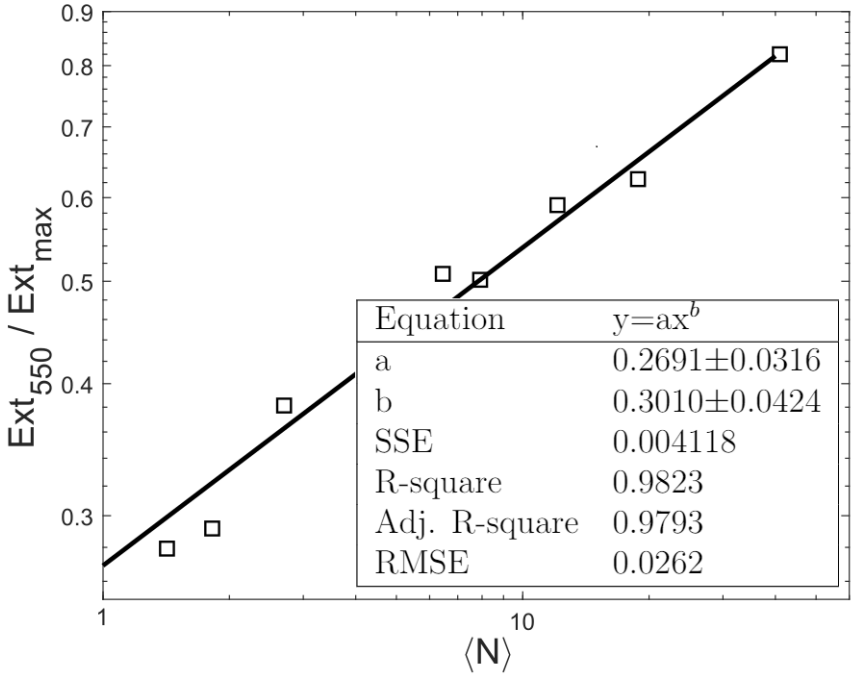

Figure 10: Average number of layers versus extinction ratio of tip sonicated graphene in water/SC. Reproduced from data provided by C. Backes.

2.6.5 Raman spectroscopy

Raman spectroscopy provides information about various properties of 2D materials, such as size and quality. The principle is as follows: Electrons from the material in question are elevated to one of their excited states by a laser with monochromatic wavelength λ_{laser}. When the excitation is elastic, the electron immediately falls back to its ground state. A photon is emitted with the same wavelength as the laser $\lambda_{\text{emitted}} = \lambda_{\text{laser}}$, which is called Rayleigh scattering. However, a very small percentage of electrons undergo inelastic excitation and the photon that is emitted has a different wavelength $\lambda_{\text{emitted}} \neq \lambda_{\text{laser}}$. This phenomenon is called Raman scattering and depends on the electron bonds in the atomic structure. The shift in the received wavelength and intensity of photons form a Raman spectrum. The shape is unique per material. The Raman spectrum of ML graphene can be seen in Figure 11. The exact origin of the peaks or so-called bands has been elaborately researched by Malard et al., 2009 [57], however, this is beyond the scope of this research, but a number of properties are associated with the shape of the spectrum. The D-band finds its origin in the rate of edge defects of the nanoflake, thus it increases with both the amount of layers and defects. Low-defect FL or ML graphene has an intensity ratio of $D/G < 0.65$ [21].

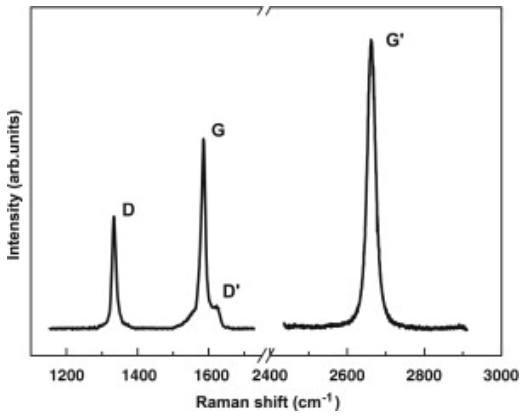

Figure 11: Raman spectrum of single layer graphene. Reproduced from Malard et al 2009 [57].

2.6.6 Lateral size determination from Raman spectroscopy

Besides UV-Vis, Backes et al., 2016 [13] made an effort to establish metrics for the average dimensions of graphene with Raman spectroscopy. One of the more robust metrics is created for $\langle L \rangle$. It is based on the following assumption: The intensity of the D-band finds its origin in the rate of edge defects and point defects. The G-band is proportional to the amount of graphitic carbon atoms. Under these assumptions the following formula was found for the average lateral size $\langle L \rangle$:

$$\langle L \rangle = \frac{k}{(I_{\mathrm{D}}/I_{\mathrm{G}})_{\mathrm{G'ene}} - (I_{\mathrm{D}}/I_{\mathrm{G}})_{\mathrm{G'\ ite}}} \tag{8}$$

From Backes et al 2016 [13], we find $k = 0.094$ and $(I_{\mathrm{D}}/I_{\mathrm{G}})_{\mathrm{G'ite}} = 0.015$. However, more recent and reliable data from Backes were provided and can be seen in Figure 12, with $k = 0.0834$ and $(I_{\mathrm{D}}/I_{\mathrm{G}})_{\mathrm{G'ite}} = 0.05015$. This metric can be used to quickly estimate the lateral size of the particles, making it a very powerful tool.

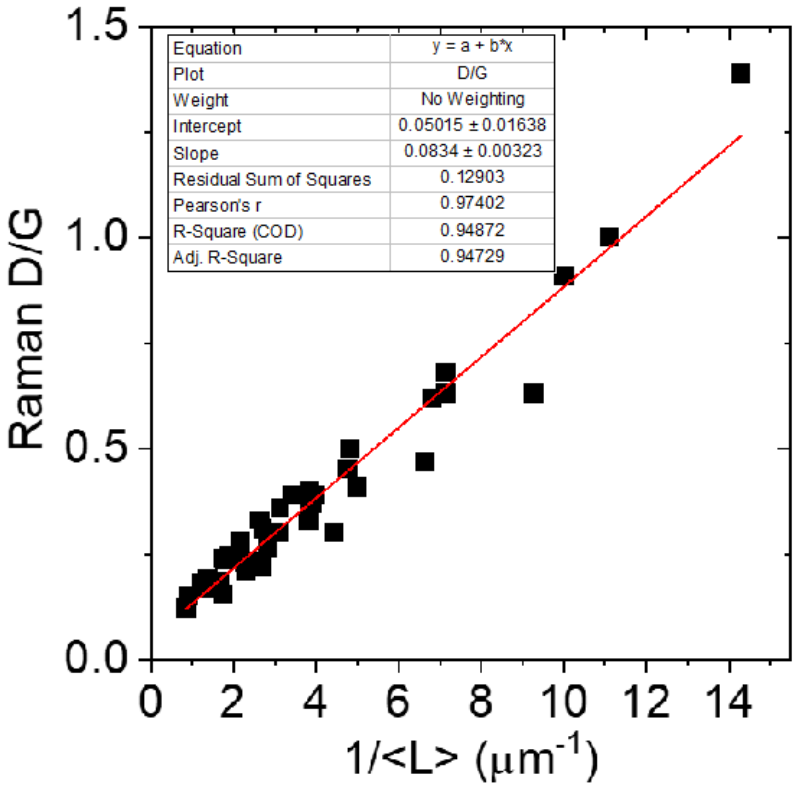

Figure 12: The relation between the D/G-band and the average lateral size of graphene flakes.

3. Theoretical background

3.1 Sedimentation of disk-like particles

During centrifugation, the particles are subjected to a centrifugal force F_C that is balanced by the drag force F_D plus the buoyant force F_B when the terminal velocity or settling velocity q is reached, as seen in Figure 13.

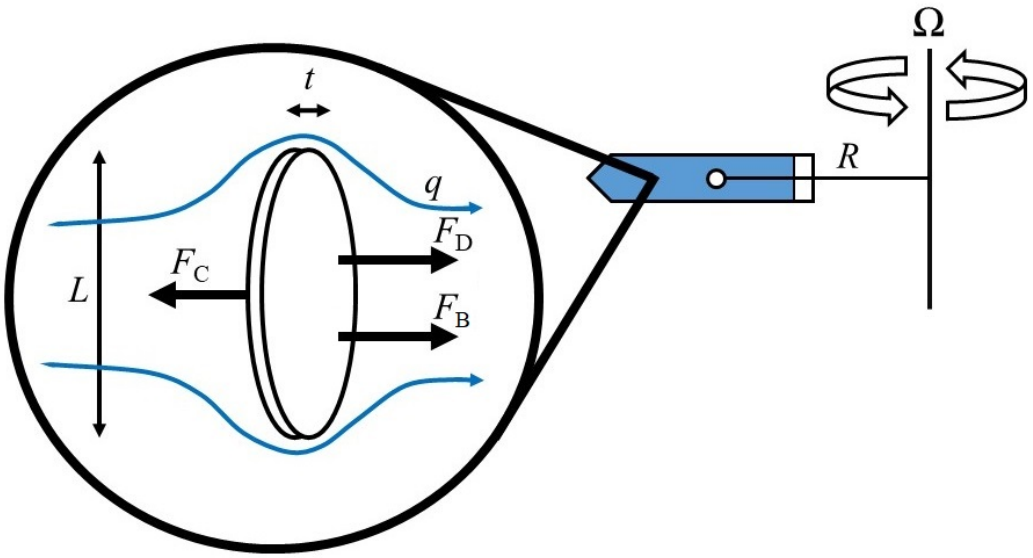

Figure 13: The force balance on a disk like particle undergoing centrifugation

The drag of spherical particles at the nanoscale can be described with Stokes flow [58]. In this regime, the inertial forces on the particle are small compared to the viscous forces (Re $\ll 1$) and assuming the no-slip boundary condition, the hydrodynamic drag force acting on a sphere is:

$$F_D = 3\pi d\mu q \tag{9}$$

In this equation F_D is the drag force, d is the diameter of the sphere, μ is the viscosity of the liquid in which the sphere is suspended and q is the velocity of the particle. The drag of nonspherical particles with a volume V is generalized to:

$$F_D = f \cdot 3\pi d_{eq}\mu q \tag{10}$$

Where f is a correction factor [59] that depends on the shape of the body and d_{eq} is the equivalent-volume diameter of the particle being equal to $(\frac{6V}{\pi})^{\frac{1}{3}}$. Graphene flakes can be modelled as thin disks with an inverted aspect ratio $E = t/L$. This is a valid approximation when $E < 0.25$. In the case of LPE graphene, the aspect ratio is ∼100 [13], which makes the assumption valid. Furthermore, we assume a no-slip boundary

condition and an attached boundary layer. Depending on its orientation, the correction factor is

$$f_{\parallel} = \frac{8}{3\pi} E^{-\frac{1}{3}} \tag{11}$$

when the direction of the disk is parallel to the axis of symmetry, and

$$f_{\perp} = \frac{16}{9\pi} E^{-\frac{1}{3}} \tag{12}$$

when the direction is perpendicular. Since the movement of nanoparticles can be described by Brownian motion, every orientation is equally possible [60] [61]. From this statement, the average drag factor $\langle f \rangle$ can be determined by adding the inverse correction factors [59]:

$$\frac{3}{\langle f \rangle} = \frac{1}{f_{\mathrm{x}}} + \frac{1}{f_{\mathrm{y}}} + \frac{1}{f_{\mathrm{z}}} \tag{13}$$

According to Loth [59], this way of addition is valid if the particle is regularly shaped about its axes. Since there are two perpendicular and one parallel orientations, the average correction factor is:

$$\frac{3}{\langle f \rangle} = \frac{2}{f_{\perp}} + \frac{1}{f_{\parallel}} \tag{14}$$

$$\langle f \rangle = \frac{2}{\pi} E^{-\frac{1}{3}}$$

(15)

Resulting in a drag force that is only dependent on L:

$$F_{\mathrm{D},\langle f \rangle} = 324^{\frac{1}{3}} \mu L q \tag{16}$$

The centrifugal force minus the buoyant force on a disk with density ρ_{disk} in a liquid with density ρ_l is given by

$$F_{\mathrm{C}} - F_{\mathrm{B}} = (\rho_{\mathrm{disk}} - \rho_l) \frac{\pi}{4} L^2 t R \Omega^2 = \Delta\rho \frac{\pi}{4} L^2 t R \Omega^2 \tag{17}$$

In which the product of the rotor radius and the angular velocity squared can be written as the equivalent gravitational acceleration $g_{\mathrm{e}}{=}R\Omega^2$. We can now find an expression for q with formulas 17 and 16:

$$q_{\langle f \rangle} = \frac{\pi \Delta\rho g_{\mathrm{e}} L t}{20736^{\frac{1}{3}} \mu} \approx \frac{\pi \Delta\rho g_{\mathrm{e}} L t}{27.48 \mu} \tag{18}$$

We notice that the settling velocity scales with Lt. This means that it is impossible

to separate thicker and shorter particles from larger and thinner particles with the same Lt by centrifugation. We take the perpendicular and the parallel orientation as an upper and lower boundary for the settling velocity, respectively:

$$q_{\perp} = \frac{\pi \Delta \rho g_{\mathrm{e}} L t}{24.42 \mu} \tag{19}$$

$$q_{\parallel} = \frac{\pi \Delta \rho g_{\mathrm{e}} L t}{36.63 \mu} \tag{20}$$

3.1.1 Dilute limit of a system of polydispersed disks

One essential assumption that is made when deriving the settling velocity in Section 3.1 is that the suspension is dilute, i.e. influence of the flow induced by particles on each other is negligible. There is no exact concentration that is defined as dilute, especially not for a polydispersed suspension of irregularly shaped particles. In the literature we find that in a monodispersity, spheres of the same size will remain largely unaffected by the presence of other spheres for a volume fraction up to roughly 1% [62]. However, for these monodispersed spheres, the Reynolds number is Re = (1) and the particle movement cannot be approximated by Stokes flow, meaning that no conclusions can be drawn for LPE-produced graphene.

More relevant to polydispersed 2D particles is the work by He et al., 2010 [61] on the hindred sedimentation of disks. In this research, experiments with monodispersed disks were performed as a function of the volume fraction ϕ. From this research, we find that there is an increased hindrance for larger aspect ratio disks, as seen in Figure 14.

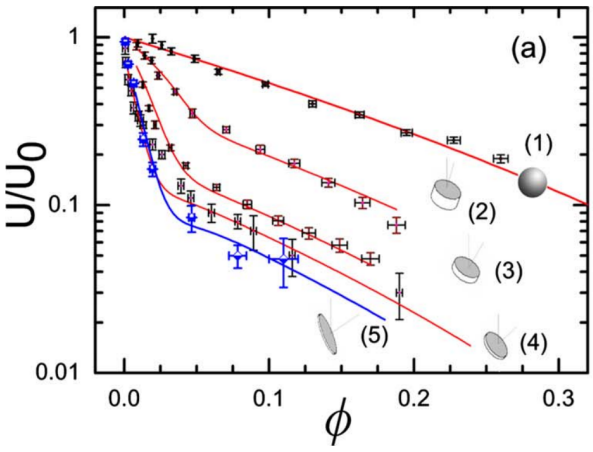

Figure 14: Experimental data of the dimensionless sedimentation as a function of particle volume fraction for suspensions of spherical wax droplets with $1/E$=1 for curve 1, ZrP platelets with $1/E$=9 for curve 4 and $1/E$=130 for curve 5, and wax disks with $1/E$=2.73 for curve 2 and $1/E$=4.76 for curve 3. Reproduced from He et al., 2010 [61].

There exists little difference in hindrance between disks with an aspect ratio of 9 (curve 4) and 130 (curve 5), especially for volume fractions of $\phi < 0.2$. This similarity

is relevant to this research, as graphene obtained from LPE typically has an aspect ratio of ∼100. Furthermore, Lotya et al., 2010 [33] produced LPE graphene in SC that had a maximum concentration of 0.3 g·L^{-1}, corresponding to a volume fraction of 0.00014, which would be very dilute when comparing to Figure 14. Still, we cannot conclude with certainty that LPE-produced graphene can be considered dilute, as the findings from He et al. concern monodispersities.

A more practical approach to this problem is to find the dependence of the viscosity on the volumetric fraction of graphene. Barwich et al., 2015 [63] researched, among other parameters, this dependency. The graphene was produced by shear exfoliation in NMP. In this research, the viscosity was found to increase beyond a critical volumetric fraction ϕ_c. This critical point indicates the concentration upon which the particles form joints and the movement of the particles is limited by other particles. The change in viscosity could serve as an indication of the free sedimentation of the graphene flakes.

3.2 Influence of slip on a spheroid and thin disk

Various molecular simulations have found that the no-slip boundary condition does not hold in graphene-water interaction [64] [65] upon which the initial settling velocity is derived. Instead, researchers have found that the velocity is nonzero at the water-graphene interface. In this case, there is a slip length b: A length that goes inside the body to the point where the velocity profile reaches zero. The slip length is visualized in Figure 15. In the limiting cases $b \to \infty$, there is perfect slip and for $b \to 0$, there is no-slip.

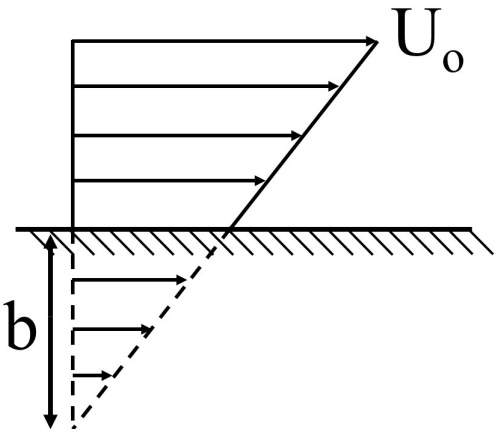

Figure 15: Visualization of the slip length b.

Slip lengths are typically in the order of nanometers, e.g. slip is negligible in most cases with a typical length scale is in the order of micrometers or larger. However, the slip length of graphene is found to be in tens on nanometers [66] [64] [65], which is in the same order as the typical size of graphene platelets. This similarity in scale means that the slip length has a significant effect on the friction of the smallest particles. In our case, we are dealing with the interaction between graphene, water and surfactant or only water-

surfactant interaction if we consider the flake well covered. Intuitively, the hydrophilcity of the surfactant covered face would attract the water molecules in such a manner that there would be no slip along the interface. Otherwise, if the hydration shell remains bound to the surfactant, there would be water molecules moving along water molecules, where a slipless assumption could be applicable. However, hydrophilicity does not predict whether there will be partial slip or no slip. Surfactants have been known to cause or increase a slip length [67]. The counter intuitive behaviour of slip is exemplified in the work undertaken by Henry et al., 2005 [68]. In this research, the boundary slippage of water plus surfactant (CTAB) and hydrophilic surfaces was experimentally investigated. The results show that the bare hydrohpilic surface produces the largest slip length and that an increase in surfactant concentration caused a decrease in slip. In addition, the slip length associated with zero or low surfactant concentration shows positive dependency on the shear rate, while the slip length remains roughly constant for high concentration. The decreased slip length cannot be explained by hydrophilicity, since the surfacant creates hydrophobic patches on the hydrophilic surface and this would intuitively increase slip. Molecular dynamics simulations by Kunert et al., 2008 [69] to hydrophobic surfaces with various concentrations of surfactant found a decrease in slip length as a function of surfactant.

Various papers have been found on the influence of slip on a discs with no slip, perfect slip and partial slip. Let us revisit Equations 10, 11 and 12 from Loth et al., 2008:

$$F_{\mathrm{D}} = f \cdot 3\pi d_{\mathrm{eq}} \mu q \tag{10}$$

$$f_{\parallel,\mathrm{Loth}} = \frac{8}{3\pi} E^{-\frac{1}{3}} \tag{11}$$

$$f_{\perp,\mathrm{Loth}} = \frac{16}{9\pi} E^{-\frac{1}{3}} \tag{12}$$

These are the equations for the friction of a disk moving parallel and perpendicular to its axis of symmetry with zero slip and hold for $E < 0.25$. Slightly different relations were found by D. Dusenbery for $E \ll 1$ and show good agreement to the equations of Loth:

$$f_{\parallel,\mathrm{D'bery}} = \frac{4E^{-\frac{1}{3}}}{3\arctan(E^{-1})} \tag{21}$$

$$f_{\perp,\mathrm{D'bery}} = \frac{8E^{-\frac{1}{3}}}{9\arctan(E^{-1})} \tag{22}$$

Continuing to the partial and free slip cases, we consider the following literature. Y. Chang and H. Keh did a combined analytical and numerical study of the Stokes flow of a rigid oblate spheroid moving parallel [70] and perpendicular [71] to its axis of symmetry for no slip, partial and free slip. The relevant numerical values are displayed below in

Tables 1 and 2.

$f_{\parallel} = F_{\mathrm{D}}/3\pi\mu Lq$				
$\boldsymbol{b/L}$	$\boldsymbol{E}$**=0.9**	$\boldsymbol{E}$**=0.5**	$\boldsymbol{E}$**=0.2**	$\boldsymbol{E}$**=0.1**
0 (NS)	0.9801	0.9053	0.8615	0.8525
0.1	0.9052	0.8448	0.8316	0.8396
1	0.7496	0.7696	0.8157	0.8355
∞ (FS)	0.6804	0.7470	0.8122	0.8347

Table 1: Friction coefficient $f_{\parallel}$ of an oblate spheroid translating parallel to its axis of symmetry as a function of the relative slip b/L. NS denotes no-slip and FS denotes free-slip. Reproduced from Y. Chang and H. Keh 2008 [70].

$f_{\perp} = F_{\mathrm{D}}/3\pi\mu Lq$				
$\boldsymbol{b/L}$	$\boldsymbol{E}$**=0.9**	$\boldsymbol{E}$**=0.5**	$\boldsymbol{E}$**=0.3**	$\boldsymbol{E}$**=0.2**
0 (NS)	0.9597	0.7927	0.7049	0.6596
0.1	0.8828	0.7156	0.6284	0.5839
1	0.7097	0.5416	0.4535	0.4084
∞ (FS)	0.6263	0.4572	0.3680	0.3223

Table 2: Friction coefficient $f_{\perp}$ of an oblate spheroid translating perpendicular to its axis of symmetry as a function of the relative slip b/L. NS denotes no-slip and FS denotes free-slip. Reproduced from Y. Chang and H. Keh 2011 [71].

Note that the friction coefficient increases with decreasing E for Loth and Dusenbery, but decreases in the case of Chang and Keh. The reason being the context of the formula, for Loth and Dusenbery, the charecteristic length is the equivalent volume diameter d_{eq} and for Chang and Keh it is simply L. When $E \to 0$ in the context of d_{eq}, the shape becomes an infinitely large disk with a finite volume. When $E \to 0$ when F_{D} is normalized by L, the disk has a finite diameter L with zero volume and zero height. When we normalize the drag from Loth and Dusenbery in a similar fashion as done for Chang and Keh, we find constant drag coeffiecients:

$$f_{\parallel} = F_{\mathrm{D}}/3\pi\mu Lq = 0.971 \tag{23}$$

$$f_{\perp} = F_{\mathrm{D}}/3\pi\mu Lq = 0.647 \tag{24}$$

The agreement for the parallel transversion is poorer than for the perpendicular movement. Interestingly, when considering the friction of the oblate spheroid moving in parallel direction, we find a very weak dependency on the slip, even in the limiting cases the drag is close to independent on the slip. J. D. Sherwood [72] found a similar result for the exact drag on a disk with zero thickness.

	b/L=0	$b/L \ll 1$	$b/L \gg 1$
$f_{\parallel}$	$8/3\pi$	$8/3\pi$	$8/3\pi$
$f_{\perp}$	$16/9\pi$	$(32/3\text{-}8.25b/L\text{+}4.58(b/L)\ln(b/L))/6\pi$	$L/3b$

Table 3: Drag coefficients of an infinitely thin disk for the limiting cases of zero slip, b/L=0, slip length much smaller than the diameter of the disk and slip length much smaller than the diameter of the disk. Reproduced from Sherwood 2012 [72].

As $8/3\pi \approx 0.8488$, the agreement for the parallel motion is nearly perfect with Chang and Keh $b/L = 0.1$. Similarly, $16/9\pi \approx 0.5659$ is in good agreement with the extrapolated value for the thin disk limit of the perpendicular motion of Chang and Keh. Lastly, filling in $b/L = 0.1$ in the formula for the small slip in perpendicular direction, results in a drag of $f_{\perp} = 0.4662$, being in agreement with the descending trend in Table 2.

3.3 Settling velocity distribution of polydispersed disks

The log-normal function is a naturally recurring distribution, often found in polydispersed particles such as crushed rocks [73] or powders [74], or as mentioned earlier, LPE-produced 2D material. The lognormal distribution is positive and skewed. If a random variable X is normally distributed with μ_{x} and σ_{x}, then taking the exponent of X will result in the lognormally distributed variable Z.

$$X = \mathcal{N}(\mu_{\mathrm{X}}, \sigma)$$

$$Z = e^{\mathcal{N}(\mu_{\mathrm{X}}, \sigma_{\mathrm{X}})} = \mathrm{lognormal}(\mu_{\mathrm{X}}, \sigma_{\mathrm{X}})$$

Z is described by μ_{X} and σ_{X}, but note that these parameters are not the mean and standard deviation of the lognormal distribution. Instead, the mean and variance of Z are:

$$E(e^{\mathcal{N}(\mu_{\mathrm{X}}, \sigma_{\mathrm{X}})}) = e^{\mu_{\mathrm{X}} + \sigma_{\mathrm{X}}^2/2} \tag{25}$$

$$\mathrm{var}(e^{\mathcal{N}(\mu_{\mathrm{X}}, \sigma_{\mathrm{X}})}) = (e^{\sigma_{\mathrm{X}}^2} - 1)e^{2\mu_{\mathrm{X}} + \sigma_{\mathrm{X}}^2} \tag{26}$$

The settling velocity of a thin disk can be estimated with Equation 18. The distributions of L and N are used to find the frequency distribution of q, the settling velocity distribution (SVD). L and N are independent and log-normally distributed:

$$ln(L) = \mathcal{N}(\mu_L, \sigma_L)$$

$$ln(N) = \mathcal{N}(\mu_N, \sigma_N)$$

The settling velocity q is proportional to the lateral size L times layer number N. For simplicity, the influence of the surfactant or slip are not taken into account:

$$q \propto LN = e^{\mathcal{N}(\mu_L,\sigma_L)+\mathcal{N}(\mu_N,N)}$$

We know that the sum of two normal distribution is a new normal distribution [75]:

$$ln(q) = \mathcal{N}(\mu_L + \mu_N + ln(C), \sqrt{\sigma_L^2 + \sigma_N^2}) \tag{27}$$

We find a new log-normal distribution for q with $\mu_q = \mu_L + \mu_N + ln(C)$ and $\sigma_q = \sqrt{\sigma_L^2 + \sigma_N^2}$, where C includes all other constants in q.

By means of example, we consider data from Backes at al., 2016 [13]. Log-normal distributions were fitted to the histograms of N and $L = \sqrt{L_\mathrm{m} W_\mathrm{m}}$ in Figure 16.

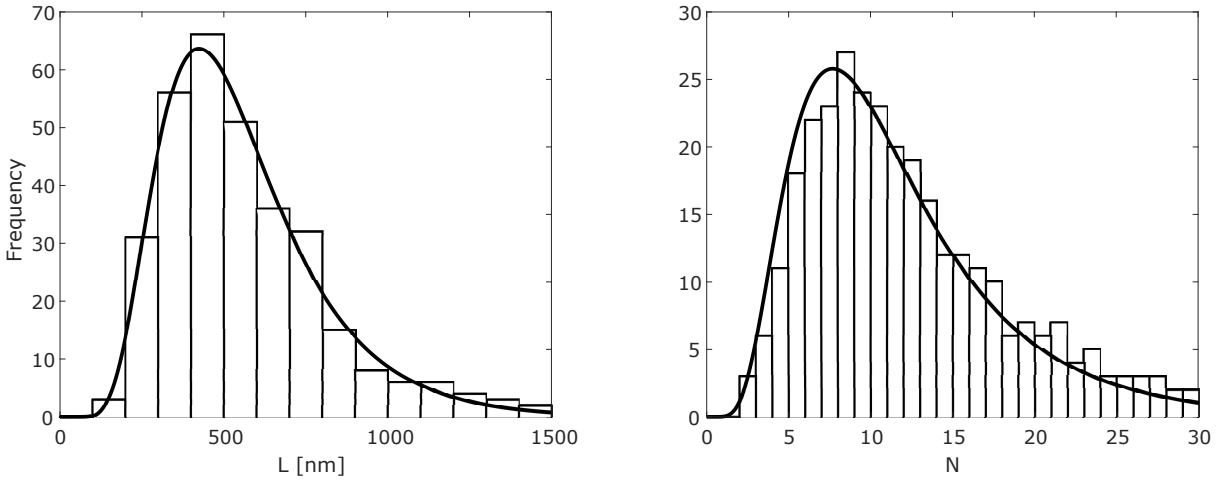

Figure 16: Distribution of LPE graphene with lognormal fit from Backes et al., 2016 [13] (left) the lateral size with $\langle L \rangle = 559.8$ nm, $\mathrm{var}(L) = 63,570$ nm^2 and (right) the number of layers with $\langle N \rangle = 11.9$ and $\mathrm{var}(N) = 47.7$.

The following parameters were found: $\mu_L = 6.235$, $\sigma_L = 0.430$, $\mu_N = 2.330$ and $\sigma_N = 0.539$. With these independent distributions and formula 18, we find a new distribution for q, with $\mu_q = -19.810$ and $\sigma_q = 0.690$ as shown in Figure 18. Particles are generated in Figure 17 with the lognormal distributions found from the data. When q is set to constants, we find contour lines in the N-L space. Particles that lie on the same contour line, are not separable by centrifugation. The frequency of the settling velocity for the generated points has been plotted in Figure 18.

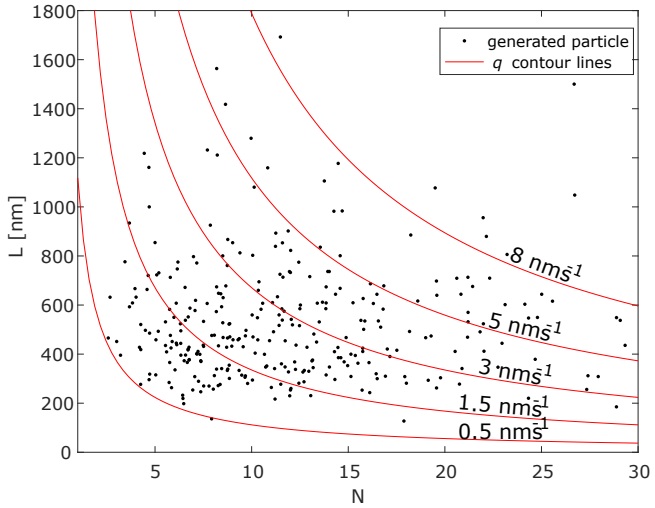

Figure 17: Generated particles with dimensions following the distributions above. Constant settling velocity lines are drawn to indicate particles with equal settling velocity

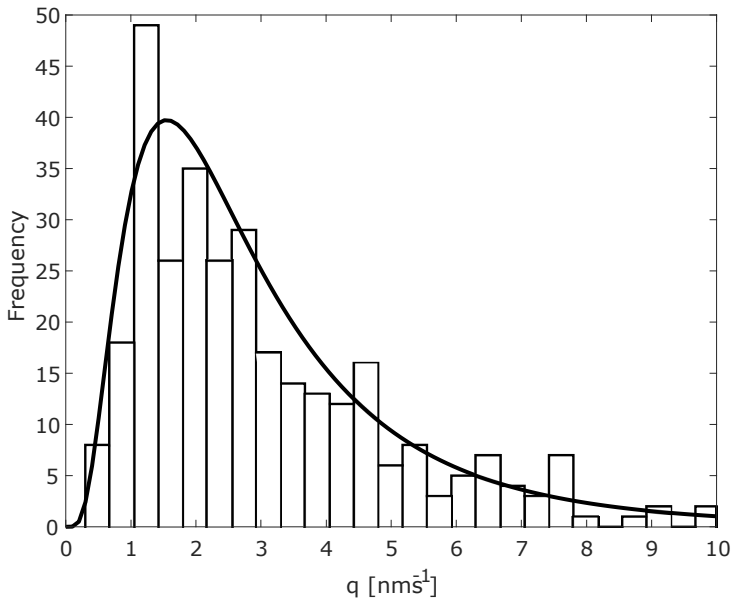

Figure 18: Frequency of settling velocities of the particles shown left that fit the distribution gained from derivation above, $\langle q \rangle = 3.16$ nm·s^{-1}, var$(q) = 6.90$ nm^2·s^{-2}.

3.3.1 Correlation and covariance

In the example in Section 3.3, N and L are uncorrelated, that is, no prediction can be made about the lateral size given information about the layer number and vice versa. However, this assumption might be invalid when we look at data from the literature in which extensive AFM measurements were performed on graphene populations [13] [20]. What was found is that thicker flakes tend to have a slightly larger lateral size as well, which means that there exists positive correlation between N and L. The formula for the correlation between the arbitrary variables X and Y is the following:

$$\rho_{\mathrm{X,Y}} = \mathrm{corr}(X, Y) = \frac{\mathrm{cov}(X, Y)}{\sigma_{\mathrm{X}}\sigma_{\mathrm{Y}}} = \frac{\mathrm{E}\left[(X - \mu_{\mathrm{X}})\,(Y - \mu_{\mathrm{Y}})\right]}{\sigma_{\mathrm{X}}\sigma_{\mathrm{Y}}} \tag{28}$$

Where $\mathrm{cov}(X, Y)$ is the covariance between X and Y. Note that μ_{X}, μ_{Y}, σ_{X} and σ_{Y} are not interchangeable with the μ_L, μ_N, σ_L and σ_N from the previous section, as the latter parameters are not the actual means and variances of L and N. If we measure a certain amount of particles, where particle i has the dimensions L_i and N_i and the average dimensions of all particles are $\langle L \rangle$ and $\langle N \rangle$, the correlation would be:

$$\rho_{\mathrm{L,N}} = \frac{\mathrm{E}\left[(L_i - \langle L \rangle)\,(N_i - \langle N \rangle)\right]}{\sqrt{\mathrm{var}(L)}\sqrt{\mathrm{var}(N)}} \tag{29}$$

4. Experimental methods

4.1 Liquid phase exfoliation of graphite

The exfoliation of graphite was performed with a Cole-Parmer 500 W ultrasonic processor at 60% amplitude for 6 hours without pulsation. Graphite and sodium cholate, both purchased from Sigma-Aldrich, were added to 200 ml of deionized water with a concentration of 20 g·L^{-1} and 6 g·L^{-1}, respectively. The beaker was submerged to about halfway its height in an ice bath of 5 L. The ice was replenished every 2 hours. Parafilm was placed over the beaker to prevent the water from evaporating and to ensure there is no contamination. In addition, the parafilm serves as an indicator of temperature control. When no condensation is observed against the film, the temperature remains low. The parafilm is tightened with scotch tape and a small puncture is created with a knife. All instruments used, e.g. spoons and beakers, were cleansed with isopropanol.

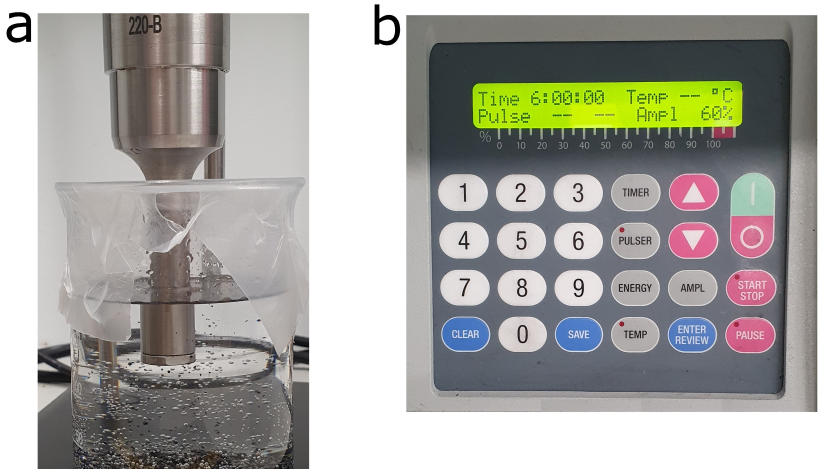

Figure 19: (a) Ultrasonic probe submerged in water prior to exfoliation. (b) Settings for Cole-Parmer 500 W ultrasonic processor.

After LPE, the dispersion was first centrifuged for 1 hour at 4000 rpm with the fixed angle rotor. The sediment was discarded to remove large unexfoliated graphite flakes. The supernatant was used as "stock dispersion".

4.2 Centrifugation of LPE product

The centrifuge used for the experiments is the Hettich Universal 320R combined with the Hettich 1556 fixed angle rotor or the Hettich 1624 swing-out rotor. After centrifugation, the vials were removed from the buckets while attempting to create as little movement as possible. The supernatant was extracted with a pipette. Roughly 3 mm of liquid was left in the vial to ensure that the sediment was not disturbed and redispered into

the supernatant, as seen in Figure 21. The experiments with a fixed-angle rotor are performed at 8000 rpm and the experiments with a swing-out rotor at 4000 rpm, only varying time. The fixed-angle and the swing out rotor are visualized in figure 20. Both rotors were measured and the RCF was calculated: For the fixed angle rotor, $R = 82.5$ mm and $\theta = 35°$; $\Omega = 8000\text{rpm} \times \frac{2\pi}{60\text{seconds}} = 837.8\frac{\text{rad}}{\text{s}}$, then $g_\text{e} = \sin(\theta)R\Omega^2 = 33090$ ms^{-2} and $\text{RCF} = \frac{33090\text{ms}^{-2}}{9.81\text{ms}^{-2}} = 3385$. Similar for the swing out rotor: $R = 121$ mm, $g_\text{e} = \sin(\theta)R\Omega^2 = 21231$ ms^{-2}, which is equivalent to RCF = 2164. One could argue that the particles travel horizontally to the wall of the vial in the case of the fixed angle rotor and that H should be adjusted to the width of the vial, leaving out $\sin(\theta)$. However, the calculation shown above is similar to the calculation by Backes et al., 2016 [19]. Also, this method was used by Acrivos et al., 1979 [49] to calculate the enhanced settling rate, so for comparison with the literature, this way of calculation is used.

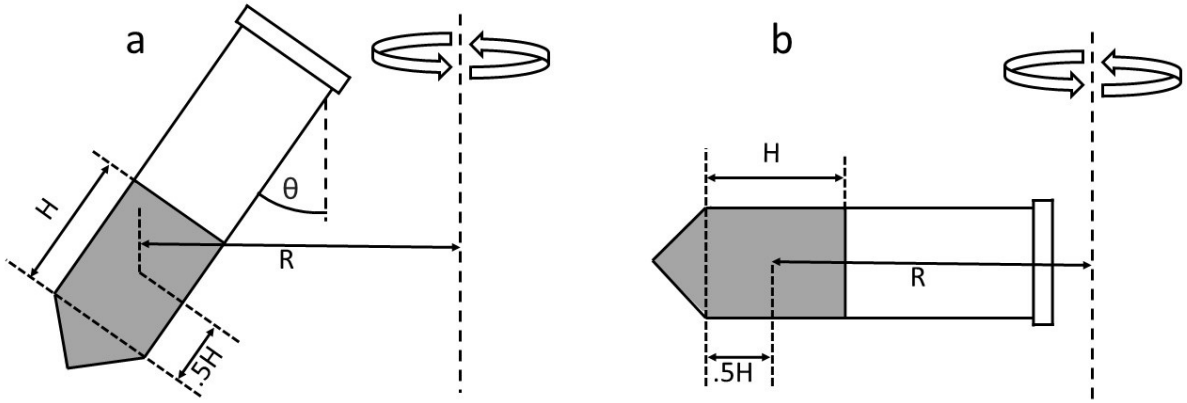

Figure 20: Visual representation of (a) the fixed-angle and the (b) swing out rotor.

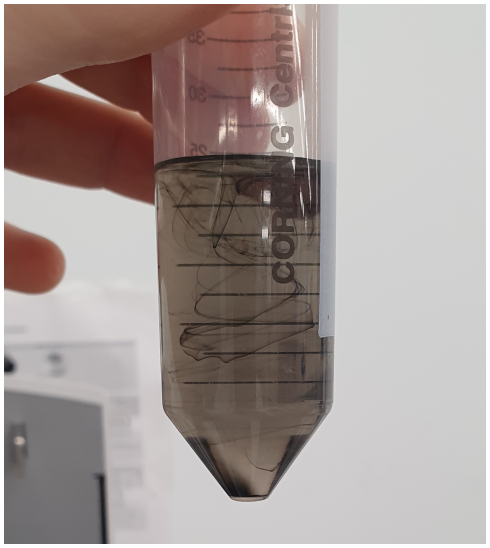

Figure 21: Redispersion of graphene into supernatant.

4.3 UV-Vis spectroscopy

UV-Vis measurements were performed with a Lange DR6000 spectrophotometer. Further equipment that was used is: 2× UV crystal cuvettes, 3× 3 ml disposable pippettes, a 500 ml beaker with dionized water, a 500 ml beaker for waste dispersion, a 50 ml beaker for mixing, isopropanol, a USB-stick, a scale with a 0.01 gram accuracy. The protocol is the following:

1. Plug in the USB-stick spectrophotometer.
2. Turn on spectrophotometer
3. Select the settings: **"Wavelength scan"**, **"10 mm carousel"** and **"Zero cell 1 and read cell 2"**.
4. Cleanse the inside and outside of the cuvettes with isopropanol and wash the isopropanol away with dionized water.
5. Cleanse the pipettes by sucking up dionized water and disposing it in the waste beaker. Each of the pipettes is used for only one purpose. Pipette 1 is used for the dionized water and can be left in the beaker with dionized water, pipette 2 is used for pure graphene dispersion and pipette 3 for diluted graphene dispersion. Ensure that the tips of pipette 2 and 3 are elevated in the air to prevent contamination.
6. Fill one of the cuvettes with dionized water and place it in cell 1 of the carousel. This cuvette will be used as the zeroing cell and does not have to be touched anymore.
7. Wash pipette 2 with the graphene dispersion that is to be investigated. When this dispersion is measured multiple times, this is only required one time.
8. Cleanse the mixing beaker with isopropanol and dionized water and shake off as much water as possible.
9. Place the beaker on the scale and zero it.
10. Use pipette 2 to insert roughly 1 ml of graphene dispersion in the mixing beaker and denote the weight, m_{gra}.
11. Use pipette 1 to insert roughly 2 ml of dionized water in the mixing beaker and denote the weight, m_{water}.
12. Shake the mixing beaker to mix the water and pure dispersion.
13. Wash pipette 3 with the mixture. When this dispersion is measured multiple times, this is only required one time.
14. Wash the empty cuvette with a small amount of the mixture, 0.3 ml is sufficient.

15. Fill the cuvette to at least halfway the height. The diluted dispersion should should have a concentration between the second and third cuvette from the left in Figure 22.

Figure 22: Graphene samples prepared for UV-Vis. Concentration decreasing from left to right.

16. Place the cuvette in cell 2.

17. Select a function where cell 1 is zeroed and cell 2 is read.

18. Perform the wavelength scan.

19. The UV-Vis spectroscopy is now excecuted and saved to the USB.

20. To find the real concentration:

$$c = \frac{m_{\text{gra}}}{m_{\text{water}} + m_{\text{gra}}} \frac{E}{l\epsilon}$$

5. Results and discussion

5.1 Slipping disk model

With the friction data as function of the slip length of an oblate spheroid from Chang and Keh, 2008 and 2011 [71] [70], and a zero thickness disk from Sherwood, 2012 [72], in Section 3.2, we can approximate the friction of a graphene flake as an oblate spheroid with lateral size L, thickness t and slip length b. The friction of a spheroid moving parallel and perpendicular to its axis of symmetry are averaged, as discussed previously:

$$\frac{3}{\langle f \rangle} = \frac{2}{f_\perp} + \frac{1}{f_\parallel} \tag{14}$$

The friction of the spheroid moving parallel to its axis of symmetry is plotted in Figure 23 for various slip lengths. To find the friction for an arbitrary combination of L, t and b, we first interpolate between the values of E in Table 1 to find a new set of friction factors as a function of b. We take $b_{\text{inf}} \approx b_{10}$ and do a second interpolation to find $f_\parallel$. All friction factors diverge towards a constant value for thin disks. When we analyze data from Backes et al., 2016 [13], the particle found with the worst aspect ratio has 10 layers and a lateral size of 30 nm, resulting in $E = \frac{10 \times 0.335\text{nm}}{30\text{nm}} = 0.11$ or $E = 0.2$, when we include the thickness that is added by SC and water from Lin et al., 2011 [39]. All other particles have smaller values of E, meaning that the parallel friction will be $0.81 < f_\parallel < 0.86$, if we assume our LPE product similar to Backes.

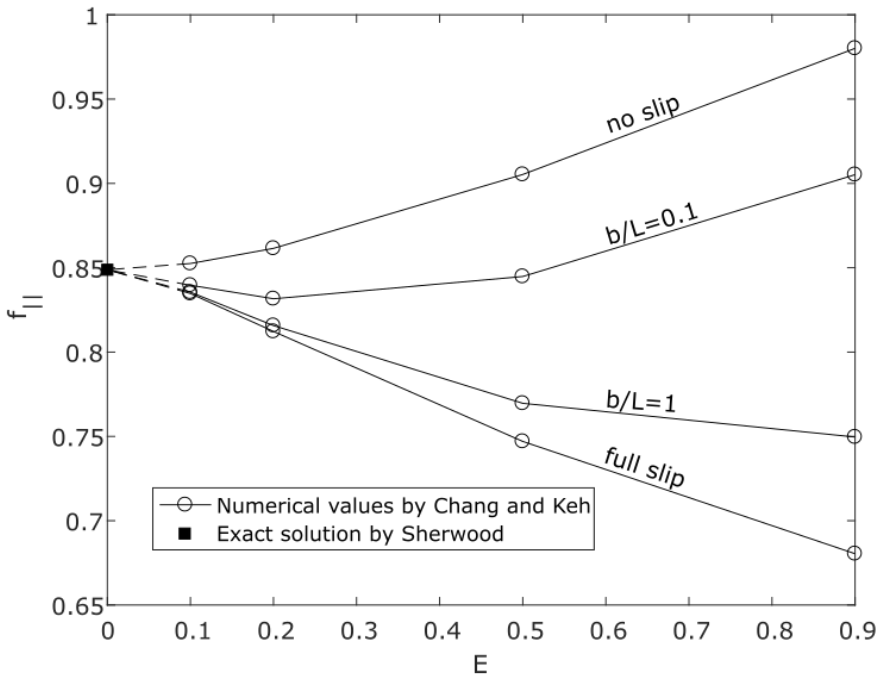

Figure 23: Friction factor of an oblate spheroid moving parallel to its axis of symmetry as a function of the aspect ratio E and relative slip length b/L.

In contrast to parallel motion friction, the speheroid friction moving perpendicular to its axis of symmetry diverges for different slip lengths towards $E \to 0$, as seen in Figure 24.

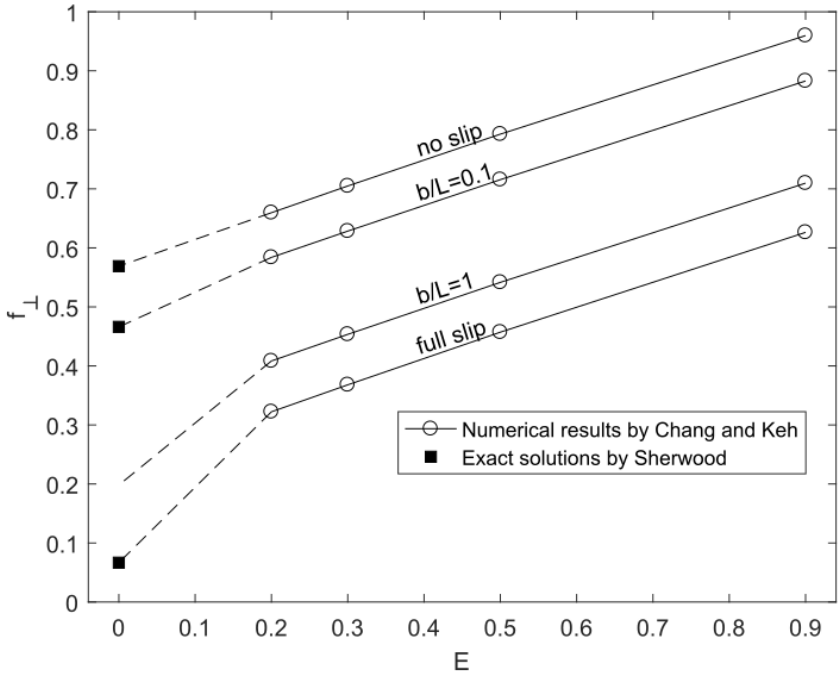

Figure 24: Friction factor of an oblate spheroid moving perpendicular to its axis of symmetry as a function of the aspect ratio E and relative slip length b/L. Note that $f_\perp$ for 'full slip' at $E = 0$ is not actually given for full slip, but for $b/L = 5$

For a particle with $0 \leq E \leq 0.2$, the perpendicular friction varies from $0 \leq f_\perp < 0.67$. Furthermore, the friction of the perpendicular motion weighs twice as much as the parallel motion in Equation 14. It is more difficult to find a good estimate for the perpendicular motion, as the exact solutions from Sherwood, 2012 [72] are only given in the cases $b/L = 1$, $b/L \ll 1$ and $b/L \gg 1$. The perpendicular friction of very thin flakes with a slip in the same order of its lateral size is not defined. To approximate this region, we first look at $f_\perp$ from Keh and Chang, 2011 [71] at set E, as a function of b/L, plotted in Figure 25.

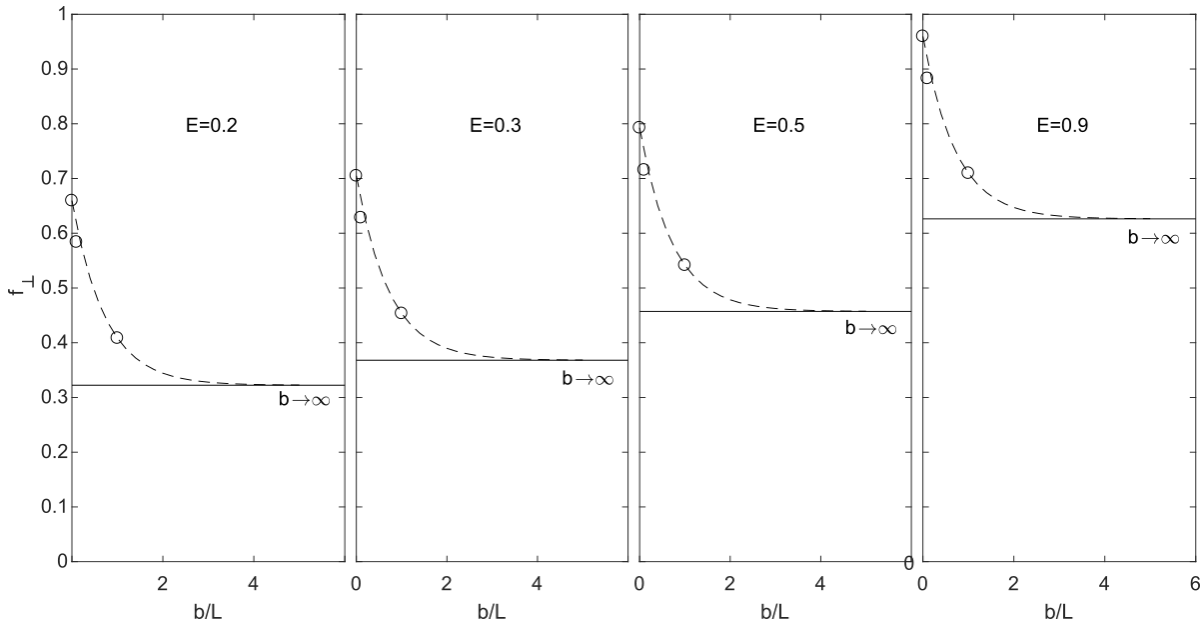

Figure 25: Data points from Keh and Chang [71] of an oblate spheroid moving perpendicular to its axis of symmetry. Friction $f_\perp$ at $b/L = 0$, 0.1 and 1 are shown with circles. The value for $b/L \to \infty$ is plotted as a horizontal asymptote. The fitted functions in the form of $f_\perp = A\ \mathrm{e}^{B\cdot(b/L)} + C$ are plotted as a dotted line.

The values of $f_\perp$ at $b/L = 0$, 0.1, 1 and $b/L \to \infty$, suggest a fit in the form of $f_\perp = A\ \mathrm{e}^{B\cdot(b/L)} + C$, in which A, B and C are constants. The values at $b/L = 0$, 1 and $b/L \to \infty$ are used to fit this equation for each constant of E.

$$B = \log\left(\frac{f_{\perp,b=1} - f_{\perp,b\to\infty}}{f_{\perp,b=0} - f_{\perp,b\to\infty}}\right) \tag{30}$$

$$f_\perp = (f_{\perp,b=0} - f_{\perp,b\to\infty})e^{B(b/L)} + f_{\perp,b\to\infty} \tag{31}$$

These fits are plotted in Figure 25 as dashed lines. We notice that $f_{\perp,b=5} \approx f_{\to\infty}$ for $0.2 \leq E \leq 0.9$. To estimate the value of $f_{\perp,b=1}(E{=}0)$, we take the same ratio as $f_\perp(E{=}0.2)$:

$$f_{\perp,b=1,E=0} = \frac{f_{\perp,b=1,E=0.2} - f_{\perp,b\to\infty,E=0.2}}{f_{\perp,b=0,E=0.2} - f_{\perp,b\to\infty,E=0.2}} \cdot (f_{\perp,b=0,E=0} - f_{\perp,b\to\infty,E=0}) + f_{\perp,b\to\infty,E=0} \tag{32}$$

We can now create a similar fit in the form of Equations 30 and 31. For a particle with $b/L > 5$, we take Sherwood's formula for $b/L \gg 1$. When $b/L < 5$, we use the fitted formula that is plotted in Figure 26 as the dashed line

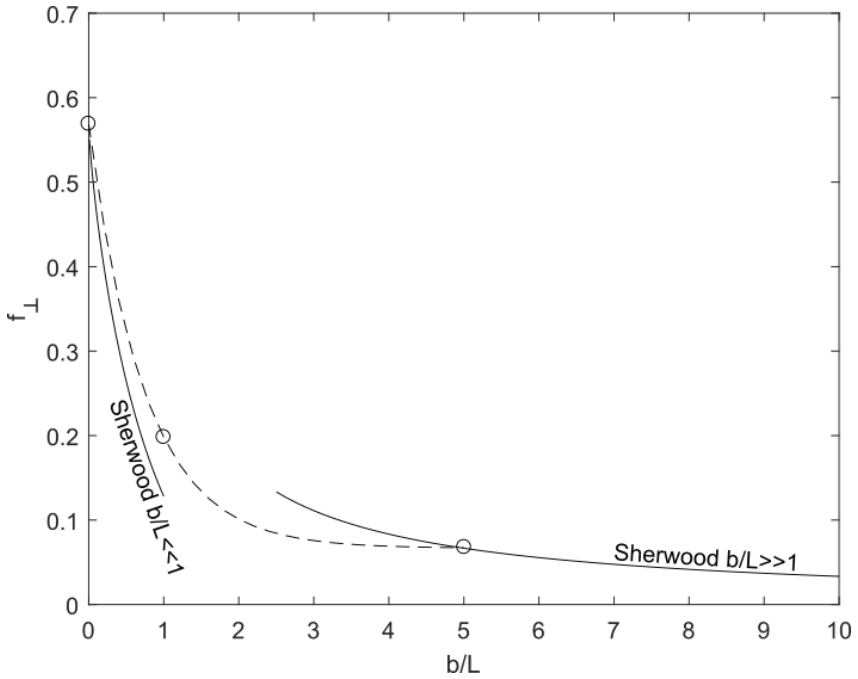

Figure 26: Two solutions of Sherwood at $b/L = 0$ and $b/L = 5$ and the approximated value at $b/L = 1$, marked with circles. The fitted function through these three points is plotted as the dashed line.

To conclude the model, we use the fitted functions to find $f_\perp$ at $E = 0$, $E = 0.2$, $E = 0.3$, $E = 0.5$ and $E = 0.9$ and then we linearly interpolate between these values. Only for particles with $b/L > 5$ and $E < 0.2$, we interpolate between the exact solution from Sherwood for $b/L \gg 1$ and $f_{\perp,b\to\infty,E=0.2}$. Finally, we have found a value for $f_\parallel$ and $f_\perp$ find the average with Formula 14.

To verify the physical plausibility of this model, the friction for a monolayer flake as a function of lateral size and slip length is plotted in Figure 27a. The increased settling velocity is normalized to the no-slip settling velocity $q_{\mathrm{b}=0}$ and displayed in 27b. As expected, friction factors converge to the no-slip value for larger L, as b will become negligible to the the size of the particle. Further, for increasing slip, drag decreases.

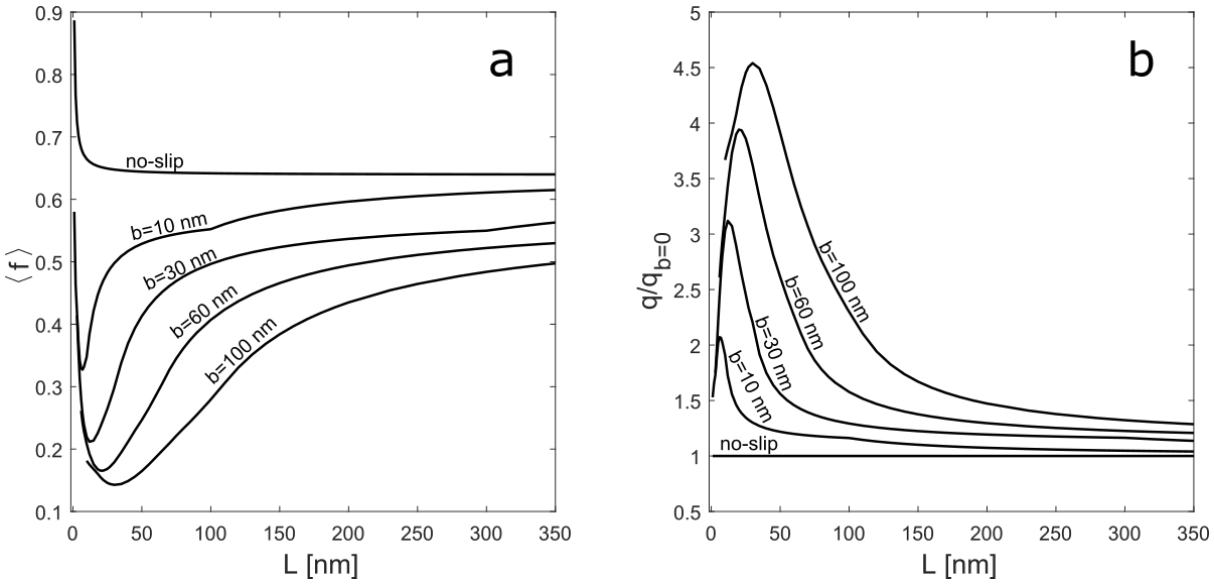

Figure 27: (a) Friction from the slip-model for a monolayer graphene flakes as function of lateral size L and slip length b. (b) Increased settling rate for a monolayer flake due to slip, normalized to no-slip settling velocity $q_{\mathrm{b=0}}$.

5.2 Surfactant models

The encapsulation of graphene by surfactant was discussed in Sections 2.3 and 2.4. Green et al., 2009 [38] assumed almost perfect coverage by SC (94%) and an extremely thick hydration shell of 3 nm per side. In contrast, the molecular simulations by Lin et al., 2011 [39] resulted in uneven coverage of the surfactant with water molecules trapped between cholate ions. The following sections discuss the effect of these the surfactant on the settling velocity.

5.2.1 Cake-model

The settling velocity based on the cake-model by Green is found by plugging in the new value for the density and thickness into the settling velocity (Formula 18), yielding the following expression:

$$q = \frac{\pi g_{\mathrm{e}} L}{27.48\mu} \left[\rho_{\mathrm{gra}} N + 2m_{\mathrm{SC}}\sigma - \rho_{\mathrm{H_2O}}((N+1)t_{\mathrm{gr}} + 2t_{\mathrm{A}})\right] \tag{33}$$

From this formula, we find that the settling velocity is independent of the thickness of the hydration layer $t_{\mathrm{H_2O}}$, which can be explained by the assumption made when deriving the formula for the settling velocity. When we assume that the particles are thin disks, the thickness does not contribute to the drag of the particle; see Formula 16. Since the hydration layer has the same density as the surrounding medium, the buoyancy is equal to the centrifugal force and the terms cancel out. As long as the particles meet the initial condition of $E < 0.25$, the settling velocity of a graphene particle is well approximated by a thin disk. However, the thickness of ML graphene with SC and hydration shell is

7.645 nm, which means that this condition does not hold for ML graphene with a lateral size smaller than 30 nm.

5.2.2 Lin's model

The settling velocity based on molecular simulations by Lin et al., 2011 [39] is found in a similar manner as the cake model and will be referred to as Lin's model. From the molecular simulations, the thickness of a ML graphene layer plus surfactant was found to be $t_{\mathrm{Lin,ML}} = 3$ nm. Assuming that an increase in the number of layers does not affect the binding of cholate ions or water molecules, every additional layer is simply a slab with thickness t_{gra} and density 2160 kg·m^{-3} that is added to an ML flake:

$$\rho_{\mathrm{Lin}} = \frac{\rho_{\mathrm{Lin,ML}} t_{\mathrm{Lin,ML}} + \rho_{\mathrm{gra}}(N-1)t_{\mathrm{gra}}}{t_{\mathrm{Lin,ML}} + (N-1)t_{\mathrm{gra}}} \tag{34}$$

Then, from the density and thickness $t_{\mathrm{Lin,ML}} + (N-1)t_{\mathrm{gra}}$, we find the settling velocity:

$$q = \frac{\pi g_{\mathrm{e}} L}{27.48\mu} \left[(\rho_{\mathrm{Lin,ML}} - \rho_{\mathrm{H_2O}}) t_{\mathrm{Lin,ML}} + (\rho_{\mathrm{gra}} - \rho_{\mathrm{H_2O}})(N-1)t_{\mathrm{gra}} \right] \tag{35}$$

5.2.3 Comparison between the simple, cake- and Lin's model

For a graphene flake in water without surfactant, the settling velocity is given by Formula 18, with $t = N t_{\mathrm{gra}}$. We can compare this simple approximation with the cake-model and Lin's model. The settling velocity for a flake with a lateral size of 100 nm and varying layer number is plotted in Figure 28. The following values are taken for the constants: $\mu = 1$ mPa·s, $\rho_{\mathrm{gra}} = 2260$ kg·m^{-3}, which is simply the density of graphite,

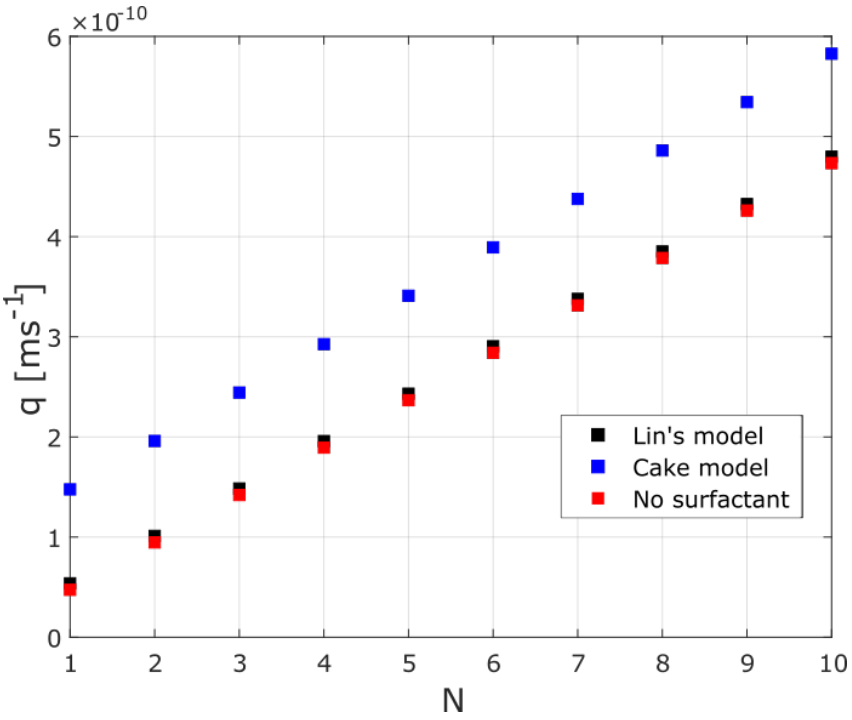

Figure 28: Comparison between the two models for a graphene disk that incorporate surfactant in the settling velocity and a thin disk without surfactant at 1 RCF.

From Figure 28, we learn that the settling velocity shows a linear dependence on the layer number for each model. Also, Lin's model and the simple method result in nearly equal settling velocities. This is a surprising result, as cholate molecules, having a higher density than water, attach to the graphene surface and would intuitively increase settling velocity. The reason for this not being the case can be explained by Figure 4, where we observe water and surfactant molecules not being present from $-0.25 < z < 0.25$ nm. This absence of molecules suggests an effective ML graphene thickness of 0.5 nm instead of the commonly used interlayer distance of 0.335. This increased thickness causes a slightly lower density overall and, by coincidence, causes the Lin's model and the no surfactant settling velocity to yield almost identical values for q.

5.3 Size estimation by simulation

This section describes a method that is developed to find the distribution of polydispersed 2D nanoparticles in a dispersion without the need of extensive AFM or TEM analysis. The method uses:

1. Experimental data of concentration in the supernatant over time during centrifugation.

2. Simulations of the graphene concentration in the supernatant.

During centrifugation, graphene particles transfer from the supernatant to the sediment, thus the graphene mass in the supernatant decreases over time, which can be measured

by UV-Vis spectroscopy. Although the exact distribution of particles is unknown prior to centrifugation, we can simulate many different distributions of N and L to find which are viable with the experimental data.

5.3.1 Simulation principle

Homogeneous (HC) and band centrifugation (BC) experiments are simulated in MATLAB. The input that is required is: n, μ_{L}, μ_{N}, σ_{L}, σ_{N}, H, T and RCF. From these parameters, n particles are generated, where the particle i is given random dimensions L_i and N_i resulting from log-normal distributions for lateral size and thickness with μ_{L}, μ_{N}, σ_{L} and σ_{N}. per particle, the settling velocity q_i is calculated. Additionally, each particle is given a random height h_i between 0 and H for HC and between xH and H for BC. Time T and RCF are chosen and experiments can be replicated. When a particle i with

$$q_i(\mathrm{RCF}, L_i, N_i) > \frac{h_i}{T}, \tag{36}$$

It reaches the sediment, and otherwise it will remain in the supernatant. When we assume the simplest case where N and L are independent, there is a no-slip condition and the surfactant does not increase the settling velocity, q will be log-normally distributed as well. We choose a centrifugation time and RCF and replicate an experiment. Then the simulation will give us the distribution in the SN and SD. An example of HC is shown in Figure 29.

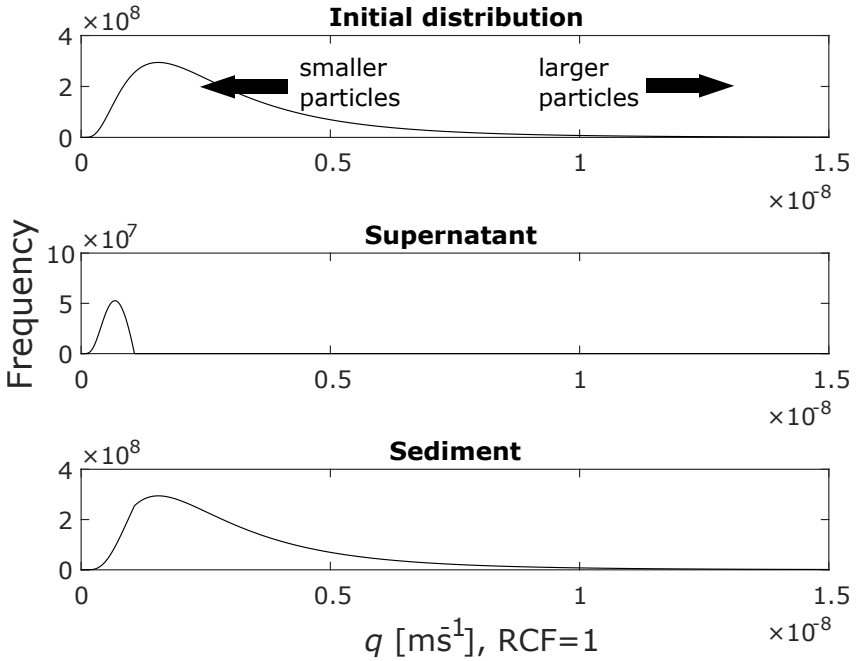

Figure 29: Example of settling velocity distribution before centrifugation (upper) and the resultant supernatant (middle) and sediment (lower) after simulation of homogeneous centrifugation experiment.

With these simulations, the mass can be tracked as well. From the assumption of the particles being thin disks, the mass of particle i is $m_i = \frac{\pi}{4} L_i^2 N_i t_{\mathrm{gra}}$ and thus the mass of all generated graphene particles is:

$$m_{\mathrm{total}} = \sum_{i=1}^{n} m_i = \sum_{i=1}^{n} \frac{\pi}{4} L_i^2 N_i t_{\mathrm{gra}} \tag{37}$$

From the total amount of particles, n_{SN} particles remain in the supernatant after centrifugation. Thus, the mass that is left in the supernatant (SN) is:

$$m_{\mathrm{SN}} = \sum_{i=1}^{n_{\mathrm{SN}}} m_{i,\mathrm{SN}} = \sum_{i=1}^{n_{\mathrm{SN}}} \frac{\pi}{4} L_{i,\mathrm{SN}}^2 N_{i,\mathrm{SN}} t_{\mathrm{gra}} \tag{38}$$

The mass fraction that remains in the supernatant is $m_{\mathrm{SN}}/m_{\mathrm{total}}$. Note that this is not equal to n_{SN}/n, as particles have different masses.

5.3.2 Combining simulations and experimental concentration measurements to estimate initial distributions

The concentration is related to the extinction found by UV-Vis measurements, as explained in Section 2.6.3. However, the extinction coefficient ε ranges from 1390 to 6600 $\mathrm{L{\cdot}g^{-1}{\cdot}m^{-1}}$ in the literature, which means that the absolute concentration cannot be determined. Yet, it is possible to determine the relative concentration between samples as the length l of the cuvette and the extinction coefficient ε_{660} remain constant in the Lambert-Beer equation. We can measure the post-centrifugation concentration in the supernatant relative to the concentration of the stock dispersion:

$$E = \varepsilon c l \tag{3}$$

$$\frac{c_1}{c_{\mathrm{stock}}} = \frac{E_1}{E_{\mathrm{stock}}} \tag{39}$$

As the concentration is measured in mass per unit volume, we can precisely determine the mass fraction left in the supernatant after centrifugation.

The UV-Vis measurements in combination with simulations allow us to estimate the initial values of μ_{L}, μ_{N}, σ_{L} and σ_{N}. Based on graphene particle sizes in the literature, we chose a range for these four parameters. For example: $\mu_{\mathrm{L}} = [-13.80\ ;\ -16]$, $\mu_{\mathrm{N}} = [0\ ;\ 2.5]$, $\sigma_{\mathrm{L}} = [0.3\ ;\ 1.3]$ and $\sigma_{\mathrm{N}} = [0.3\ ;\ 1.3]$. We choose 11 intervals for each parameter range with linearly equally spaced values resulting in $11^4 = 14631$ combinations:

$\boldsymbol{\mu_{\mathrm{L}}}$	$\boldsymbol{\mu_{\mathrm{N}}}$	$\boldsymbol{\sigma_{\mathrm{L}}}$	$\boldsymbol{\sigma_{\mathrm{N}}}$	**Exp(L)**	**Exp(N)**
-13.8	0	0.3	0.3	1062 nm	1.05
-13.8	0	0.3	0.4	1062 nm	1.08
-13.8	0	0.3	0.5	1062 nm	1.13
⋮	⋮	⋮	⋮	⋮	⋮
-13.8	0	0.3	1.3	1062 nm	2.33
-13.8	0	0.4	0.3	1100 nm	1.05
-13.8	0	0.4	0.4	1100 nm	1.08
⋮	⋮	⋮	⋮	⋮	⋮
-13.8	0	0.4	1.3	1100 nm	2.33
-13.8	0	0.5	0.3	1151 nm	1.05
⋮	⋮	⋮	⋮	⋮	⋮
-13.8	0	1.3	1.3	2364 nm	2.33
-13.8	0.25	0.3	0.3	1062 nm	1.34
⋮	⋮	⋮	⋮	⋮	⋮
-16	2.5	1.3	1.3	262 nm	28.4

These combinations are distributions of particle dimensions. For each of these combi-

nations, a set of simulations is performed corresponding to the experiments. The resulting mass fraction left in the supernatant will be compared to the corresponding concentration from the experiment. If the resultant mass fractions from the simulations for a certain combination lie between the error bars of the relative concentration of the experiments, the combination passes the filter. If not, the combination will be considered impossible. The result is a reduced matrix of possible combinations of the four parameters. Other filters, such as aspect ratio, can be considered to further narrow down the selection of possible combinations.

5.3.3 Incorporation of surfactant and slip

The space of possible combinations of μ_{L}, μ_{N}, σ_{L} and σ_{N} depends on the assumptions made: What is q for a given N and L? As discussed in previous sections, surfactant and slip may increase the settling velocity. The models that are created and discussed in Sections 2.3 and 5.1 can be used to repeat the simulations that are discussed previously, but with the incorporation of slip and/or surfatant.

5.3.4 Incorporation of correlation

Additionally, the assumption of L and N being completely independent is most likely not realistic. When comparing the scatterplots of N vs. L from [13] and [20] to N and L being independently generated in Figure 30, one observes that there is a slight correlation between N and L, that is, the chance of a particle having an area $\sqrt{L_m W_m} > 0.1$ μm^2 is significantly larger for a particle with 10 layers than for a monolayer flake. The datapoints from [20] are distinguishable, and their value is extracted with WebPlotDigitizer. The correlation between layer number and area is $\rho_{\mathrm{N,Area}}$=0.2902. The correlation between layer number and lateral size is $\rho_{\mathrm{N,L}}$=0.3502.

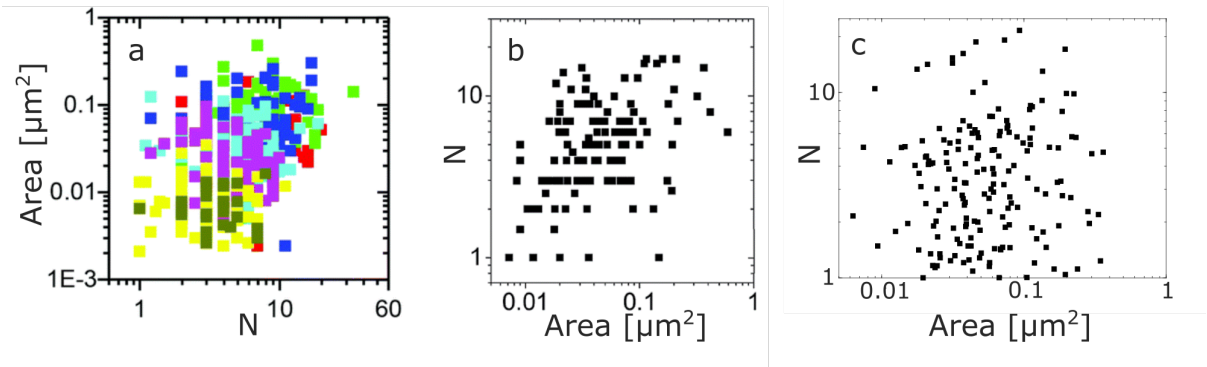

Figure 30: Dimensions of individual particles from AFM data from (a) Backes et al., 2016 [13] and (b) Varrla et al., 2014 [20] and (c) 200 log-normal randomly generated particles with $\mu_{\mathrm{L}} = 15.3$, $\mu_{\mathrm{N}} = 0.98$, $\sigma_{\mathrm{L}} = 0.4$ and $\sigma_{\mathrm{N}} = 1$.

To generate n particles with dimensions N and L and correlation $\rho_{\mathrm{N,L}}$, we create matrix a M in which the first column exists of normally distributed realisations with μ_{N}

and σ_{N} and the second column exists of normally distributed realisations with μ_{L} and σ_{L}:

$$\mathbf{M}_1 = \mathcal{N}(\mu_{\mathrm{N}}, \sigma_{\mathrm{N}}) \tag{40}$$

$$\mathbf{M}_2 = \mathcal{N}(\mu_{\mathrm{L}}, \sigma_{\mathrm{L}}) \tag{41}$$

$$\mathbf{M} = [\mathbf{M}_1\ \mathbf{M}_2] \tag{42}$$

Note that taking the exponent of the individual values in M would result in n particles with uncorrelated dimensions. $\mathbf{M}$ is multiplied by the Cholesky decomposition of the correlation matrix $\mathbf{R}$, $\mathbf{L}$. The exponent is takes of $\mathbf{M}{\cdot}\mathbf{L}$ to create particle dimensions.

$$\mathbf{L} = \mathrm{Chol}(\mathbf{R}) = \mathrm{Chol}(\begin{bmatrix} 1 & \rho \\ \rho & 1 \end{bmatrix}) = \begin{bmatrix} 1 & \rho \\ 0 & \sqrt{1-\rho^2} \end{bmatrix} \tag{43}$$

$$[\mathbf{N}\,\mathbf{L}] = \exp(\mathbf{M}{\cdot}\mathbf{L}) = \exp(\begin{bmatrix} \mathrm{M}_{11} & \mathrm{M}_{12} \\ \mathrm{M}_{21} & \mathrm{M}_{22} \\ \mathrm{M}_{31} & \mathrm{M}_{32} \\ \vdots & \vdots \\ \mathrm{M}_{\mathrm{n}1} & \mathrm{M}_{\mathrm{n}2} \end{bmatrix} \begin{bmatrix} 1 & \rho \\ 0 & \sqrt{1-\rho^2} \end{bmatrix}) = \exp \begin{bmatrix} \mathrm{M}_{11} & \rho\mathrm{M}_{11} + \sqrt{1-\rho^2}\mathrm{M}_{12} \\ \mathrm{M}_{21} & \rho\mathrm{M}_{21} + \sqrt{1-\rho^2}\mathrm{M}_{22} \\ \mathrm{M}_{31} & \rho\mathrm{M}_{31} + \sqrt{1-\rho^2}\mathrm{M}_{32} \\ \vdots & \vdots \\ \mathrm{M}_{\mathrm{n}1} & \rho\mathrm{M}_{\mathrm{n}1} + \sqrt{1-\rho^2}\mathrm{M}_{\mathrm{n}2} \end{bmatrix} \tag{44}$$

Here, the input parameter ρ is not equal to the correlation factor ρ_{NL}. After generating the particles, $\rho_{\mathrm{N,L}}$ can be found with the formula 28. Moreover, the expected value of L $E(L) \neq \exp(\mu_{\mathrm{L}} + \sigma_{\mathrm{L}}^2/2)$, however, $E(N) = \exp(\mu_{\mathrm{N}} + \sigma_{\mathrm{N}}^2/2)$. Besides the four parameters μ_{L}, μ_{N}, σ_{L} and σ_{N}, a fifth parameter, ρ will be added, to find the difference in of the initial distribution for increased correlation. A visualization of different degrees of correlation is shown in Figure 31.

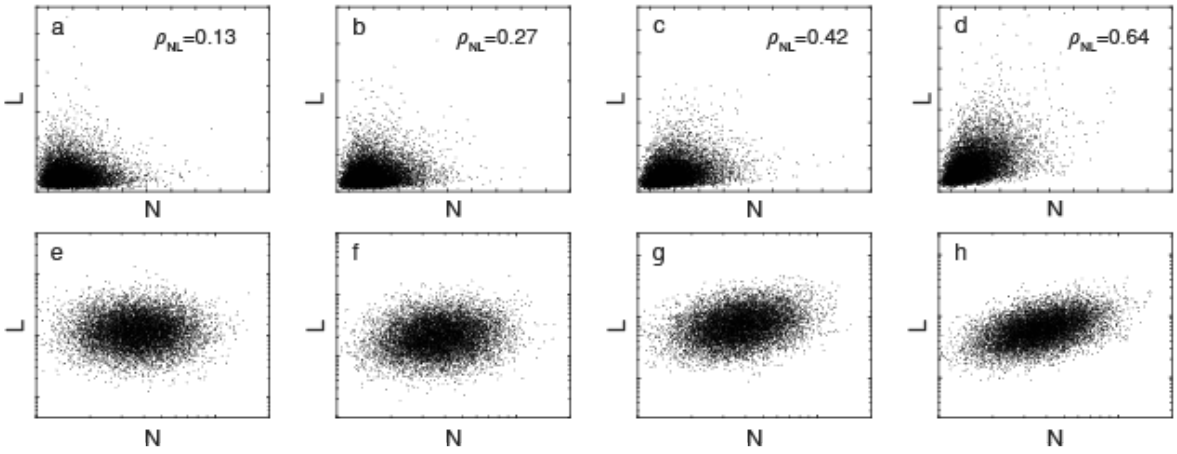

Figure 31: Examples of 10000 particles generated with increasing degree of correlation. Figure (a), (b), (c) and (d) are plotted on double linear scale. Figure (e), (f), (g) and (h) are the respective corresponding plots on double logarithmic axis.

5.4 LPE product and UV-Vis characterization of graphene

With the production method discussed in Section 4.1, graphene was successfully produced using ultrasonication in an aqueous solution. To prove the presence of graphene, the UV-Vis spectrum was found and shown in Figure 32. The π-π^* extinction peak, found at $\lambda = 269$ nm, is $E_{\max} = 11.77$ and $E_{550} = 4.00$, resulting in a average layer number of $\langle N \rangle = (\frac{1}{0.2691} \frac{E_{550}}{E_{\max}}^{1/0.3010}) = 2.18$ layers, based on the data by C. Backes, from Figure 10 in Section 2.6.3. An average layer number of $\langle N \rangle = 2.18$ is relatively small, when comparing to the literature: Although Ogilvie et al., 2019 [19] sonicated for an equal period of time and intensity, the particles found by Ogilvie are significantly larger. Two possible explanations are (1) the usage of pulsation by Ogilvie instead of continuous sonication, causing the netto exfoliation time to be shorter, (2) the use of a larger beaker by Ogilvie, causing for lower energy input per unit volume.

The extinction at $\lambda = 660$ nm was found to be $E_{660} = 3.65$. Assuming $\epsilon = 2322$ L·g·$^{-1}$m^{-1}, the concentration is 0.15 g·L^{-1}.

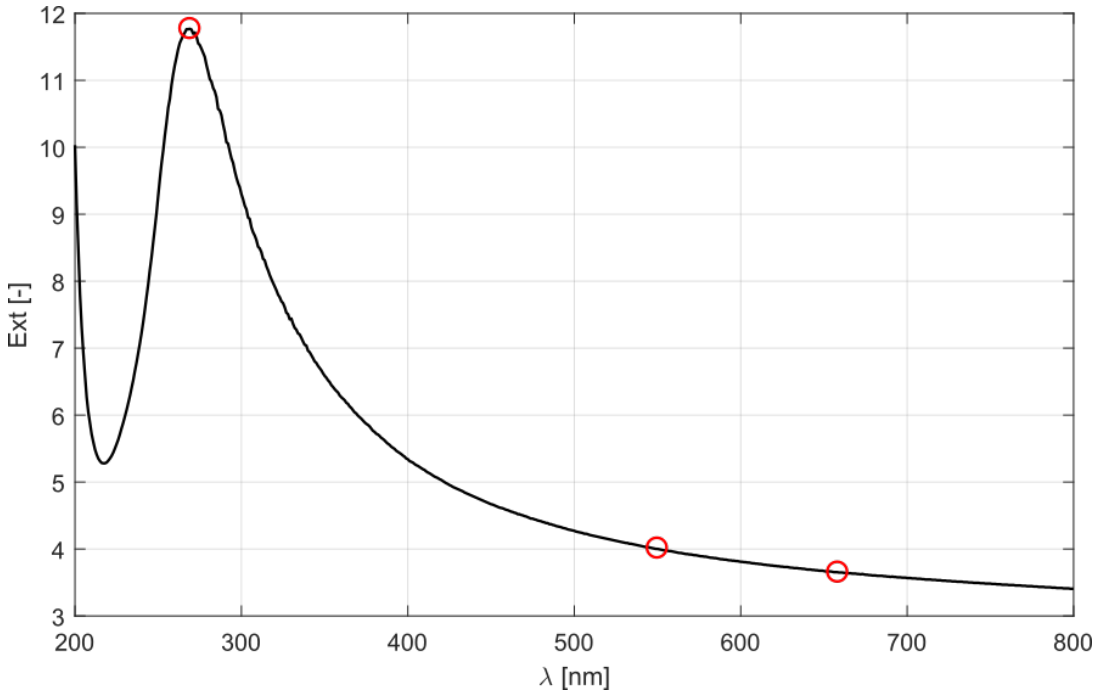

Figure 32: UV-Vis spectrum of the stock graphene dispersion with the π-π^* peak at 269 nm.

Further characterization was done by rheology experiments with 50 mm parallel plates. The shear stress τ versus shear rate $\dot{\gamma}$ and ensuing viscosity μ are plotted in Figure 33, for stock graphene dispersion and pure water, for comparison. Both the dispersion and water show deviating shear stress and viscosity for $\dot{\gamma} < 20$ s^{-1}, but coincide after this value. Since the viscosity of water is known to be $\mu_{\text{water}} = 1$ mPa·s, and this value is confirmed with the measurements for $\dot{\gamma} > 20$ s^{-1}, we can conclude that the deviating values are measurement errors and assume that the graphene measurements are also reliable for $\dot{\gamma} > 20$ s^{-1} and, thus $\mu_{\text{gra}} = 1$ mPa·s. From this, we conclude that the the system is well below the critical volume fraction ϕ_c, at which graphene flakes from joints, which was discussed in Section 3.1.1. This result was also expected from the concentration, since the critical volume fraction found by Barwich et al., 2015 [63] is $c_c = 4.2$ g·L^{-1}, 30 times higher than our stock dispersion.

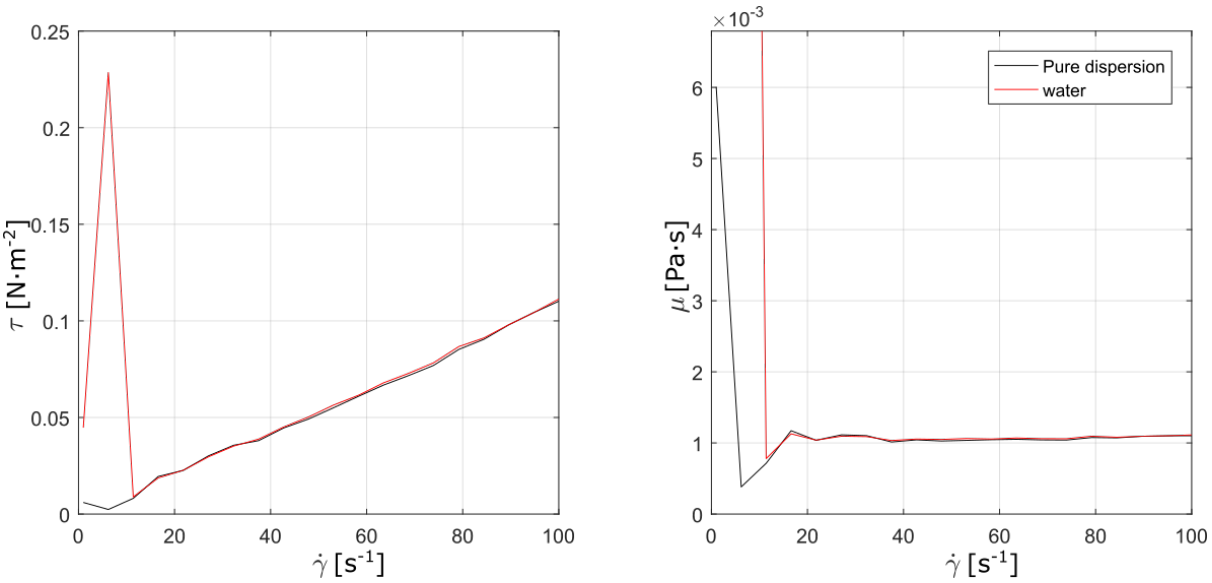

Figure 33: Rheology measurements for pure stock dispersion (S0) and pure water. Shear rate $\dot{\gamma}$ versus shear stress τ is shown on the left and shear rate $\dot{\gamma}$ versus viscosity μ is shown on the right.

5.5 Mass transfer and size decrease in supernatant

To use the initial size estimation method discussed in Section 5.3, we need to find the concentration in the supernatant versus the centrifugation time, which can be interpreted as the mass transfer from supernatant to sediment. The stock dispersion was centrifuged for $\frac{1}{2}$, 1, 2, 3, 5 and 14 hours at 2164 RCF, with a swing-out rotor. The average and error bars of six measurements were taken per data point. Since the distance traveled by a particle scales linearly with both RCF and time, i.e. 10 hours of centrifugation at 1 RCF yields the same result al 1 hour at 10 RCF, the x-axis is given as time×RCF in hours. The concentration versus time×RCF is shown in Figure 34a, where a smooth decline in concentration is observed, with narrow error bars, indicating that accurate measurements were taken. Further insight is given by the average layer number $\langle N \rangle$ versus time×RC, where we find the layer number to decrease from 2.1 to 1.35 layers. Naturally, the minimum layer number is 1 layer, but centrifugation time was not long enough to approach this asymptote.

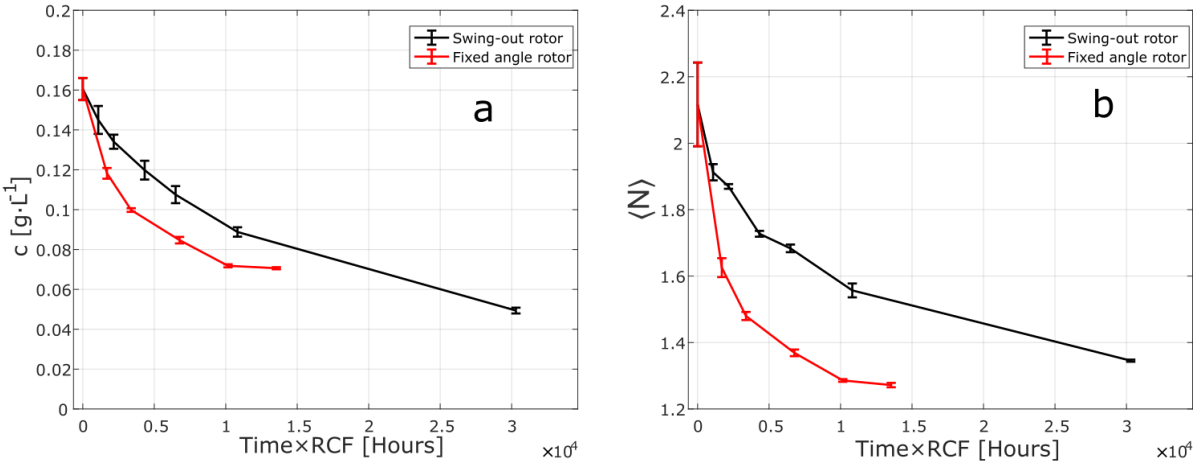

Figure 34: Concentration (ϵ_{660}=2322 $\mathrm{Lg^{-1}m^{-1}}$) versus time×RCF (a) and $\langle N \rangle$ versus time×RCF (b) for experiments with a swing-out rotor and fixed angle rotor.

5.6 Swing-out and fixed angle rotor comparison

As mentioned in Section 2.5.2, an increased sedimentation rate is present when the vial is at an angle with the centrifugal force. To find the increased settling rate, centrifugation experiments were performed with a fixed angle rotor and compared to the data of the swing-out rotor. The result is plotted in Figure 34. One notable phenomenon is the discrepancy in the increased rate for concentration and layer number. The concentration decreases 1.3 to 2 times faster and the extinction ratio 2 to 4 four times. This difference suggests that the thinner particles are more likely to remain in the supernatant with a fixed angle rotor than while using a swing out rotor. This result is remarkable, as there is a mechanism present, while using a swing out rotor, that selects particles based on their thickness N and not on their sedimentation rate, which scales with NL.

5.7 Diluteness determination method

Volume fraction and viscosity provide some information about the rate of diluteness, but no definite conclusions about the rate of hindrance can be drawn from those variables. A new method is developed to determine the system being in the dilute limit or not. It is based on the following principles:

1. As large particles settle faster than small particles, the average particle size in the supernatant decreases during centrifugation, thus the average particle thickness $\langle N \rangle$ decreases as well. (The decrease in $\langle N \rangle$ is seen in Figure 34b)

2. When the particles are hindered, the decrease in $\langle N \rangle$ is slowed down, since the sedimentation process overall is slowed down.

These principles are illustrated in Figure 35, in which System A is the unhindered case, where the layer number decreases from $\langle N \rangle = 10$ to $\langle N \rangle = 2$ after 10 hours of

centrifugation. System B, C and D are examples of increasing hindered cases, where D is hindered the most.

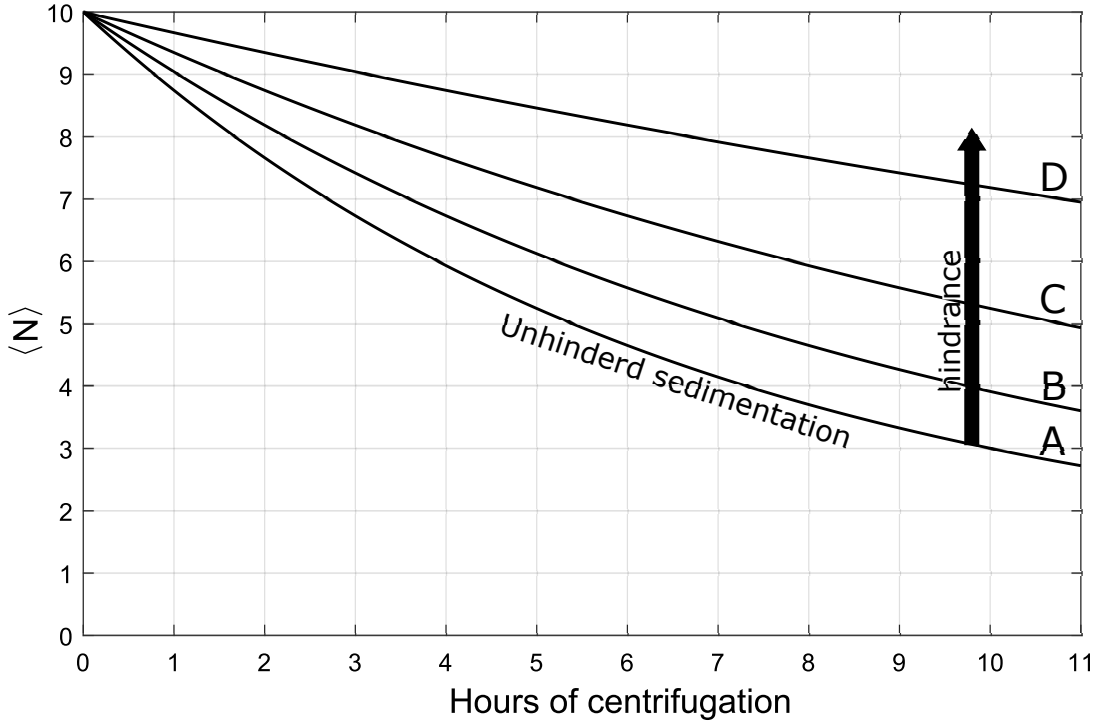

Figure 35: Illustration for the decrease in layer number $\langle N \rangle$, for the dilute/unhinderd System A and for the hindered Systems B, C and D.

For System D, particles are hindered by other particles, so when System D is diluted, the particles would be able to sediment more freely and the layer number decreases faster during centrifugation, towards System A, B or C.

System A is already in the dilute limit, i.e. particles are unhindered, meaning that diluting A would not result in a faster layer number decrease.

Concluding, the system being in the dilute limit or not can be determined by centrifuging the system, upon which the layer number decrease is measured. Then, the system should be diluted sufficiently, and the centrifugation experiment is repeated (equal time and RCF). If one observes the layer number in the SN to be lower for the diluted case than for the pure system, the sedimentation rate is increased and system is **not in the dilute limit**. However, when the layer number is found to be equal for the pure and for the diluted system, then the sedimentation rate is not increased and the system is **in the dilute limit**.

5.8 Determination of the dilute regime

The method discussed in the previous section will be applied to our stock dispersion. The stock dispersion, which can be seen as the top right sample in Figure 36, called 'pure dispersion', has a concentration of 0.1 g·L^{-1} and was centrifuged for two hours at 4000

rpm. We find that $\langle N \rangle$ decreases from 1.9 to 1.5 layers. Four more samples were made from the stock dispersion by adding varying amounts of water. The top left sample is $\frac{1}{16}$ stock dispersion and $\frac{15}{16}$ water. This sample was centrifuged for two hours at 4000 rpm as well, and we find the layer number to decrease to the exact same value as the stock dispersion. When comparing to the examples in the previous section, the conclusion can be drawn that the system is indeed dilute.

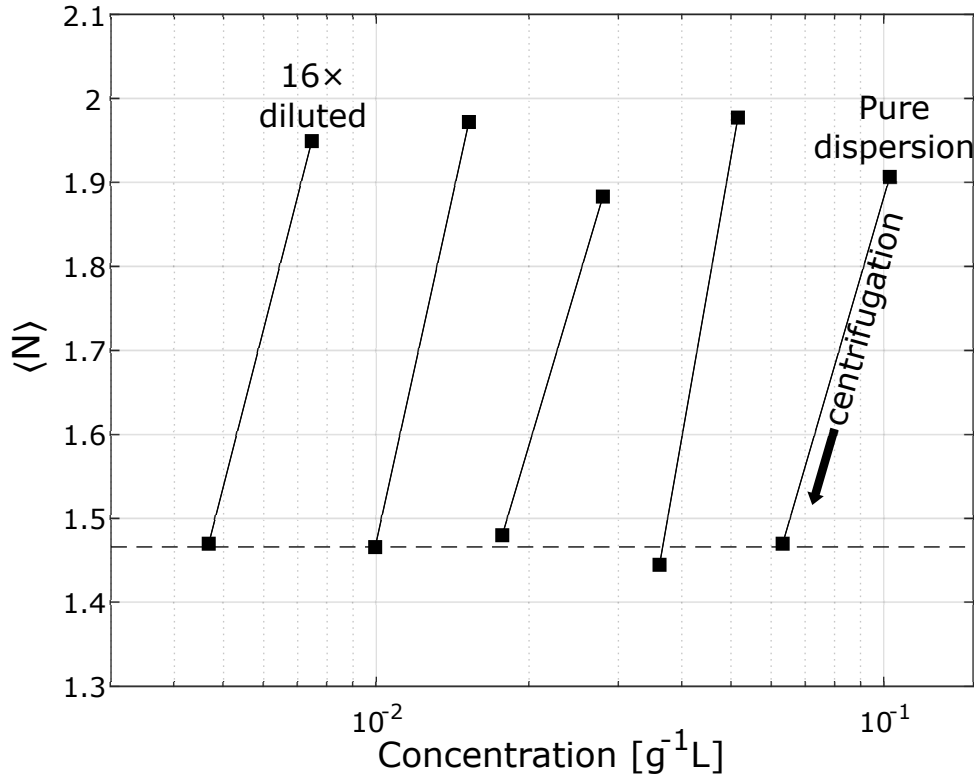

Figure 36: The concentration (ϵ_{660}=2322 $\mathrm{Lg^{-1}m^{-1}}$) versus $\langle N \rangle$ after centrifugation for decreasing concentrations.

By means of clarification, the same plot is made with arbitrary numbers to illustrate the case where a hindered system was diluted and centrifuged and is shown in Figure 37. In this figure we see that all samples have equal $\langle N \rangle$ prior to centrifugation, but the decrease in $\langle N \rangle$ is larger due to the increased sedimentation rate.

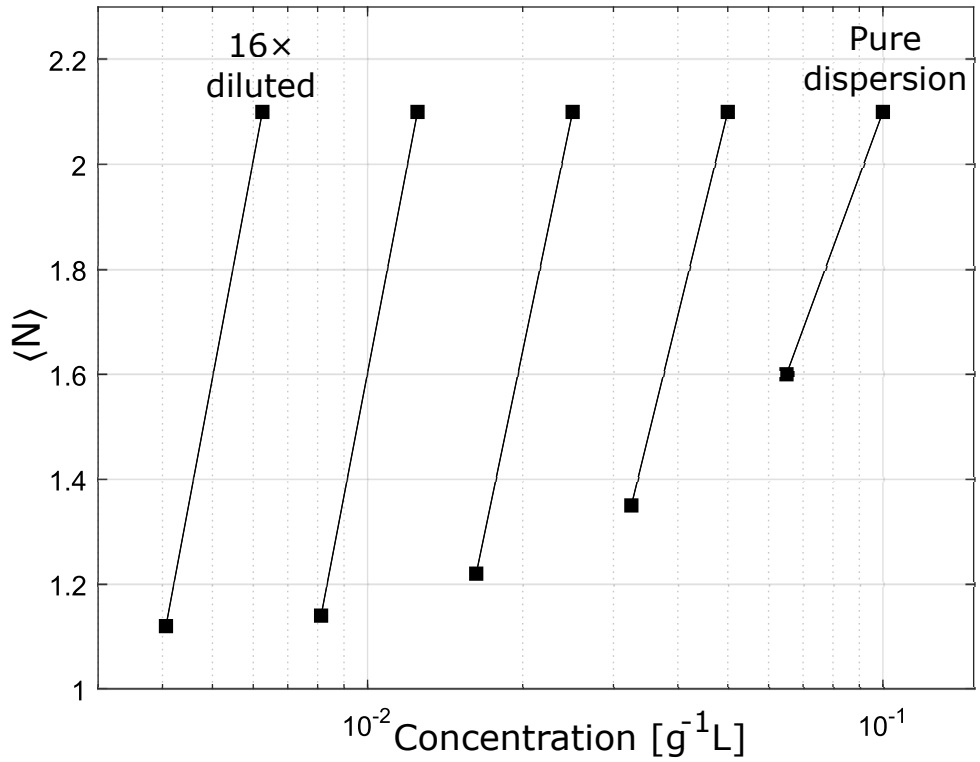

Figure 37: Example of an hindered system that is centrifuged and diluted.

5.9 Fitting of initial distributions to concentration experiments

The data of the concentration versus time × RCF data for the swing-out rotor was used to estimate the initial distribution of particles following the method described in Section 5.3. As mentioned, in the most simple case, the assumptions state no-slip, no influence by surfactant and no correlation between N and L. To find the space for these assumptions, the parameters were first set to the following ranges: $\mu_{\mathrm{L}} = [-19\ ;\ -14]$, $\mu_{\mathrm{N}} = [0\ ;\ 2]$, $\sigma_{\mathrm{L}} = [0.3\ ;\ 1.3]$ and $\sigma_{\mathrm{N}} = [0.3\ ;\ 1.3]$. This set of parameter ranges results in extreme values for the lateral size and layer number: $E(L)= [5\ ;\ 2000]$ nm and $E(N)= [1\ ;\ 17]$ layers. These ranges are used for exploring more precise parameter ranges. Exactly 15,000 combinations were simulated with 200,000 particles per simulation to find their mass fraction after 0.5, 1, 2, 3, 5 and 14 hours of centrifuging, corresponding with the experimental data in Figure 34. The combinations with mass fractions found by simulation that are within the error of the mass fractions from all experiments, shown in Table 4, pass the **first filter**. In Figure 38a, the expected values of all the simulated combinations are plotted. In Figure 38b-38e, we observe how the first filter leaves less combinations viable when more mass fractions from experimental data are taken into account. The combinations that pass the full first filter are shown in 38e.

C. Backes et al., 2019 [19] found that the average aspect ratio of LPE graphene was $L/t = \sqrt{L_m W_m}/t = 103.3$ on average, with negligible deviation for different sizes of

particles. For this reason, we pose a **second filter**, where only combinations pass with an average aspect ratio between 50 and 250, as shown in Figure 38f.

Hours	**Min. mass frac. [%]**	**Max mass frac. [%]**
.5	83.1	98.1
1	78.3	89.0
2	69.3	80.1
3	62.1	72.3
5	51.8	58.7
14	28.9	32.9

Table 4: The maximal and minimal mass fraction left in the supernatant after a given time of centrifugation at 2164 RCF.

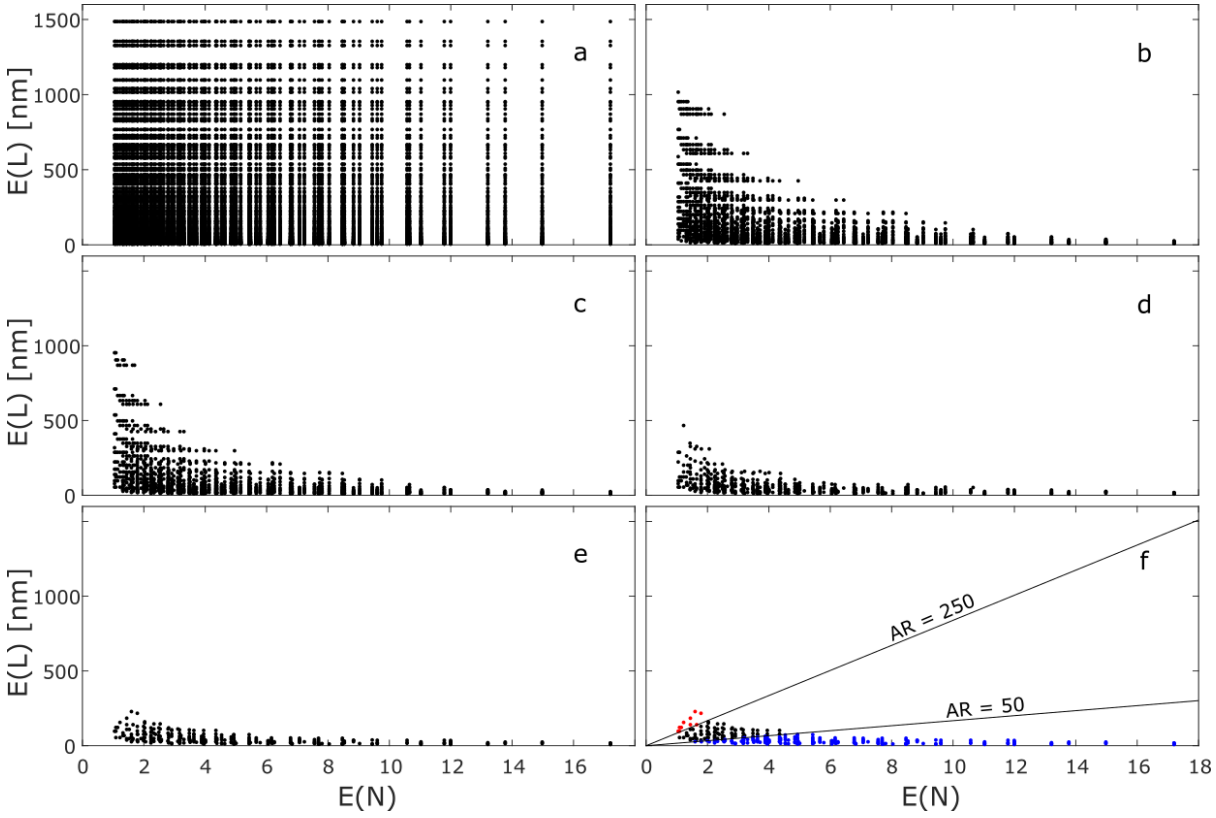

Figure 38: (a) Expected values $E(N)$ and $E(L)$ of all simulated combinations of μ_{L}, μ_{N}, σ_{L} and σ_{N}. (b) All combinations of which the simulated mass fractions correspond with experimental data of 0.5 hours and 1 hours of centrifugation from Table 4. (c) All combinations corresponding with 0.5, 1, 2 and 3 hours of centrifugation. (d) All combinations corresponding with 0.5, 1, 2, 3 and 5 hours of centrifugation. (e) All combinations that pass the first filter. (f) All combinations that pass the first and second filter.

Based on the two filters discussed previously, a second simulation is run with a new, more precise set of parameters : $\mu_{\mathrm{L}} = [-18\ ;\ -15.5]$, $\mu_{\mathrm{N}} = [0\ ;\ 1]$, $\sigma_{\mathrm{L}} = [0.3\ ;\ 1.3]$

and $\sigma_N = [0.3 ; 1.3]$ with a resolution of 14 intervals per parameter, resulting in 38.461 combinations. From these combinations, 1330 passed the mass fraction filter and 827 combinations pass the aspect ratio filter shown in Figure 39.

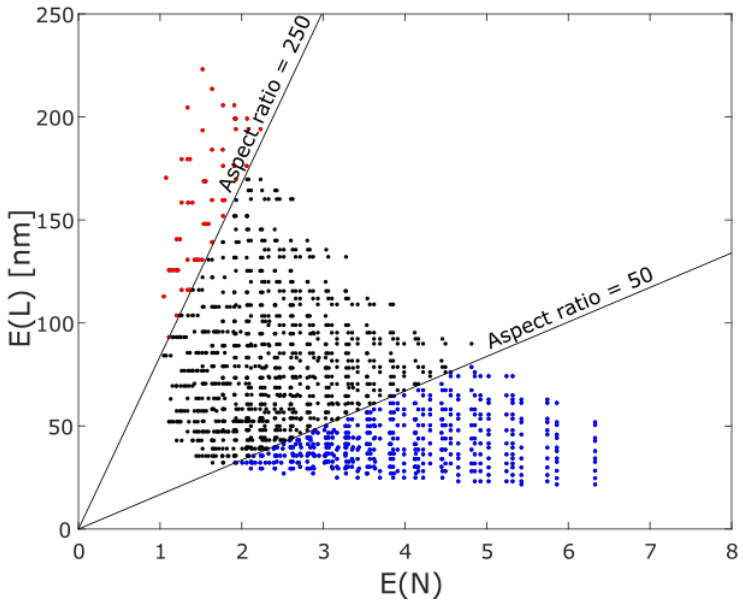

Figure 39: Expected dimensions of viable combinations of μ_L, μ_N, σ_L and σ_N with enhanced parameter range and resolution.

From Figure 39 we find the expected dimensions to be between 1 and 4 layers and 30 and 170 nm. This would mean that the particles in question are much smaller than those found in C. Backes et al., 2019 [19]. This result is in line with the low layer number estimation from the UV-Vis data.

The possible realisations can be displayed by plotting the resultant settling velocity distributions, as shown in Figure 40. The parameters of the settling velocity, μ_q and σ_q, can found by using Formula 27. Average values are plotted in black. The extreme cases with the strongest and weakest peak are colored blue and red, respectively. The blue line is an extreme case for the smallest particles, on average and the red line is the extreme case for the largest particles possible.

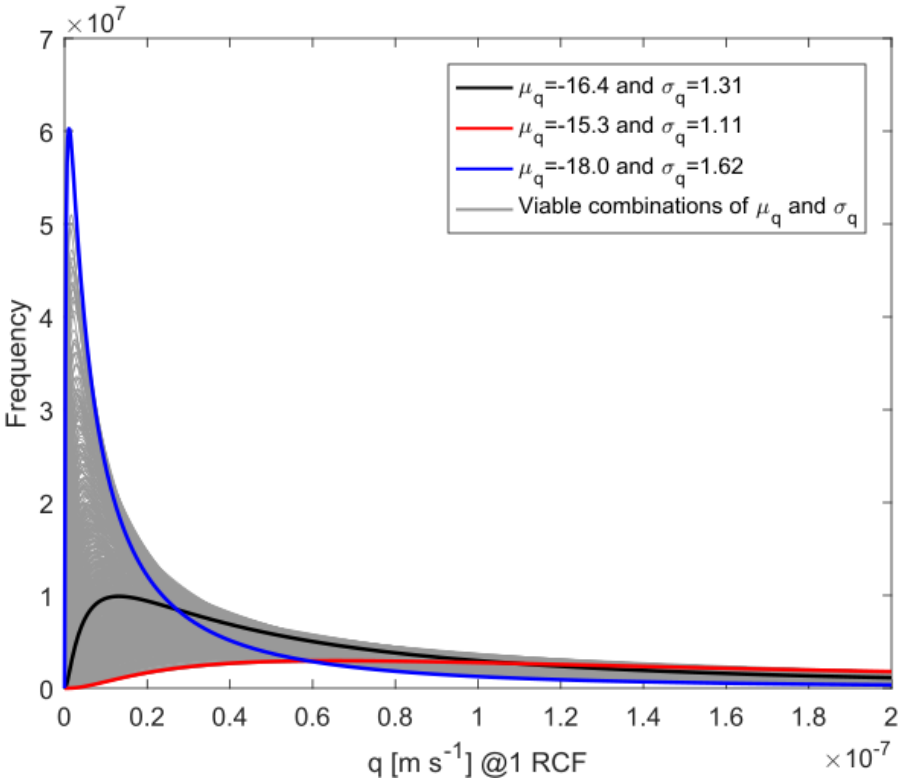

Figure 40: Resultant settling velocity distributions of viable combinations of μ_{L}, μ_{N}, σ_{L} and σ_{N}

.

5.9.1 Particle size distribution fitting including surfactant

Similar to the previous section, simulations for graphene with surfactant will be performed, called the cake model in Section 2.3. The surfactant will increase the settling velocity of the particles. For this reason, we expect the viable particles to be smaller. The same rough search, as for the simple case, is executed to find the following new set of parameters: $\mu_{\mathrm{L}} = [-18.4\ ;\ -16.4]$, $\mu_{\mathrm{N}} = [0\ ;\ 0.6]$, $\sigma_{\mathrm{L}} = [0.3\ ;\ 1.3]$ and $\sigma_{\mathrm{N}} = [0.3\ ;\ 1.3]$. The simulation was run with a resolution of 12 linear intervals per parameter, resulting in 20736 combinations. From the first filter, we find 330 combinations to be viable. The expected dimensions of the combinations of parameters are shown in Figure 41. As can be clearly seen, the expected values particles have significantly smaller lateral size, while the layer number remains roughly in the same range. For this reason, the expected aspect ratios are smaller, and no single combination has an aspect ratio greater than 113.

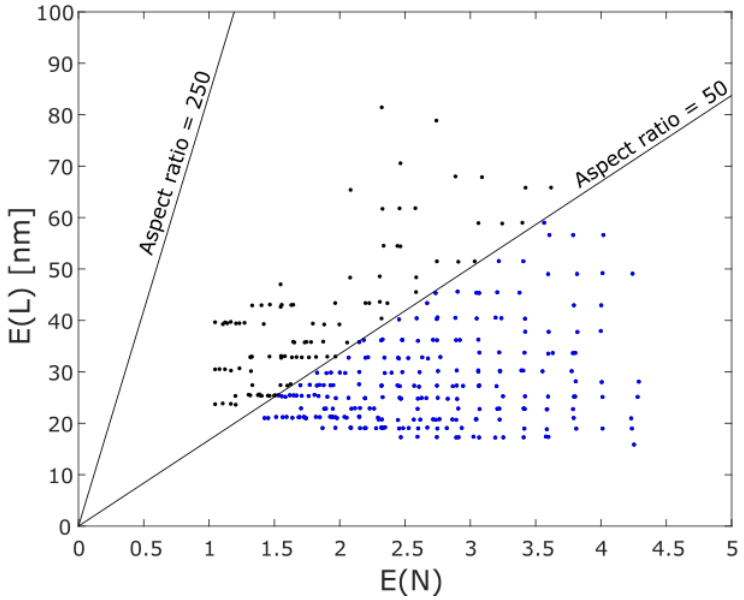

Figure 41: Expected dimensions of viable combinations of μ_L, μ_N, σ_L and σ_N assuming the cake-model.

5.9.2 Particle size distribution fitting including correlation

Besides the exploration of possible parameters ranges for μ_L, μ_N, σ_L and σ_N, a fifth variable will be incorporated into the following simulation: The correlation input constant ρ. As explained in Section 5.3.4, this input parameter ρ creates a correlation between the normally distributed values. When taking the exponent of these values, the actual correlation $\rho_{N,L}$ will be different from ρ. After the particles have been generated, the actual correlation $\rho_{N,L}$ is found. Based on the simple case, a set of parameter ranges will be explored. It is important to broaden the range for μ_L, since ρ affects $E(L)$. The parameter range was set to $\mu_L = [-20\ ;\ -15.8]$, $\mu_N = [0\ ;\ 0.6]$, $\sigma_L = [0.3\ ;\ 1.3]$, $\sigma_N = [0.3\ ;\ 1.3]$ and $\rho = [0\ ;\ 0.6]$, with 139755 combinations (15×11×11×11×7). After simulations, the same filters as for the previous cases were applied, in addition to separating the combinations based on their correlation $\rho_{N,L}$. The resultant average dimensions are plotted in Figure 42 for the different rates of correlation. The correlation input was set to the following intervals: $\rho = 0$, 0.1, 0.2 0.3, 0.4, 0,5, 0.6. However, the maximum was $\rho = 0.5$ for the viable combinations with $50 < AR < 250$, so we can confirm with certainty that that this parameter was set to the proper range.

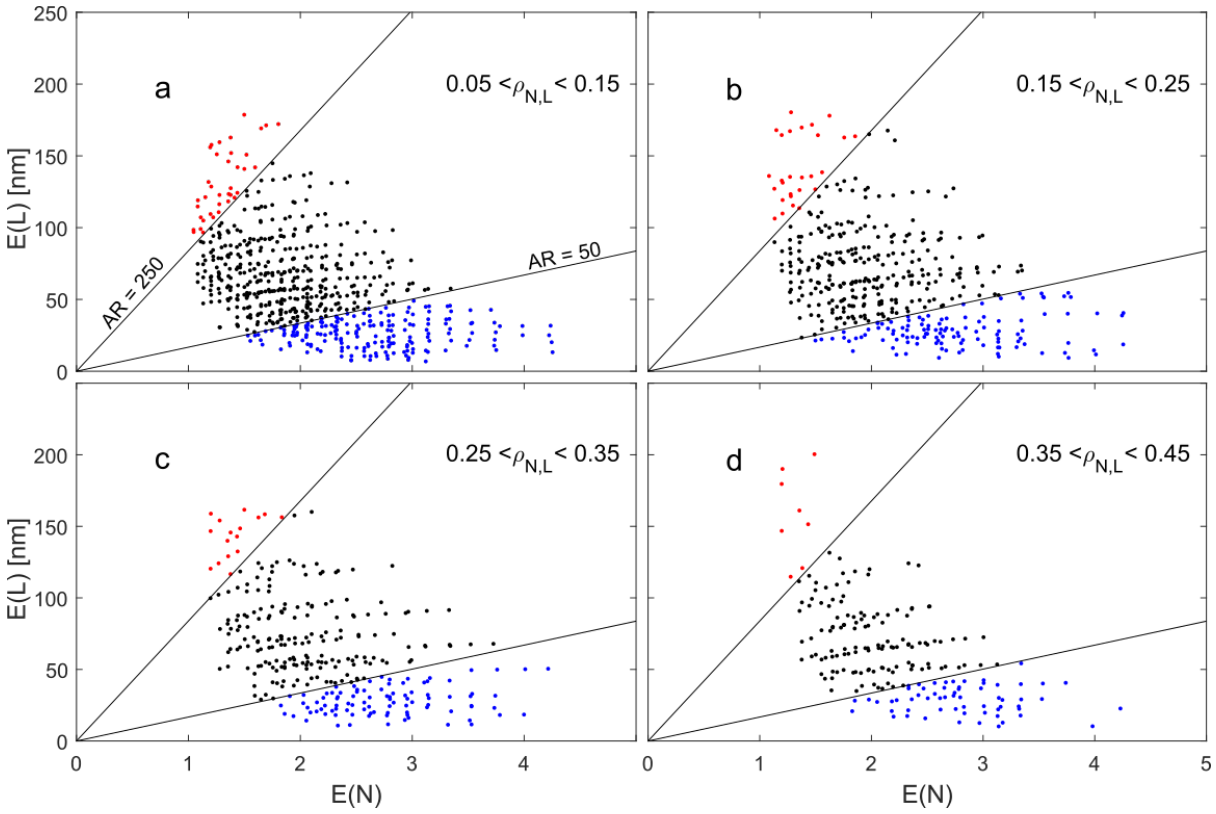

Figure 42: Expected dimensions of average realisations of μ_L, μ_N, σ_L and σ_N with correlation $\rho_{N,L}$. In (a), 397 combinations are viable with an AR between 50 and 250. For (b), there are 274 combinations, 186 for (c) and 128 for (d).

From Figure 42, we observe that the viable combinations with the smallest layer number change to larger layer numbers. From roughly 1 in (a) to 1.3 in (d). When we look at the average of all viable combinations, we also observe this trend, i.e. the average of the viable averages/expected values:

(a) $0.05 < \rho_{N,L} < 0.15$: $\langle E(N)\rangle$=1.86, $\langle E(L)\rangle$=67.3 nm
(b) $0.15 < \rho_{N,L} < 0.25$: $\langle E(N)\rangle$=1.97, $\langle E(L)\rangle$=72.1 nm
(c) $0.25 < \rho_{N,L} < 0.35$: $\langle E(N)\rangle$=2.04, $\langle E(L)\rangle$=74.0 nm
(d) $0.35 < \rho_{N,L} < 0.45$: $\langle E(N)\rangle$=2.00, $\langle E(L)\rangle$=72.1 nm

A maximum average of expected dimensions is observed at the correlation between $0.25 < \rho_{N,L} < 0.35$. The range of viable combinations does not change drastically, however, many more combinations are viable for lower correlations.

5.9.3 Particle size distribution fitting including slip

Similar simulations are performed to find viable combinations, where we include slip. However, this introduces a new challenge: The run time of the simulation. For the previous simulations, it took roughly 0.1 seconds to simulate one experiment with 200.000 particles. For the calculation of the settling velocity including slip, multiple interpolations have to be done per particle. A simulation including slip takes 324 seconds with 200.000

particles. In order to do a parameter range search with many combinations, the simulation has to be done with fewer particles, which will decrease the accuracy. Simulations with different amount of particles were executed to give an estimation of the standard deviation as a function of particle number, plotted in Figure 43.

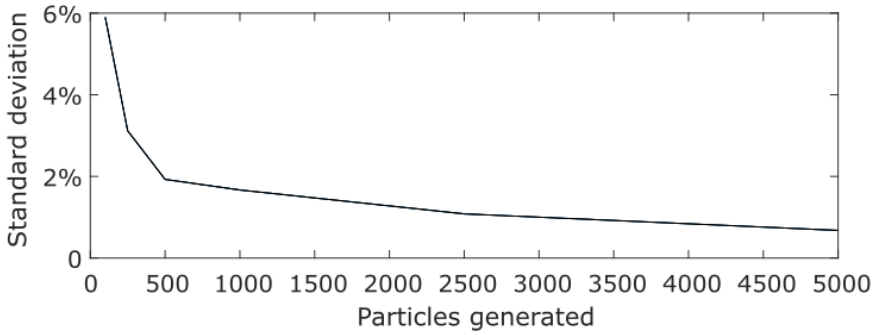

Figure 43: Standard deviation as a function of the number of particles generated with slip length.

Taking the standard deviation from Figure 43 into account, we set the number of particles to 500 and the extend the mass percentage interval from from the first filter 4 by 3%. This simulation will not result in parameter ranges that are as precise as the previous cases, but we accept that error. The parameter ranges were set to $\mu_{\mathrm{L}} = [-18 \ ; -15.5]$, $\mu_{\mathrm{N}} = [0 \ ; 1]$, $\sigma_{\mathrm{L}} = [0.3 \ ; 1.3]$, $\sigma_{\mathrm{N}} = [0.3 \ ; 1.3]$, with 10206 combinations. The results of the simulations are plotted in Figure 44.

We observe that the shape of the region with viable combinations is similar to that of the case with no slip, indicating that this less accurate search still yields viable results. However, considerably less combinations match the experimental data. As slip increases the settling velocity, we also expect the particles to decrease in size. This effect is also present in the simulations, mainly in the decrease in thickness. The average of the viable expected values is as follows:

(a) b = 10 nm: $\langle E(N)\rangle$=2.64, $\langle E(L)\rangle$=94.2
(b) b = 30 nm: $\langle E(N)\rangle$=2.70, $\langle E(L)\rangle$=91.2 nm
(c) b = 60 nm: $\langle E(N)\rangle$=2.36, $\langle E(L)\rangle$=89.8 nm
(d) b = 100 nm: $\langle E(N)\rangle$=2.01, $\langle E(L)\rangle$=85.6 nm

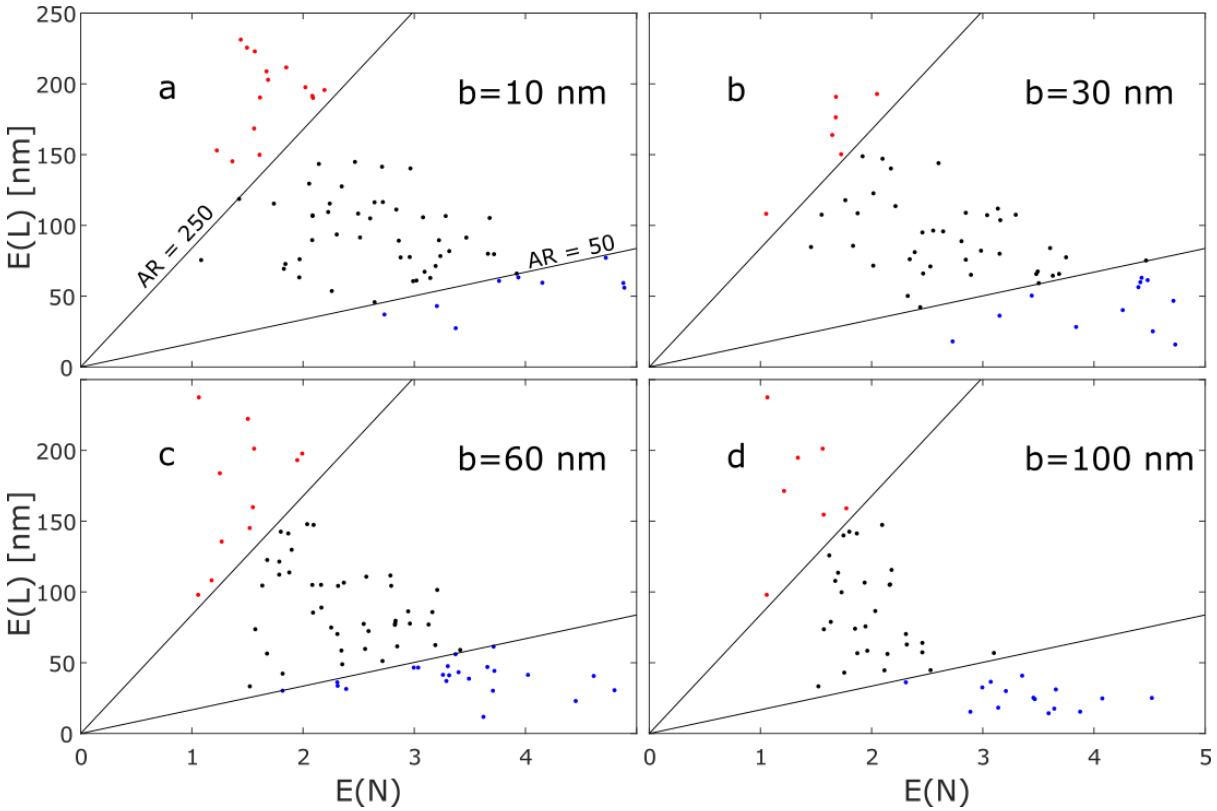

Figure 44: Viable combinations of μ_L, μ_N, σ_L and σ_N with a slip length ranging from 10 nm to 100 nm.

6. Conclusion and recommendations

6.1 Summary and conclusions

This thesis project led to several research outcomes, some purely experimental and some combining experiments with computer modelling. First of all, we were able to produce and characterise dispersions of graphene nanoparticles in liquids. This was a major achievement, as the research group had no prior experience in graphene production. The produced graphene dispersion, which was stabilized by surfactants, remained stably dispersed for at least 12 months. The size polydispersity of the dispersion was characterized by UV-Vis spectroscopy to find the mass concentration and average thickness of the particles. Centrifugation experiments in which we measured the concentration and thickness distribution over time by UV-Vis spectroscopy were performed to characterise the time-dependent deposition of the graphene particles from the supernatant region to the sedimented layer. Further characterization was done by steady-shear rheology experiments. Measurments of shear viscosity suggest that all our sedimentation experiements are conducted in the dilute limit in which the sedimentation rate can be estimated by using analytical formulas for the Stokes drag on plate-like particles.

To estimate the settling velocity of graphene particles in dilute dispersions a semi-analytical drag model that includes both the effect of hydrodynamic slip and the effect of surfactant molecules adhered to the particle surface was developed starting from the analytical solution for the Stokes drag on thin disks.

The key innovation of the current thesis is the develoment of a method to estimate the mean and variance of a log-normal size distribution of a graphene suspension by combining simple UV-Vis measurements with fast computer simulations. The idea is that recording the UV-Vis spectra at different times gives enough information to eliminate parameters of the size distribution that are unphysical, as they do not respect the Stokes settling formula (which we know to be valid for dilute suspensions). The estimate does not give exact parameters, but ranges of physical parameters, and can be improved if further experimental data is available.

The method rests on i) generating statistical populations of particles with a given variance and mean of a log-normal size distribution of length and thickness, and ii) predicting the fraction of this size distributions that would be present in the supernatant and in the sedimented layer at each time. The model incorporates also features that are known to be important for graphene dispersions, such as the effect of hydrodynamic slip (which can reduce the sedimentation rate) and the effect of surfactant molecules coating each particle (which can change the effective weight of each particle). While most of the work assume length and thickness to be statistically independent variables, in part of the work we also account for an experimentally plausible statistical correlation between thickness and lateral size, developing a method to produce log-normally distributed size

distributions with a given correlation coefficient.

The main advantage of the method we have developed, as opposed to techniques relying on Atomic Force Microscope and Transmission Electron Microscopy, are that it does not require extremely time consuming "manual counting" of the particles. The technique that was developed to estimate the particle size, only requires UV-vis characterization and a few hours of simulation, which makes it significantly more accessible than expensive microscopy techniques, for which extensive training is needed. The method therefore could be used for routine quality control of graphene or other 2D nanomaterials. More broadly, our research opens the opportunity for fast algorithmic estimation of particle size distributions from limited experimental data.

6.2 Recommendations for future research

6.2.1 Band centrifugation

From the theory and simulations we learn that higher purity can be achieved with BC compared to HC. Due to the time limit, the technique has not yet been developed. However, some methods were briefly explored. The top layer needs to be of a fluid of lower density than the bottom layer. If we want to perform BC with the dispersion we already have, graphene in water plus sodium cholate, we can either use a heavier material as bottom fluid or mix the dispersion with a lighter material, so that water can be used as bottom fluid. However, in both cases, the liquid must not interfere with the stability of the dispersion. One material that can surely be used is deuterium dioxide or D_2O as bottom fluid. It is nearly identical to regular water, except that there are extra neutrons in the nucleus, giving it a slightly higher density. However, it is too expensive to be used on a large scale. Low density solvents like isopropanol, ethanol and acetone were used to decrease the density of the dispersion, however, this caused immediate aggregation of graphene that was visible by eye. More research is needed to find materials that do not influence stability. Another option with large potential would be to design a new centrifuge that is able to inject the dispersion into the medium to perform BC mechanically. This way, the preparation of the band sample would be controlled.

6.2.2 Further estimation of initial distribution with AFM

We have found a variety of possible combinations of μ_L, μ_N, σ_L and σ_N. This gives a fair estimate of the content of our dispersion. However, the difference in possible average dimensions varies by a factor 4. When we have no equipment available to further characterize the dispersion, this is the maximum amount of information that can be extracted. However, when we have access to an AFM or TEM, the combinations can be narrowed even further. To obtain an accurate estimate, one would have to do a single centrifugation and investigate the supernatant with one of these microscopy techniques.

With TEM, the following variables can be found:

- Average lateral size: $\langle L \rangle$
- Variance in the lateral size: var(L)

With AFM, these same parameters that determine the lateral size can be found. Additionally, it provides information about the layer number and aspect ratio:

- Average layer number: $\langle N \rangle$
- Variance in the layer number: var(N)
- Average aspect ratio: $\langle E \rangle$

We simulate the same experiment for the already viable combinations. Then from these simulations we investigate the supernatant for each of the combinations and find the same parameters that are mentioned above. Comparison can be made between the simulation and microscopy data to find which of the combinations has the best similarity.

6.2.3 Application of known size distribution

Let us explore the theoretical case that an AFM measurement was performed that concluded the following set of parameters: $\mu_{\mathrm{L}} = -16.08$, $\mu_{\mathrm{N}} = 0.54$, $\sigma_{\mathrm{L}} = 0.38$ and $\sigma_{\mathrm{N}} = 1.15$, which results in $E(L)$=112 nm and $E(N)$=3.3, with an average aspect ratio of $\frac{112\mathrm{nm}}{3.3\times 0.335\mathrm{nm}} = 101$. When we simulate a large number of particles with these parameters, we can identify the portion of the SVD that contains the largest portion of the desired particles. We define the desired particles as bilayer or monolayer particles with lateral size $L > 100$ and plot these particles on a second SVD histogram with only particles that meet these requirements, as shown in Figure 45. From the histogram, one observes the bulk of these particles to have a settling velocity of $q < 1.5 \times 10^{-10}$ ms^{-1}. Desired particles make up 30.0% of the total number of particles. We can simulate centrifugation experiments to find the fraction that can be achieved by single- or multi-step HC or BC experiments. After performing a single BC experiment for 129.600 RCF$\times$hours, we increased the desired particle fraction from 30.0 to 45.2%.

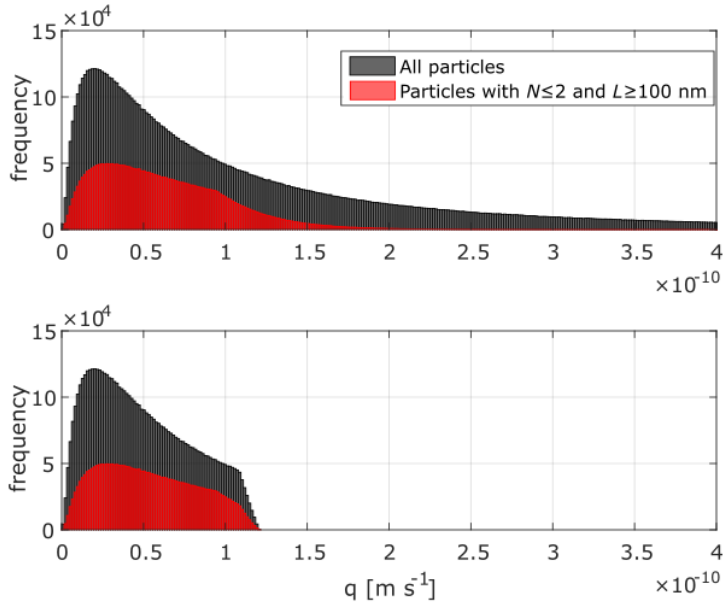

Figure 45: SVD histograms of simulation of 10.000.000 generated particles with $\mu_{\mathrm{L}} = -16.08$, $\mu_{\mathrm{N}} = 0.54$, $\sigma_{\mathrm{L}} = 0.38$ and $\sigma_{\mathrm{N}} = 1.15$. Frequency shown prior to (upper) and after (lower) a band centrifugation experiment at 129.600 RCF×hours.

6.2.4 Measurement of the slip length of graphene

In the literature, many molecular simulations about the slippage of graphene in water were performed. However, values for the slip lengths were inconsistent. An experimental setup, designed by Israelachvili [76] can be used to find the slip length. This has not been done for graphene and could be of great use to better understand interaction between graphene and a medium plus possible surfactant.

6.2.5 Molecular simulations

To better understand the sedimentation of graphene, molecular simulations could be performed. Different sizes of 2D graphene sheets under the influence of gravity will help us create a better understanding of the phenomena as slip, surfactant and hydration shells. Molecular simulations of graphene and various surfactants are found in the literature. None of these simulations are done with movement of graphene flakes. If we are accurately able to predict the velocity of a single flake, we can make accurate predictions of the sedimentation of many particles.

References

[1] Kostya S Novoselov, Andre K Geim, Sergei V Morozov, De-eng Jiang, Yanshui Zhang, Sergey V Dubonos, Irina V Grigorieva, and Alexandr A Firsov. Electric field effect in atomically thin carbon films. *science*, 306(5696):666–669, 2004.

[2] Jason Stafford, Andrius Patapas, Nwachukwu Uzo, Omar K Matar, and Camille Petit. Towards scale-up of graphene production via nonoxidizing liquid exfoliation methods. *AIChE Journal*, 64(9):3246–3276, 2018.

[3] Gints Kucinskis, Gunars Bajars, and Janis Kleperis. Graphene in lithium ion battery cathode materials: A review. *Journal of Power Sources*, 240:66–79, 2013.

[4] Sasha Stankovich, Dmitriy A Dikin, Geoffrey HB Dommett, Kevin M Kohlhaas, Eric J Zimney, Eric A Stach, Richard D Piner, SonBinh T Nguyen, and Rodney S Ruoff. Graphene-based composite materials. *nature*, 442(7100):282–286, 2006.

[5] Cancan Huang, Chun Li, and Gaoquan Shi. Graphene based catalysts. *Energy & Environmental Science*, 5(10):8848–8868, 2012.

[6] Andrea Capasso, AE Del Rio Castillo, H Sun, Alberto Ansaldo, Vittorio Pellegrini, and Francesco Bonaccorso. Ink-jet printing of graphene for flexible electronics: an environmentally-friendly approach. *Solid State Communications*, 224:53–63, 2015.

[7] Yenny Hernandez, Valeria Nicolosi, Mustafa Lotya, Fiona M Blighe, Zhenyu Sun, Sukanta De, IT McGovern, Brendan Holland, Michele Byrne, Yurii K Gun'Ko, et al. High-yield production of graphene by liquid-phase exfoliation of graphite. *Nature nanotechnology*, 3(9):563–568, 2008.

[8] Claudia Backes, Amr M Abdelkader, Concepción Alonso, Amandine Andrieux-Ledier, Raul Arenal, Jon Azpeitia, Nilanthy Balakrishnan, Luca Banszerus, Julien Barjon, Ruben Bartali, et al. Production and processing of graphene and related materials. *2D Materials*, 7(2):022001, 2020.

[9] Adrian T Murdock, Antal Koos, T Ben Britton, Lothar Houben, Tim Batten, Tong Zhang, Angus J Wilkinson, Rafal E Dunin-Borkowski, Christina E Lekka, and Nicole Grobert. Controlling the orientation, edge geometry, and thickness of chemical vapor deposition graphene. *ACS nano*, 7(2):1351–1359, 2013.

[10] Hye Jin Park, Jannik Meyer, Siegmar Roth, and Viera Skákalová. Growth and properties of few-layer graphene prepared by chemical vapor deposition. *Carbon*, 48(4):1088–1094, 2010.

[11] John Desmond Bernal. The structure of graphite. *Proceedings of the Royal Society of London. Series A, Containing Papers of a Mathematical and Physical Character*, 106(740):749–773, 1924.

[12] P Schmidt-Wellenburg, P Geltenbort, VV Nesvizhevsky, C Plonka, T Soldner, F Vezzu, and O Zimmer. A source of ultra-cold neutrons for the gravitational spectrometer granit. *arXiv preprint arXiv:0708.1373*, 2007.

[13] Claudia Backes, Keith R Paton, Damien Hanlon, Shengjun Yuan, Mikhail I Katsnelson, James Houston, Ronan J Smith, David McCloskey, John F Donegan, and Jonathan N Coleman. Spectroscopic metrics allow in situ measurement of mean size and thickness of liquid-exfoliated few-layer graphene nanosheets. *Nanoscale*, 8(7):4311–4323, 2016.

[14] Panagiotis G Karagiannidis, Stephen A Hodge, Lucia Lombardi, Flavia Tomarchio, Nicolas Decorde, Silvia Milana, Ilya Goykhman, Yang Su, Steven V Mesite, Duncan N Johnstone, et al. Microfluidization of graphite and formulation of graphene-based conductive inks. *ACS nano*, 11(3):2742–2755, 2017.

[15] Claudia Backes, Ronan J Smith, Niall McEvoy, Nina C Berner, David McCloskey, Hannah C Nerl, Arlene O'Neill, Paul J King, Tom Higgins, Damien Hanlon, et al. Edge and confinement effects allow in situ measurement of size and thickness of liquid-exfoliated nanosheets. *Nature communications*, 5(1):1–10, 2014.

[16] Lei Gong, Ian A Kinloch, Robert J Young, Ibtsam Riaz, Rashid Jalil, and Konstantin S Novoselov. Interfacial stress transfer in a graphene monolayer nanocomposite. *Advanced Materials*, 22(24):2694–2697, 2010.

[17] Pei He and Brian Derby. Controlling coffee ring formation during drying of inkjet printed 2d inks. *Advanced Materials Interfaces*, 4(22):1700944, 2017.

[18] Thomas F Jaramillo, Kristina P Jørgensen, Jacob Bonde, Jane H Nielsen, Sebastian Horch, and Ib Chorkendorff. Identification of active edge sites for electrochemical h2 evolution from mos2 nanocatalysts. *science*, 317(5834):100–102, 2007.

[19] Sean P Ogilvie, Matthew J Large, Marcus A O'Mara, Peter J Lynch, Cheuk Long Lee, Alice AK King, Claudia Backes, and Alan B Dalton. Size selection of liquid-exfoliated 2d nanosheets. *2D Materials*, 6(3):031002, 2019.

[20] Eswaraiah Varrla, Keith R Paton, Claudia Backes, Andrew Harvey, Ronan J Smith, Joe McCauley, and Jonathan N Coleman. Turbulence-assisted shear exfoliation of graphene using household detergent and a kitchen blender. *Nanoscale*, 6(20):11810–11819, 2014.

[21] Keith R Paton, Eswaraiah Varrla, Claudia Backes, Ronan J Smith, Umar Khan, Arlene O'Neill, Conor Boland, Mustafa Lotya, Oana M Istrate, Paul King, et al. Scalable production of large quantities of defect-free few-layer graphene by shear exfoliation in liquids. *Nature materials*, 13(6):624–630, 2014.

[22] Jason Stafford, Nwachukwu Uzo, Usmaan Farooq, Silvia Favero, Si Wang, Hsueh-Hung Chen, Anouk L'Hermitte, Camille Petit, and Omar K Matar. Real-time monitoring and hydrodynamic scaling of shear exfoliated graphene. *2D Materials*, 8(2):025029, 2021.

[23] Keith R Paton, James Anderson, Andrew J Pollard, and Toby Sainsbury. Production of few-layer graphene by microfluidization. *Materials Research Express*, 4(2):025604, 2017.

[24] Weifeng Zhao, Ming Fang, Furong Wu, Hang Wu, Liwei Wang, and Guohua Chen. Preparation of graphene by exfoliation of graphite using wet ball milling. *Journal of materials chemistry*, 20(28):5817–5819, 2010.

[25] Ahmad Amiri, Mohammad Naraghi, Goodarz Ahmadi, Mohammadreza Soleymaniha, and Mehdi Shanbedi. A review on liquid-phase exfoliation for scalable production of pure graphene, wrinkled, crumpled and functionalized graphene and challenges. *FlatChem*, 8:40–71, 2018.

[26] Yu Lin Zhong, Zhiming Tian, George P Simon, and Dan Li. Scalable production of graphene via wet chemistry: progress and challenges. *Materials Today*, 18(2):73–78, 2015.

[27] Jacob N Israelachvili. *Intermolecular and surface forces*. Academic press, 2015.

[28] Artur Ciesielski and Paolo Samori. Graphene via sonication assisted liquid-phase exfoliation. *Chemical Society Reviews*, 43(1):381–398, 2014.

[29] Charles M Hansen. *Hansen solubility parameters: a user's handbook*. CRC press, 2007.

[30] HM Solomon, BA Burgess, GL Kennedy, and RE Staples. 1-methyl-2-pyrrolidone (nmp): reproductive and developmental toxicity study by inhalation in the rat. *Drug and chemical toxicology*, 18(4):271–293, 1995.

[31] Gerald L Kennedy. Acute and subchronic toxicity of dimethylformam ide and dimethylacetamide following various routes of administration. *Drug and chemical toxicology*, 9(2):147–170, 1986.

[32] Udayabagya Halim, Chu Ran Zheng, Yu Chen, Zhaoyang Lin, Shan Jiang, Rui Cheng, Yu Huang, and Xiangfeng Duan. A rational design of cosolvent exfoliation

of layered materials by directly probing liquid–solid interaction. *Nature communications*, 4(1):1–7, 2013.

[33] Mustafa Lotya, Paul J King, Umar Khan, Sukanta De, and Jonathan N Coleman. High-concentration, surfactant-stabilized graphene dispersions. *ACS nano*, 4(6):3155–3162, 2010.

[34] Jonathan N Coleman, Mustafa Lotya, Arlene O'Neill, Shane D Bergin, Paul J King, Umar Khan, Karen Young, Alexandre Gaucher, Sukanta De, Ronan J Smith, et al. Two-dimensional nanosheets produced by liquid exfoliation of layered materials. *Science*, 331(6017):568–571, 2011.

[35] KP Lee, NC Chromey, R Culik, JR Barnes, and PW Schneider. Toxicity of n-methyl-2-pyrrolidone (nmp): teratogenic, subchronic, and two-year inhalation studies. *Fundamental and Applied Toxicology*, 9(2):222–235, 1987.

[36] Joohoon Kang, Jung-Woo T Seo, Diego Alducin, Arturo Ponce, Miguel Jose Yacaman, and Mark C Hersam. Thickness sorting of two-dimensional transition metal dichalcogenides via copolymer-assisted density gradient ultracentrifugation. *Nature communications*, 5(1):1–7, 2014.

[37] Jian Zhu, Joohoon Kang, Junmo Kang, Deep Jariwala, Joshua D Wood, Jung-Woo T Seo, Kan-Sheng Chen, Tobin J Marks, and Mark C Hersam. Solution-processed dielectrics based on thickness-sorted two-dimensional hexagonal boron nitride nanosheets. *Nano letters*, 15(10):7029–7036, 2015.

[38] Alexander A Green and Mark C Hersam. Solution phase production of graphene with controlled thickness via density differentiation. *Nano letters*, 9(12):4031–4036, 2009.

[39] Shangchao Lin, Chih-Jen Shih, Michael S Strano, and Daniel Blankschtein. Molecular insights into the surface morphology, layering structure, and aggregation kinetics of surfactant-stabilized graphene dispersions. *Journal of the American Chemical Society*, 133(32):12810–12823, 2011.

[40] Chih-Jen Shih, Shangchao Lin, Michael S Strano, and Daniel Blankschtein. Understanding the stabilization of single-walled carbon nanotubes and graphene in ionic surfactant aqueous solutions: large-scale coarse-grained molecular dynamics simulation-assisted dlvo theory. *The Journal of Physical Chemistry C*, 119(2):1047–1060, 2015.

[41] Haoyue Sun and Xiaoning Yang. Molecular simulation of self-assembly structure and interfacial interaction for sdbs adsorption on graphene. *Colloids and Surfaces A: Physicochemical and Engineering Aspects*, 462:82–89, 2014.

[42] SK Hait, PR Majhi, A Blume, and SP Moulik. A critical assessment of micellization of sodium dodecyl benzene sulfonate (sdbs) and its interaction with poly (vinyl pyrrolidone) and hydrophobically modified polymers, jr 400 and lm 200. *The Journal of Physical Chemistry B*, 107(15):3650–3658, 2003.

[43] Francesco Bonaccorso and Zhipei Sun. Solution processing of graphene, topological insulators and other 2d crystals for ultrafast photonics. *Optical Materials Express*, 4(1):63–78, 2014.

[44] Dalal Fadil, Ridwan F Hossain, Gustavo A Saenz, and Anupama B Kaul. On the chemically-assisted excitonic enhancement in environmentally-friendly solution dispersions of two-dimensional mos2 and ws2. *Journal of Materials Chemistry C*, 5(22):5323–5333, 2017.

[45] Arlene O'Neill, Umar Khan, and Jonathan N Coleman. Preparation of high concentration dispersions of exfoliated mos2 with increased flake size. *Chemistry of Materials*, 24(12):2414–2421, 2012.

[46] Heng Li, Lucas Beetsma, Suriya Senthil Kumar, and Lorenzo Botto. Theoretical analysis of a multi-step method to fractionate dilute poly-dispersed particle systems in sedimentation or centrifugation (to be submitted).

[47] AE Boycott. Sedimentation of blood corpuscles. *Nature*, 104(2621):532–532, 1920.

[48] Koreo Kinosita. Sedimentation in tilted vessels (1). *Journal of Colloid Science*, 4(5):525–536, 1949.

[49] Andreas Acrivos and Eric Herbolzheimer. Enhanced sedimentation in settling tanks with inclined walls. *Journal of fluid mechanics*, 92(3):435–457, 1979.

[50] Damien Hanlon, Claudia Backes, Evie Doherty, Clotilde S Cucinotta, Nina C Berner, Conor Boland, Kangho Lee, Andrew Harvey, Peter Lynch, Zahra Gholamvand, et al. Liquid exfoliation of solvent-stabilized few-layer black phosphorus for applications beyond electronics. *Nature communications*, 6(1):1–11, 2015.

[51] Ute Kaiser, Johannes Biskupek, Jannik C Meyer, Jens Leschner, Lorenz Lechner, Harald Rose, Michael Stöger-Pollach, Andrei N Khlobystov, Peter Hartel, Heiko Mueller, et al. Transmission electron microscopy at 20 kv for imaging and spectroscopy. *Ultramicroscopy*, 111(8):1239–1246, 2011.

[52] Daniel Rugar and Paul Hansma. Atomic force microscopy. *Physics today*, 43(10):23–30, 1990.

[53] Jason Stafford, Nwachukwu Uzo, Usmaan Farooq, Silvia Favero, Si Wang, Hseuh-Hung Chen, Anouk L'Hermitte, Camille Petit, and Omar Matar. Universal scaling and real-time monitoring of the production of liquid exfoliated graphene. 2020.

[54] Umar Khan, Arlene O'Neill, Mustafa Lotya, Sukanta De, and Jonathan N Coleman. High-concentration solvent exfoliation of graphene. *small*, 6(7):864–871, 2010.

[55] Mustafa Lotya, Yenny Hernandez, Paul J King, Ronan J Smith, Valeria Nicolosi, Lisa S Karlsson, Fiona M Blighe, Sukanta De, Zhiming Wang, IT McGovern, et al. Liquid phase production of graphene by exfoliation of graphite in surfactant/water solutions. *Journal of the American Chemical Society*, 131(10):3611–3620, 2009.

[56] Rahul Raveendran Nair, Peter Blake, Alexander N Grigorenko, Konstantin S Novoselov, Tim J Booth, Tobias Stauber, Nuno MR Peres, and Andre K Geim. Fine structure constant defines visual transparency of graphene. *Science*, 320(5881):1308–1308, 2008.

[57] LM Malard, Marcos Assunção Pimenta, Gene Dresselhaus, and MS Dresselhaus. Raman spectroscopy in graphene. *Physics reports*, 473(5-6):51–87, 2009.

[58] George Gabriel Stokes et al. On the effect of the internal friction of fluids on the motion of pendulums. 1851.

[59] E Loth. Drag of non-spherical solid particles of regular and irregular shape. *Powder Technology*, 182(3):342–353, 2008.

[60] Onofrio M Maragó, Francesco Bonaccorso, Rosalba Saija, Giulia Privitera, Pietro G Gucciardi, Maria Antonia Iatì, Giuseppe Calogero, Philip H Jones, Ferdinando Borghese, Paolo Denti, et al. Brownian motion of graphene. *ACS nano*, 4(12):7515–7523, 2010.

[61] Peng He, Andres F Mejia, Zhengdong Cheng, Dazhi Sun, Hung-Jue Sue, Dean S Dinair, and Manuel Marquez. Hindrance function for sedimentation and creaming of colloidal disks. *Physical Review E*, 81(2):026310, 2010.

[62] E Kuusela, JM Lahtinen, and T Ala-Nissila. Collective effects in settling of spheroids under steady-state sedimentation. *Physical review letters*, 90(9):094502, 2003.

[63] Sebastian Barwich, Jonathan N Coleman, and Matthias E Möbius. Yielding and flow of highly concentrated, few-layer graphene suspensions. *Soft Matter*, 11(16):3159–3164, 2015.

[64] Gabriele Tocci, Laurent Joly, and Angelos Michaelides. Friction of water on graphene and hexagonal boron nitride from ab initio methods: very different slippage despite very similar interface structures. *Nano letters*, 14(12):6872–6877, 2014.

[65] Catherine Kamal, Simon Gravelle, and Lorenzo Botto. Hydrodynamic slip can align thin nanoplatelets in shear flow. *Nature communications*, 11(1):1–10, 2020.

[66] Sridhar Kumar Kannam, BD Todd, Jesper Schmidt Hansen, and Peter J Daivis. How fast does water flow in carbon nanotubes? *The Journal of chemical physics*, 138(9):094701, 2013.

[67] Christophe Cheikh and Ger Koper. Friction in surfactant layers at solid–liquid interfaces. *Colloids and Surfaces A: Physicochemical and Engineering Aspects*, 270:252–256, 2005.

[68] CL Henry, C Neto, DR Evans, S Biggs, and VSJ Craig. The effect of surfactant adsorption on liquid boundary slippage. *Physica A: Statistical Mechanics and its Applications*, 339(1-2):60–65, 2004.

[69] Christian Kunert and Jens Harting. On the effect of surfactant adsorption and viscosity change on apparent slip in hydrophobic microchannels. *Progress in Computational Fluid Dynamics, an International Journal*, 8(1-4):197–205, 2008.

[70] HJ Keh and YC Chang. Slow motion of a slip spheroid along its axis of revolution. *International journal of multiphase flow*, 34(8):713–722, 2008.

[71] Yu C Chang and Huan J Keh. Theoretical study of the creeping motion of axially and fore-and-aft symmetric slip particles in an arbitrary direction. *European Journal of Mechanics-B/Fluids*, 30(2):236–244, 2011.

[72] JD Sherwood. Resistance coefficients for stokes flow around a disk with a navier slip condition. *Physics of Fluids*, 24(9):093103, 2012.

[73] David T Snow. The frequency and apertures of fractures in rock. In *International journal of Rock mechanics and Mining sciences & Geomechanics Abstracts*, volume 7, pages 23–40. Elsevier, 1970.

[74] WI Higuchi and EN Hiestand. Dissolution rates of finely divided drug powders i. effect of a distribution of particle sizes in a diffusion-controlled process. *Journal of pharmaceutical sciences*, 52(1):67–71, 1963.

[75] Don S Lemons. An introduction to stochastic processes in physics, 2003.

[76] Jacob N Israelachvili. Measurement of the viscosity of liquids in very thin films. *Journal of colloid and interface science*, 110(1):263–271, 1986.

A. Derivation of the settling velocity

The derivation for the settling velocity starts with the following formulas for the drag, equivalent volume diameter, volume, correction factor and centrifugal force resp.

$$F_{\mathrm{D}} = \langle f \rangle \cdot 3\pi d_{\mathrm{eq}} \mu q$$

$$d_{\mathrm{eq}} = (\frac{6V}{\pi})^{\frac{1}{3}}$$

$$V = \frac{\pi}{4} L^2 t$$

$$\langle f \rangle = \frac{2}{\pi} E^{-\frac{1}{3}}$$

$$F_{\mathrm{C}} = \Delta\rho \frac{\pi}{4} L^2 t g_{\mathrm{e}}$$

The drag becomes

$$F_{\mathrm{D}} = \frac{2}{\pi} t^{-\frac{1}{3}} L^{\frac{1}{3}} \cdot 3\pi (\frac{6}{\pi} V)^{\frac{1}{3}} \mu q =$$
$$\frac{2}{\pi} t^{-\frac{1}{3}} L^{\frac{1}{3}} \cdot 3\pi (\frac{6}{\pi} \frac{\pi}{4} L^2 t)^{\frac{1}{3}} \mu q =$$
$$\frac{2}{\pi} t^{-\frac{1}{3}} L^{\frac{1}{3}} 3\pi (\frac{3}{2})^{\frac{1}{3}} L^{\frac{2}{3}} t^{\frac{1}{3}} \mu q =$$
$$6L(\frac{3}{2})^{\frac{1}{3}} \mu q =$$
$$(324)^{\frac{1}{3}} L \mu q$$

Equating this to the centrifugal force:

$$F_{\mathrm{C}} = \Delta\rho \frac{\pi}{4} L^2 t g_{\mathrm{e}} = (324)^{\frac{1}{3}} L \pi \mu q$$

$$q = \frac{\Delta\rho \pi L^2 t g_{\mathrm{e}}}{4(324)^{\frac{1}{3}} L \mu}$$

$$q = \frac{\Delta\rho \pi L t g_{\mathrm{e}}}{(20736)^{\frac{1}{3}} \mu}$$

B. Calculation of the hindered settling velocity

To estimate the hindered settling velocity, we assume an aspect ratio of E=1/50 or ξ=50 and a volume fraction of ϕ=0.01. The hindered settling velocity is then:

$$\frac{q}{q_0} = (1 - W)(1 - \phi)^{K_S} + W\left[1 - (\phi + \phi_m)\right]^{K_{\text{sphere}}} \tag{45}$$

The physical meaning of the variables will be left out of this calculation, but may be found in the article from He et al., 2010 [61].

$$W = \left[1 + \exp\left(-\frac{\phi - \phi_t}{\kappa}\right)\right]^{-1}$$

$$\phi_t = 0.062 - 0.0123(\xi - 1) + 7.4571 \times 10^{-4}(\xi - 1)^2$$

$$\phi_m = (0.284 \pm 0.021)[1 - \exp\left(\frac{1 - \xi}{2.29 \pm 0.487}\right)]$$

$$K_S = (5.95 \pm 0.27) + (7.614 \pm 0.255)(\xi - 1)$$

$$K_{\text{sphere}} = 5.95 \pm 0.27$$

$$\kappa = 0.008$$

C. Slip model script

The MATLAB code for the slip length model is shown below. The input is individual particle data where L_i, N_i corresponds to the lateral size and number of layers of particle i. The slip length is set to a constant: 20 nm. However, this can be adjusted accordingly.

```
L= [10 11 12 13 14 15 17 18 20 30 40 50 60 70 75 80 90 100
   150 200 300 400 500 750 1000 1500 ];
N=15*ones(1,length(L));
b=20*ones(1,length(N));

t=zeros(1,length(N));
E=zeros(1,length(N));
b_L=zeros(1,length(N));

for i=1:length(N)
    t(i)=(N(i)+1)*0.335;
    E(i)=t(i)/L(i);
    b_L(i)=b(i)/L(i);
end

f_sher_para=8/(3*pi);

E_para=     [0.9    0.5    0.2    0.1    0.05];

f_chan_para=[0.9801 0.9053 0.8615 0.8525 f_sher_para   % b/L
   =0, no slip
             0.9052 0.8448 0.8316 0.8396 f_sher_para   % b/L
                =0.1
             0.7496 0.7696 0.8157 0.8355 f_sher_para   % b/L
                =1
             0.6804 0.7470 0.8122 0.8347 f_sher_para]; % b/L=
                inf, free slip
b_L_val=[0 0.1 1 10];

f_para=zeros(1,length(N));
for i=1:length(N)
    if E(i)<=0.05
        f_para(i)=f_sher_para;
    elseif E(i)>0.05
```

```
30          f_c_p=zeros(1,4);
31          f_c_p(1)=interp1(E_para,f_chan_para(1,:),E(i));
32          f_c_p(2)=interp1(E_para,f_chan_para(2,:),E(i));
33          f_c_p(3)=interp1(E_para,f_chan_para(3,:),E(i));
34          f_c_p(4)=interp1(E_para,f_chan_para(4,:),E(i));
35
36          f_para(i)=interp1(b_L_val,f_c_p,b_L(i));
37      end
38  end
39
40  f_chan_perp1=[0.9597 0.7927 0.7049 0.6596 0.569
                    % b/L=0, no slip
41              0.8828 0.7156 0.6284 0.5839 0.466169215373116 %
                   b/L=0.1
42              0.7097 0.5416 0.4535 0.4084 0.198154317 % b/L=1
43              0.6263 0.4572 0.3680 0.3223 1/15];  % b/L=inf
44
45  b_L_val_perp=[0 0.1 1 1.2 1.4 1.6 1.8 2 2.2 2.4 2.6 2.8 3 3.2
        3.4 3.6 3.8 4 4.2 4.4 4.6 4.8 5 10];
46
47  f_perp=zeros(1,length(N));
48  for i=1:length(N)
49
50  E_perp=[0.9     0.5     0.3     0.2     0];
51
52  if b_L(i)>=5
53  f_chan_perp=[0.9597     0.7927     0.7049     0.6596     0.569
54      0.8828     0.7156     0.6284     0.5839     0.466169215373116
55      0.7097     0.5416     0.4535     0.4084     0.198154317
56      0.6895     0.5212     0.4330     0.3878     0.1672
57      0.6742     0.5058     0.4174     0.3722     0.1436
58      0.6626     0.4941     0.4056     0.3602     0.1255
59      0.6538     0.4852     0.3965     0.3512     0.1117
60      0.6472     0.4784     0.3897     0.3443     0.1011
61      0.6421     0.4733     0.3845     0.3390     0.0930
62      0.6383     0.4694     0.3805     0.3350     0.0868
63      0.6354     0.4665     0.3775     0.3320     0.0821
64      0.6332     0.4642     0.3752     0.3297     0.0784
65      0.6315     0.4625     0.3735     0.3279     0.0757
66      0.6303     0.4613     0.3722     0.3266     0.0736
```

```
    0.6293    0.4603    0.3712    0.3255    0.0719
    0.6286    0.4595    0.3704    0.3248    0.0707
    0.6280    0.4590    0.3698    0.3242    0.0697
    0.6276    0.4585    0.3694    0.3237    0.0690
    0.6273    0.4582    0.3691    0.3234    0.0685
    0.6270    0.4580    0.3688    0.3231    0.0680
    0.6269    0.4578    0.3686    0.3229    0.0677
    0.6267    0.4576    0.3685    0.3228    0.0675
    0.6266    0.4575    0.3684    0.3227    0.0673
              0.6263 0.4572 0.3680 0.3223 L(i)/(3*b(i))];
elseif b_L(i)<5
f_chan_perp=[0.9597 0.7927 0.7049 0.6596 0.569
    0.8828    0.7156    0.6284    0.5839    0.466169215373116
    0.7097    0.5416    0.4535    0.4084    0.198154317
    0.6895    0.5212    0.4330    0.3878    0.1672
    0.6742    0.5058    0.4174    0.3722    0.1436
    0.6626    0.4941    0.4056    0.3602    0.1255
    0.6538    0.4852    0.3965    0.3512    0.1117
    0.6472    0.4784    0.3897    0.3443    0.1011
    0.6421    0.4733    0.3845    0.3390    0.0930
    0.6383    0.4694    0.3805    0.3350    0.0868
    0.6354    0.4665    0.3775    0.3320    0.0821
    0.6332    0.4642    0.3752    0.3297    0.0784
    0.6315    0.4625    0.3735    0.3279    0.0757
    0.6303    0.4613    0.3722    0.3266    0.0736
    0.6293    0.4603    0.3712    0.3255    0.0719
    0.6286    0.4595    0.3704    0.3248    0.0707
    0.6280    0.4590    0.3698    0.3242    0.0697
    0.6276    0.4585    0.3694    0.3237    0.0690
    0.6273    0.4582    0.3691    0.3234    0.0685
    0.6270    0.4580    0.3688    0.3231    0.0680
    0.6269    0.4578    0.3686    0.3229    0.0677
    0.6267    0.4576    0.3685    0.3228    0.0675
    0.6266    0.4575    0.3684    0.3227    0.0673
              0.6263 0.4572 0.3680 0.3223 1/15];
end

        f_s_p=zeros(1,24);
    for j=1:24
        f_s_p(1,j)=interp1(E_perp,f_chan_perp(j,:),E(i));
```

```
107     end
108
109     f_perp(i)=interp1(b_L_val_perp,f_s_p,b_L(i));
110 end
```

D. Size estimation simulations

The following section provides instructions to the use of the size estimation method. There are only instructions to simulate for the simple calculation of q. For instructions to include slip, surfactant and correlation, contact me on lucasbeetsma@hotail.nl.

To simulate centrifugation experiments, the following scripts are needed:

- mu_sigma_N_and_L_space_2.m
- mass_frac_2.m
- q_slip.m

Be sure to save the three files in one folder. Also, be sure that the latter two files are saved as mass_frac_2.m and q_slip.m, sicne these functions are called from the main body, u_sigma_N_and_L_space_2.m.

Then, how do we actually use the script? When we look at the main body, we see

```
n_mu_L =14;
n_mu_N =9;
n_sigma_L =9;
n_sigma_N =9;
```

This is the number of linear intervals of the parameters μ_{L}, μ_{N}, σ_{L}, σ_{N}. Logically, the amount of combinations that is simulated is the multiple of these values. The amount of intervals can be changed accordingly. Change n=200000 in mass_frac_2.m to the desired number of particles to simulate.

Below is the ranges of the parameters and RCF and time:

```
mu_L_minmax =[ -15.5 -19.5];
mu_N_minmax =[0 1];
sigma_L_minmax =[0.3 1.3];
sigma_N_minmax =[0.3 1.3];
Rcf =2164;

time =3600*[1 2 5 14];
```

Currently the script will run four simulations per combination, where 1, 2, 5 and 14 hours at 2164 RCF are simulated.

The script will return the matrix MB, where every row is:

1	2	3	4	5	6	7	8	9	10	11	12
μ_{L}	μ_{N}	σ_{L}	σ_{N}	ρ	$\frac{m_{1\mathrm{hr}}}{m_0}$	$\frac{m_{2\mathrm{hr}}}{m_0}$	$\frac{m_{5\mathrm{hr}}}{m_0}$	$\frac{m_{14\mathrm{hr}}}{m_0}$	$\langle N \rangle$	$\langle L \rangle$	$\rho_{\mathrm{N,L}}$

To compare to the experimental data, we look at the following in the main body:

```
FILTER = MB ( all ( MB (: ,6) > 0.753 & MB (: ,6) < 0.92 & MB
    (: ,7) >
0.663 & MB (: ,7) < 0.84 & MB (: ,8) > 0.488 & MB (: ,8) <
   0.62
& MB (: ,9) > 0.24 & MB (: ,9) < 0.37 ,2) ,:) ;
```

Change the values for

```
MB (: ,6) > 0.753 & MB (: ,6) < 0.92 to
```

to the values obtained from experimental data for 1 hour of centrifugation. And

```
MB (: ,7) > 0.663 & MB (: ,7)
```

to those of 2 hours, and so on. The FILTER matrix will return the reduced matrix of MB, only with the combinations that pass the filter.

Note: A much more user-friendly script is under development. Contact me on the email adress above for the latest version.

D.1 Main body (mu_sigma_N_and_L_space_2.m)

```
close all
clear all

n_mu_L=4;
n_mu_N=4;
n_sigma_L=4;
n_sigma_N=4;
n_rho=1;

Rcf=2164;

time=3600*[1 2 5 14];

mu_L_minmax    =[-15.5 -16.5];
mu_N_minmax    =[0       1];
sigma_L_minmax=[0.3   1.3];
sigma_N_minmax=[0.3   1.3];
rho_minmax     =[0     0];

mu_L_M   =linspace(mu_L_minmax(1),mu_L_minmax(2),n_mu_L);
mu_N_M   =linspace(mu_N_minmax(1),mu_N_minmax(2),n_mu_N);
sigma_L_M=linspace(sigma_L_minmax(1),sigma_L_minmax(2),
   n_sigma_L);
sigma_N_M=linspace(sigma_N_minmax(1),sigma_L_minmax(2),
   n_sigma_N);
rho_M    =linspace(rho_minmax(1),rho_minmax(2),n_rho);

M=zeros(n_mu_L*n_mu_N*n_sigma_L*n_sigma_N*n_rho,5);
for j1                =1:n_mu_L
    for j2            =1:n_mu_N
        for j3        =1:n_sigma_L
            for j4    =1:n_sigma_N
                for j5=1:n_rho
                M((n_mu_N*n_sigma_L*n_sigma_N*n_rho*(j1-1)+
                   n_sigma_L*n_sigma_N*n_rho*(j2-1)+n_sigma_N
                   *n_rho*(j3-1)+n_rho*(j4-1)+j5),:)=[mu_L_M(
                   j1)
```

```
33                                                                  mu_N_M
                                                                       (
                                                                       j2
                                                                       )
34                                                                  sigma_L_M
                                                                       (
                                                                       j3
                                                                       )
35                                                                  sigma_N_M
                                                                       (
                                                                       j4
                                                                       )
36                                                                  rho_M
                                                                       (
                                                                       j5
                                                                       )
                                                                       ]';

37                      end
38                  end
39              end
40          end
41  end
42
43
44
45  B    =zeros(length(M(:,1)),(length(time)+2));
46  for i=1:length(M(:,1))
47      for j=1:length(time)
48      [B(i,j),B(i,(length(time)+1)),B(i,(length(time)+2)),B(i,(
           length(time)+3))]=mass_frac_2(M(i,1),M(i,2),M(i,3),M(i
           ,4),time(j),Rcf,0,M(i,5));
49      end
50  end
51
52  MB=[M B];
53
54  FILTER= MB(all(MB(:,6) > 0.753 & MB(:,6) < 0.92 & MB(:,7) >
       0.663 & MB(:,7) < 0.84 & MB(:,8) > 0.488 & MB(:,8) < 0.62
       & MB(:,9) > 0.24 & MB(:,9) < 0.37,2),:);
```

D.2 Simulation function (mass_frac_2.m)

```
function [MASS_FRAC,AVG_N,AVG_L,Correlation] = mass_frac_2(
   mu_L,mu_N,sigma_L,sigma_N,time,RCF,surfactant,rho)

n=200000;
P=zeros(7,n);
b=60E-9; % slip
H=0.05;

R=[1 rho;rho 1];

Lchol = chol(R);

M(:,1)=mu_N+sigma_N*randn([n,1]);
M(:,2)=mu_L+sigma_L*randn([n,1]);

M_corr=(M*Lchol)';

%LAYER NUMBER
P(1,:)=exp(M_corr(1,:));
%P(1,:)=Parameter*lognrnd(0,1,[n,1]);

%LATERAL SIZE
P(2,:)=exp(M_corr(2,:));
%P(2,:)=Parameter*F*lognrnd(0,1,[n,1]);


AVG_N=sum(P(1,:))/n;
AVG_L=1E9*sum(P(2,:))/n;
EXP_L=exp(mu_L+sigma_L^2/2)*1E9;
EXP_N=exp(mu_N+sigma_N^2/2);

%Without enhanced settling velocity due to surfactant
if surfactant == 0
%SETTLING VELOCITY
for i=1:n
    P(3,i)=((pi*1260*9.81)/(27.48*0.001))*P(1,i)*P(2,i)*0.335
       E-9;
end
```

```
37
38 %MASS PER PARTICLE
39 for i=1:n
40     P(4,i)=(pi/4)*P(1,i)*P(2,i)^2*0.335E-9*2260;
41 end
42
43 %With enhanced sett. vel. due to surfactant
44 elseif surfactant ==1
45
46 %SETTLING VELOCITY
47 rho_SC=7.66E-7;
48 m_SC=7.15E-25;
49 sigma=1.35E18;
50 rho_H=1000;
51 t_H=3.3E-9;
52 t_A=0.355E-9;
53 t_gra=0.335E-9;
54 for i=1:n
55     P(3,i)=((pi*9.81)/(27.48*0.001))*P(2,i)*(rho_SC*P(1,i)+2*
          m_SC*sigma-rho_H*((P(1,i)+1)*t_gra+2*t_A));
56 end
57
58
59
60 %MASS PER PARTICLE
61 for i=1:n
62     P(4,i)=(pi/4)*P(1,i)*P(2,i)^2*0.335E-9*2260;
63 end
64
65 %When enhanced sett. vel. due to slip
66 elseif surfactant ==2
67 for i=1:n
68     P(3,i)=q_slip(P(1,i),P(2,i),b);
69 end
70
71 %MASS PER PARTICLE
72 for i=1:n
73     P(4,i)=(pi/4)*P(1,i)*P(2,i)^2*0.335E-9*2260;
74 end
75
```

```
76
77 end
78
79 %POSITION IN VIAL
80 P(5,:)=H*rand([n,1]);
81
82 Total_mass=sum(P(4,:));
83 Average_mass_p_particle=Total_mass/n;
84
85 SD_HC=zeros(2,n);
86 SN_HC=zeros(2,n);
87
88 for i=1:n
89     if P(3,i) > P(5,i)/(time*RCF)
90         SD_HC(1,i)=P(3,i);
91         SD_HC(2,i)=P(4,i);
92         SN_HC(1,i)=NaN;
93         SN_HC(2,i)=0;
94     else
95         SD_HC(1,i)=NaN;
96         SD_HC(2,i)=0;
97         SN_HC(1,i)=P(3,i);
98         SN_HC(2,i)=P(4,i);
99     end
100 end
101
102 [MASS_FRAC]=sum(SN_HC(2,:))/(sum(SD_HC(2,:))+sum(SN_HC(2,:)))
    ;
103 Correlation_matrix=corrcoef(P(1,:),P(2,:));
104 Correlation=Correlation_matrix(1,2);
105 end
```

]

D.3 Slip model function (q_slip.m)

```
function q=q_slip(N,L,b)

t=0.335E-9*N;
E=t/L;
b_L=b/L;


f_sher_para=8/(3*pi);

E_para=      [0.9     0.5     0.2     0.1     0.05];
f_chan_para=[0.9801 0.9053 0.8615 0.8525 f_sher_para    % b/L
   =0, no slip
             0.9052 0.8448 0.8316 0.8396 f_sher_para    % b/L
                =0.1
             0.7496 0.7696 0.8157 0.8355 f_sher_para    % b/L
                =1
             0.6804 0.7470 0.8122 0.8347 f_sher_para]; % b/L=
                inf, free slip
b_L_val=[0 0.1 1 10];

f_para=zeros(1,length(N));
for i=1:length(N)
    if E(i)<=0.05
        f_para(i)=f_sher_para;
    elseif E(i)>0.05
        f_c_p=zeros(1,4);
        f_c_p(1)=interp1(E_para,f_chan_para(1,:),E(i));
        f_c_p(2)=interp1(E_para,f_chan_para(2,:),E(i));
        f_c_p(3)=interp1(E_para,f_chan_para(3,:),E(i));
        f_c_p(4)=interp1(E_para,f_chan_para(4,:),E(i));

        f_para(i)=interp1(b_L_val,f_c_p,b_L(i));
    end
end

f_chan_perp1=[0.9597 0.7927 0.7049 0.6596 0.569
                % b/L=0, no slip
```

```
33              0.8828 0.7156 0.6284 0.5839 0.466169215373116
                   % b/L=0.1
34              0.7097 0.5416 0.4535 0.4084 0.198154317
                               % b/L=1
35              0.6263 0.4572 0.3680 0.3223 1/15];
36
37
38  b_L_val_perp=[0 0.1 1 1.2 1.4 1.6 1.8 2 2.2 2.4 2.6 2.8 3 3.2
        3.4 3.6 3.8 4 4.2 4.4 4.6 4.8 5 10];
39    % 1.2 1.4 1.6 1.8 2 2.2 2.4 2.6 2.8 3 3.2 3.4 3.6 3.8 4 4.2
          4.4 4.6 4.8 5
40  f_perp=zeros(1,length(N));
41  for i=1:length(N)
42
43  E_perp=      [0.9     0.5     0.3     0.2     0     ];
44
45  if b_L(i)>=5
46  f_chan_perp=[0.9597 0.7927 0.7049 0.6596 0.569
       % b/L=0, no slip
47              0.8828 0.7156 0.6284 0.5839 0.466169215373116
                   % b/L=0.1
48              0.7097 0.5416 0.4535 0.4084 0.198154317
                               % b/L=1
49                  0.6895     0.5212     0.4330     0.3878
                       0.1672
50      0.6742     0.5058     0.4174     0.3722     0.1436
51      0.6626     0.4941     0.4056     0.3602     0.1255
52      0.6538     0.4852     0.3965     0.3512     0.1117
53      0.6472     0.4784     0.3897     0.3443     0.1011
54      0.6421     0.4733     0.3845     0.3390     0.0930
55      0.6383     0.4694     0.3805     0.3350     0.0868
56      0.6354     0.4665     0.3775     0.3320     0.0821
57      0.6332     0.4642     0.3752     0.3297     0.0784
58      0.6315     0.4625     0.3735     0.3279     0.0757
59      0.6303     0.4613     0.3722     0.3266     0.0736
60      0.6293     0.4603     0.3712     0.3255     0.0719
61      0.6286     0.4595     0.3704     0.3248     0.0707
62      0.6280     0.4590     0.3698     0.3242     0.0697
63      0.6276     0.4585     0.3694     0.3237     0.0690
64      0.6273     0.4582     0.3691     0.3234     0.0685
```

```
    0.6270    0.4580    0.3688    0.3231    0.0680
    0.6269    0.4578    0.3686    0.3229    0.0677
    0.6267    0.4576    0.3685    0.3228    0.0675
    0.6266    0.4575    0.3684    0.3227    0.0673
              0.6263 0.4572 0.3680 0.3223 L(i)/(3*b(i))];
                % b/L=inf, free slip

elseif b_L(i)<5
f_chan_perp=[0.9597 0.7927 0.7049 0.6596 0.569
   % b/L=0, no slip
              0.8828 0.7156 0.6284 0.5839 0.466169215373116
                % b/L=0.1
              0.7097 0.5416 0.4535 0.4084 0.198154317
                           % b/L=1
                  0.6895    0.5212    0.4330    0.3878
                     0.1672
    0.6742    0.5058    0.4174    0.3722    0.1436
    0.6626    0.4941    0.4056    0.3602    0.1255
    0.6538    0.4852    0.3965    0.3512    0.1117
    0.6472    0.4784    0.3897    0.3443    0.1011
    0.6421    0.4733    0.3845    0.3390    0.0930
    0.6383    0.4694    0.3805    0.3350    0.0868
    0.6354    0.4665    0.3775    0.3320    0.0821
    0.6332    0.4642    0.3752    0.3297    0.0784
    0.6315    0.4625    0.3735    0.3279    0.0757
    0.6303    0.4613    0.3722    0.3266    0.0736
    0.6293    0.4603    0.3712    0.3255    0.0719
    0.6286    0.4595    0.3704    0.3248    0.0707
    0.6280    0.4590    0.3698    0.3242    0.0697
    0.6276    0.4585    0.3694    0.3237    0.0690
    0.6273    0.4582    0.3691    0.3234    0.0685
    0.6270    0.4580    0.3688    0.3231    0.0680
    0.6269    0.4578    0.3686    0.3229    0.0677
    0.6267    0.4576    0.3685    0.3228    0.0675
    0.6266    0.4575    0.3684    0.3227    0.0673
              0.6263 0.4572 0.3680 0.3223 1/15];
                                  % b/L=inf, free slip

end
```

```
99          f_s_p=zeros(1,24);
100     for j=1:24
101         f_s_p(1,j)=interp1(E_perp,f_chan_perp(j,:),E(i));
102     end
103
104     f_perp(i)=interp1(b_L_val_perp,f_s_p,b_L(i));
105 end
106
107
108 f_avg=3/(2/f_perp+1/f_para);
109 q=L*t*1260*9.81/(12*f_avg*0.001);
110 end
```